Severe Plastic Deformation of Copper-Titanium Alloys Using Multi Axial Cryo-Forging

Thesis

Submitted in partial fulfillment of the requirements for the degree of

DOCTOR OF PHILOSOPHY

By

Ramesh S

Under the guidance of

Dr. H. SHIVANANDA NAYAKA

Associate Professor

Department of Mechanical Engineering

National Institute of Technology Karnataka,

Surathkal, Mangalore – 575025

DECLARATION

I hereby declare that the Research Thesis entitled **"Severe Plastic Deformation of Copper-Titanium Alloys Using Multi Axial Cryo-forging"** which is being submitted to the **National Institute of Technology Karnataka, Surathkal** in partial fulfillment of the requirements for the award of the Degree of **Doctor of Philosophy** in **Mechanical Engineering** is a *bonafide report of the research work carried out by me*. The material contained in this Research Thesis has not been submitted to any other Universities or Institutes for the award of any degree.

Register Number: **165050ME16F11**

Name of the Research Scholar: **RAMESH S.**

Signature of the Research Scholar:

Department of Mechanical Engineering

Place: NITK-Surathkal

Date:

CERTIFICATE

This is to certify that the Research Thesis entitled **"Severe Plastic Deformation of Copper-Titanium Alloys Using Multi Axial Cryo-forging"** submitted by **Mr. RAMESH S. (Register Number: 165050ME16F11)** as the record of the research work carried out by him, *is accepted as the Research Thesis submission* in partial fulfillment of the requirements for the award of the Degree of **Doctor of Philosophy.**

Dr. H. SHIVANANDA NAYAKA

Associate Professor

Chairman-DRPC

Date:

ACKNOWLEDGMENTS

ABSTRACT

Severe plastic deformation (SPD) is a technique where high strains are induced into the material to produce fine-grained structural materials, thereby improving the wear resistance and corrosion resistance. There is an increase in scientific and industrial interest in the development of bulk ultra-fine-grained (UFG) alloys, intended for structural applications. UFG materials offer vastly improved mechanical and physical properties. They also exhibits superplastic properties at elevated temperatures. SPD is done using Equal Channel Angular Pressing (ECAP), High-Pressure Torsion (HPT), Repetitive Corrugation and Straightening (RCS), Accumulative Roll Bonding (ARB) and Multi Axial Forging (MAF). In MAF, materials are forged repeatedly in a closed die along three orthogonal directions, sequentially. It allows processing of relatively ductile material, because it can be performed at cryogenic temperature.

Literature review shows that by using MAF technique, grain refinement phenomena can be observed in some ferrous and non-ferrous metals. MAF is one of the simple and most effective methods of SPD to improve material properties. MAF is a process in which the workpiece is subjected to shear deformation and thus, severe plastic strain is induced into the material without any change in the cross-sectional dimension of the sample. Microstructure has major effect on mechanical properties. MAF process leads to ultrafine-grained microstructure in the material which may show superplastic deformation at low temperature and high strain rate. In FCC structured metals, grain refinement also leads to textural changes i.e. high strengthening at cryogenic condition deformation. Copper-Titanium (Cu-Ti) alloy is the nontoxic substitute for Cu-Be and it showed good mechanical and electrical properties and can be used for the production of high strength spring, corrosion-resistant elements, and electrical connections like contact, relay, gears and electrical wires.

Hence, in the present study, three alloys of Cu-Ti, namely, Cu-1.5%Ti, Cu-3%Ti and Cu-4.5%Ti, have been processed by MAF. Microstructural evolution in different MAF cycles is studied and it is correlated to the mechanical properties observed. As UFG materials have much higher hardness, they are expected to have higher wear resistance. MAF processed material exhibits higher wear and corrosion resistance, than the as-received material. Hence MAF processed samples find wider engineering applications.

Literature review consists of features of various SPD Techniques, advantages, and limitations. MAF process, parameters which influence MAF process, advantages and applications of MAF processed Cu-Ti alloys are discussed in details. Works of different researchers on MAF processed Copper alloys, with respect to, mechanical properties, wear and corrosion behavior are reported. Motivation from literature survey and objectives of the present work are highlighted.

Details of the experimentation performed, right from the process adopted for the development of the UFG Cu-Ti to their characterization, are given in chapter three. Microstructural analyses were performed using optical microscopy (OM), scanning electron microscopy (SEM), transmission electron microscopy (TEM) and electron backscatter diffraction (EBSD). Tensile tests were performed on both as-received and MAF processed samples. Dry sliding wear testing was performed using Pin on disc testing machine for both unprocessed and MAF processed samples. For the study of corrosion behavior, electrochemical polarization studies were performed and tofel extrapolation technique was used to obtain the corrosion rates.

Chapter 4, Chapter 5 and Chapter 6, explain the results and discussion of various experiments carried out on three alloys Cu-1.5%Ti, Cu-3%Ti and Cu-4.5%Ti Microstructural characterization by OM, SEM, TEM, EBSD and XRD analysis has been discussed. Mechanical properties which includes hardness, tensile followed by fractography has been analyzed. Wear test with different loading conditions and sliding distances has been explained. Corrosion studies by electrochemical measurements test method has been highlighted.

Key words: *Multi axial cryo-forging, Cu-Ti Alloys, Grain Refinement, Microstructure, Mechanical Properties, Fractography, Wear, Corrosion, X-ray Diffraction, Energy dispersive X-ray spectrometer*

TABLE OF CONTENTS

LIST OF TABLES

LIST OF FIGURES

xvii

xviii

NOMENCLATURE

ARB : Accumulative Roll Bonding

ASTM : American Society for Testing and Materials

BCC : Body Center Cubic

CCDF : Cyclic Closed-Die Forging

CEC : Cyclic Extrusion Compression

CGP : Constrained Groove Pressing

COF : Coefficient of Friction

DFT : Density Functional Theory

DRX : Dynamic Recrystallization

EBSD : Electron Back-Scatter Diffraction

ECAP : Equal Channel Angular Pressing

EDS : Energy Dispersive X-ray Spectroscopy

EIS : Electrochemical Impedance Spectroscopy

ES : Extrusion Shear

FCC : Face Centred Cubic

FE-SEM : Field Emission Scanning Electron Microscope

HAGB : High Angle Grain Boundaries

HCP : Hexagonal Closed Pack

HDS : Hot Die Steel

HPT : High Pressure Torsion

HPTE : High Pressure Torsion Extrusion

IPF : Inverse Pole Figure

LAGB : Low Angle Grain Boundaries

LN_2 : Liquid Nitrogen

MAF : Multi Axial Forging

OM : Optical Microscopy

OIM : Orientation Imaging Microscopy

RCS : Repetitive Corrugation and Straightening

SAED   : Selected Area Electron Diffraction

SCE   : Saturated Calomel Electrode

SEM   : Scanning Electron Microscopy

SPD   : Severe Plastic Deformation

TEM   : Transmission Electron Microscopy

UFG   : Ultrafine grain

UTM   : Universal Testing Machine

UTS   : Ultimate Tensile Strength

XRD   : X-ray Diffraction

YS   : Yield Strength

SYMBOLS

Φ	:Die channel angle
Ψ	:Outer arc of curvature
ε_N	:Equivalent strain
σ	:Yield stress
σ_O	:Friction stress
k	:Locking parameter
d	:Grain size
Ø	:Diameter
HV	:Vickers microhardness
ρ	:Metal density
ΔW	:Weight loss rate
V_H	:Hydrogen evolution rate
P_H	:Corrosion rate
E_{corr}	:Corrosion potential
I_{corr}	:Corrosion current density
β_a	:Anodic constant
β_c	:Cathodic constant

CHAPTER 1

1. INTRODUCTION

Grain size of material plays a very significant role in determining the mechanical and physical properties of materials. Interest has been directed towards the development of new techniques to produce ultrafine grained materials. Ultrafine grains (UFG) can be accomplished either by bottom-up approach or top-down approach. In bottom-up approach, individual atoms or molecules are consolidated into bulk materials, like in inert gas consolidation, electrodeposition, hot isostatic pressing, whereas, in top down approach, solid materials usually having coarse grain structure, are refined to UFG materials.

Top-down approach can be accomplished by conventional processing and severe plastic deformation. Conventional processes like cold rolling and drawing result in grain refinement. However, structures formed usually have low angle grain boundaries. Severe plastic deformation results in high degree of grain refinement along with the accumulation of high plastic strains which leads to the formulation of high angle grain boundaries.

Strength of metals and alloys are increased by reducing the grain size, as per Hall-Petch Equation (Hall, 1951, Petch, 1953, Dieter, 1998). Development of bulk and UFG materials for structural applications has led to an increases in scientific and industrial interest. This increases an interest to develop ultrafine grains for structural applications in industries (Valiev et al. 1991, 1994, 2006). Grain refinement is one of the methods to improve strength and other mechanical properties. Ultrafine grained metals and alloys shows excellent mechanical properties such as high strength, fracture toughness, wear resistance, superplasticity and corrosion resistance (Bhowmik et al. 2009). There are various methods of producing UFG materials. Among them, the most important technique is the severe plastic deformation (SPD) technique.

Severe plastic deformation (SPD) is the method to produce ultrafine grains, where high strain is imposed on the sample at lower, as well as, at higher temperature conditions, without any change in cross sectional area of the samples.

UFG materials, in spite of having high strength, have poor ductility at room temperature (Dieter, 1998). Fine grains cause less accumulation of dislocations near grain boundaries and causes low strain hardening and subsequently, results in poor ductility (Jia et al. 2001, Joshi et al 2016). Materials, with low stacking fault energy, tend to generate mechanical twins during deformation, which can improve ductility without much loss in strength (Zhu et al. 2004). Ultrafine grains have been effectively developed by various severe plastic deformation (SPD) techniques, such as Accumulative Roll-Bonding (ARB) (Anne et al. 2017), Multi-Axial Forging (MAF) (Chen et al. 2012, Rao et al.2014, Gupta et al. 2016), High-Pressure Torsion (HPT) (Harito et al. 2005, Ivanisenko et al. 2016) Repetitive Corrugation and Straightening (RCS) (Huange et al. 2004, Sunil et al. 2015) Equal Channel Angular Pressing (ECAP) (Gopi et al. 2016, Gopi et al. 2017) Constrained Groove Pressing (CGP) (Shin et al. 2002, Yadav et al. 2016) machining (Swaminathan et al. 2007, Yadav et al. 2018) and cryo-rolling (Subramanya et al.2008) Among these SPD techniques, MAF is considered a simple process, where the material is forged sequentially in three orthogonal directions. Thus, even after several cycles of forging, original shape of the material remains unaltered. Also, microstructures generated are homogeneous and isotropic in terms of mechanical properties which are generally not found in most of the other SPD processes. Compared to cold/hot deformation, MAF, at cryogenic temperature (-196 ºC), can produce a more refined microstructure, as recovery and recrystallization are completely suppressed at cryogenic temperature. This results in high dislocation densities and other defects, especially in materials having low stacking fault energy (Rao et al. 2016). Cold MAF is a unique process in which, forging is done at low temperatures (both at room and cryogenic temperatures), whereas, there is a change in strain path after each forging pass and it is characterized by higher deformation rates, in order to produce bulk samples.

Copper and its alloys are extensively used in automobile, constructional and electrical components. Among copper alloys, Cu–Be alloys show premier mechanical properties, high corrosion resistance, good thermal and electrical conductivity along with non-sparking behavior and good formability during cold and hot working. Due to these properties, Cu-Be alloys are used in explosion activities in mines and engine

chambers, where sparking may prove hazardous (Nagarjuna et al.1997,1999, Sembhoshi et al. 2013) However, Cu-Be alloys are relatively costly. Also, Be compounds are toxic and so, there are health risks when exposed to atmosphere during material processing, such as melting, cutting, welding, casting, grinding and hot deformation operation (Nagarjuna 1994). Due to their toxic characteristics, there has been a complete ban on use of Be compounds for many years in European Union countries (Szkliniarz et al. 2014). This led to an extensive research to develop low cost and non-toxic Cu alloys.
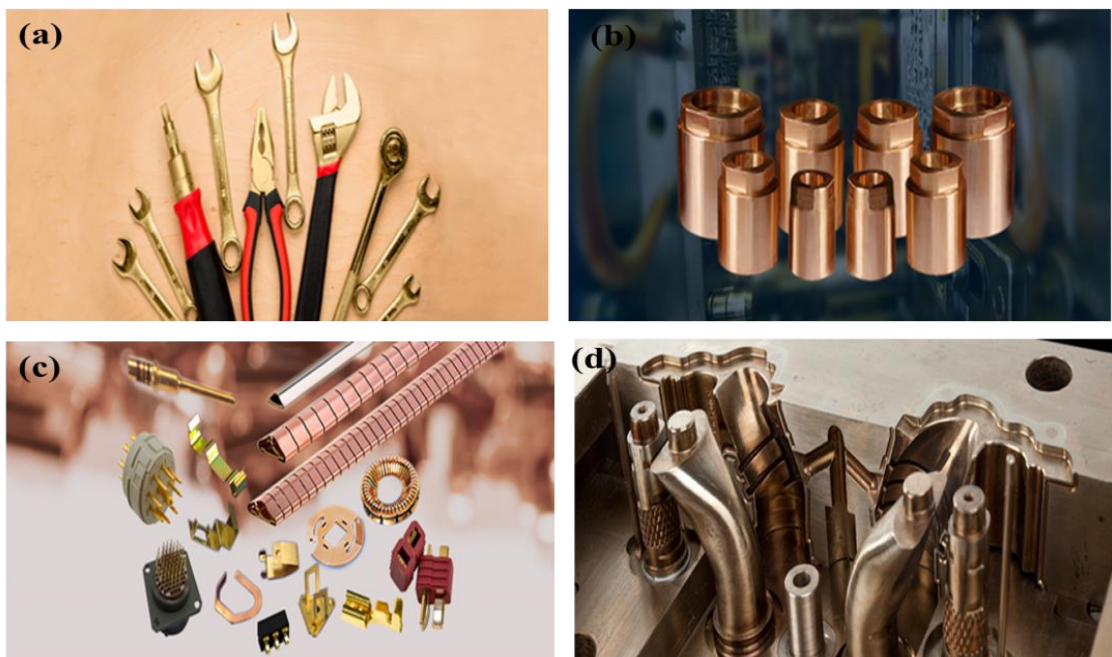
Figure 1.1 Applications of Cu-Ti alloys (a) Non-Sparking Tools (b) Engine valve Seats (c) Electrical Applications (d) MIG Welding Contact Tips

Cu-Ti alloys are the non-toxic substitutes for Cu-Be and show good mechanical and electrical properties. Hence, they can be applied for production of high strength springs, gears, electrical wires, as well as, in elements resistant to corrosion and abrasion in electrical connections like contact and relay (Nagarjuna et al. 1997) Owing to these properties, Cu-Ti alloys are used for improvement in quality of silicon solar cells, (Deghan et al. 2007) heat transfer applications (Nagarjuna et al. 2004) electronic devices, such as relay controls and connectors (Semboshi et al. 2014) and biomedical applications (Kikuchi et al. 2003). Some of the major applications of Cu-Ti alloys are shown in Figure 1.1 Nagarjuna et al. (1995) investigated the deformation characteristics

of solution treated Cu-Ti alloys and found that true stress increases with increase in Ti content (Zhao et al. 2006) Grain boundary strengthening and solid solution treatment contribute to increase in flow stress and modulations. Precipitation promotes further increase of strength and deformation, mainly, due to twinning mechanism. Huan WEI et al. (2018) investigated corrosion behavior of Cu−Ti alloys in 3.5% NaCl solution with addition of different percentages of Ti content and showed that, by increasing Ti content, corrosion resistance decreases.

Present work aims to provide the systematic study in the relation between processing and structure-properties, which will facilitate the migration of knowledge from the basic principles to the development of copper alloy with superior properties.

Content of the thesis

This thesis contains Eight chapters and are outlined as follows;

Chapter 1, represents the introduction of severe plastic deformation process, grain refinement, and Multi axial forging process. Various features related to copper and its alloys, selection of Cu-Ti alloy, its application, and drawback of Cu-Be alloy are discussed.

Chapter 2, presents the literature of the present study. This chapter discussed about, different SPD process and factors affecting the MAF process. Characteristics of Cu alloy, mechanical properties, wear and Corrosion properties discussed. Based the literature review, selection of objectives for present research is highlighted.

Chapter 3, explains the step-by-step experimental procedure and materials used for the MAF process. Detail description of equipments used in the present work and sample preparation methods are also explained.

Chapters 4, 5 and 6 discuss the results obtained during processing of Cu-1.5%Ti, Cu-3%Ti and Cu-4.5%Ti alloys respectively, by multi axial forging process at cryogenic temperature. XRD was conducted to identify the different phases in the samples deformed and undeformed conditions. Microstructural characterization was carried out using Optical microscope (OM), Scanning electron microscopy SEM, Transmission electron miscroscopy (TEM) and electron backscattered diffraction (EBSD) for grin structure and grain boundary misorientation angles. Mechanical testing like, tensile, hardness, wear analysis and corrosion studies were done for as-received and MAF processed samples of all three copper alloys.

Chapter 7, discuss the effect of variation of Titanium content on all properties estimated.

Chapter 8, Explains conclusions and scope for future work.

CHAPTER 2

2. LITERATURE SURVEY

Literature review gives brief discussion on Multi axial forging (MAF) technique, which is used for obtaining Ultrafine grained structural materials and also introduction to Copper and Copper alloys. MAF technique is discussed considering the available literature and the motivation for the present work, followed by objectives of the present work. It also includes the literature of the SPD processed materials with respect to microstructure, mechanical, wear and corrosion properties. SPD produces fine crystalline structures in different bulk materials. Strains are induced to attain grain refinement in the material. Microstructural changes caused by SPD, increase the material properties like hardness and strength, but reduce ductility. Coarse-grains are converted to ultra-fine grain by imposing high strain on the material to induce dislocations and are re-assembled to form a group of grain boundaries. Few conventional metal-working processes like rolling and extrusion are restricted to produce fine grained structures due to following reasons. Firstly, limitation of imposing strains into the material, because this process causes reduction in the cross-sectional area of the specimen. Secondly, the imposed strains are not sufficient to produce UFG materials due to low workability at lower temperature (Valiev et al. 2000).

Copper and copper alloys are extensively used in automobile, construction and electrical components. Among copper alloys, Cu–Be alloys show premier mechanical properties, high corrosion resistance, good thermal and electrical conductivity, along with non-sparking behavior and good formability, during cold and hot metal-working processes (Lee et al. 2019). Due to these properties, Cu-Be alloys are used in explosion activities in mines and engine chambers, where sparking may prove hazardous (Nagarjuna et al. 1997, 1999; Semboshi et al. 2013; Szkliniarz et al. 2014). However, Cu-Be alloys are relatively expensive. Also, Beryllium compounds are toxic and so, there are health risks when exposed to atmosphere during various processing, such as melting, cutting, welding, casting, grinding and hot deformation operations (Nagarjuna et al. 1994). Due to their toxic characteristics, there has been a complete ban on use of Be compounds for many years in European Union countries (Szkliniarz et al. 2014).

This led to extensive research to develop low cost and non-toxic Cu alloys (Nagarjuna, 2004; Semboshi et al. 2014).

Copper-Titanium (Cu-Ti) alloy is the nontoxic substitute for Cu-Be and it showed good mechanical properties, superior corrosion resistance, better electrical properties and antiseptic properties (Nagarjuna et al. 1997,1999). Further, Cu-Ti alloys can be used for production of high strength springs, corrosion resistant elements, and electrical connections like contact, relay, gears and electrical wires (Lee et al. 2019; Semboshi et al. 2014). Cu-Ti alloys are also used to improve quality of silicon solar cells (Dehghan et al. 2007) heat transfer applications (Nagarjuna et al. 2004), electronic devices, such as relay controls and connectors (Semboshi et al. 2014) and biomedical applications (Kikuchi et al. 2003). It is known that ultrafine-grained or nanostructured materials have high mechanical strength, however, poor ductility at room temperature (Dieter,1998). Fine grains cause less accumulation of dislocations near the grain boundaries and causes low strain hardening and subsequently, poor ductility (Jia et al. 2001; Zhu et al.2004). Materials with low stacking fault energy tend to generate mechanical twins during deformation which can improve ductility without much loss in strength (Zhao et al. 2006). Ultrafine grains have been effectively development by various severe plastic deformation (SPD) techniques such as accumulative roll-bonding (ARB) (Anne et al. 2017), multi-axial forging (MAF) (Chen et al. 2012, Rao et al. 2014, Akbaripanah et al. 2017, Xia et al. 2015), high-pressure torsion (HPT) (Harita et al. 2005, Ivanisenko et al. 2016, Zhilyaew et al. 2001, 2008), repetitive corrugation and straightening (RCS) (Huang et al. 2004, Sunil, 2015), equal channel angular pressing (ECAP) (Raab et al. 2004, Stolyarov et al. (2001), Zhu et al. 2000, Gopi et al. 2016), constrained groove pressing (CGP) (Shin et al. 2002, Yadav et al. 2016), machining (Swaminathan et al. 2007, Yadav et al. 2018) and cryo-rolling (Sarma et al. 2008, Among these SPD techniques, there have been several studies relating to the evolution of microstructure and mechanical properties of materials, processed by MAF at room temperature. Huang et al. (2001), observed improvement in yield strength (YS) and ductility of Cu-6% Al alloy processed by MAF at room temperature, through enhancement in strain hardening rate. Padap et al (2009), witnessed the enhancement in mechanical properties due to reduction in grain size from 30 to 0.5 μm by MAF

process, in hot conditions, for low carbon steels. Chen et al (2016), used MAF for processing AZ61 magnesium alloy at different temperatures and was able to reduce grain size to 8 μm from 131 μm. Gupta et al (2016), processed high lead bronze tin (Cu-17% Sn-4.5% Pb-6% Zn) through MAF and reported that the increase in deformation strain (during 1, 2, and 3 cycles) steadily improved homogeneity in terms of various microstructural parameters, such as grain size, twin spacing, twin lamellae thickness and dislocation density. Rao et al (2014), processed Al6061 alloy through MAF, at cryogenic temperature to obtain ultrafine grain structure and consequently, improved the mechanical properties.

Dasharath et al (2016) investigated the tensile behavior of Cu-9.6% Zn alloy at cryogenic temperature at $\varepsilon = 3$, 5.4, and 7.2. YS and % elongation were estimated as 680 MPa and 7%, respectively. It was observed that dimple size and shear fracture angle decreased during fractured surface analysis. Ultrafine grained structure was developed with a high dislocation density, because of low stacking fault energy (Gupta et al. 2016; Ning et al. 2012; Kumar et al. 2019). MAF is simple repeated compression process with sample being rotated at 90° during each pass, and large plastic strains being imposed on the sample. Magnesium alloy Mg-Al-Zn was processed at room temperature using MAF at $\varepsilon = 2$ by Miura et al.2007. After 20 MAF passes, strength increased to 525 MPa. Joshi et al. (2016), processed Al-2014 alloy by MAF at cryogenic condition for 4 cycles with $\varepsilon = 2.4$. It was found that the ultrafine grains were formed with grain size in the range of 100-450 nm and hardness, being increased from 103 HV to 171 HV and fracture toughness increased to 37.7 MPa-m$^{0.5}$ from 23.93 MPa m$^{0.5}$. Yang et al. (2013) processed AZ31 magnesium alloy by MAF under decreasing temperature conditions for every pass. Low temperature MAF was found to accelerate the formation of fine grain structure and plastic workability. Padap et al (2009) processed plane low carbon steel at 500° C using MAF. After 9 passes of MAF, strength and hardness increased from 357 MPa to 791 MPa and from 120 HV to 252 HV, respectively. As MAF passes increased, LAGBs were converted to HAGBs and grain size reduced to 0.5 μm.

2.1 Severe plastic deformation

Automobile and aerospace industries use materials of ultrafine grained structures, processed by severe plastic deformation (SPD) (Valiev et al. 1993, 2000, 2004, 2006) techniques, as they possess superior mechanical properties like high strength, fatigue, ductility, and fracture resistance. Some of the SPD techniques developed in past few decades are given below.

- ECAP (Equal channel angular pressing)
- ARB (Accumulative roll bonding)
- MAF (Multi-axial forging)
- RCS (Repetitive corrugation and straightening)
- HPT (High-pressure torsion)

(i) Equal Channel angular pressing (ECAP)
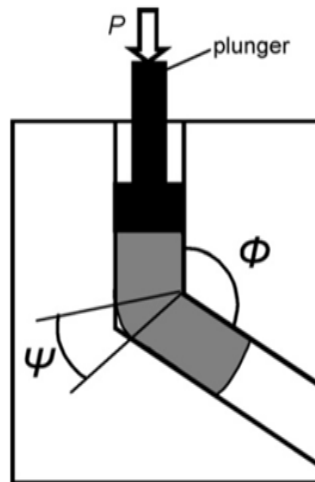
Figure 2.1 Schematic of ECAP setup (Azushima et al. 2008)

ECAP process was first introduced by Segal and Co-Workers in 1980s. This is one of the most investigated techniques in the 90's (Valiev et al.2000). In ECAP process, the billet is passes through a special die, in which the angle of intersection of two channels is in between 90° to 130°. After each pass, sample was rotated in longitudinal axis at 90° (Route B) and 180° (Route C). Plastic shear deformation was occurring without changing the cross-sectional dimension. Schematic diagram of ECAP setup as shown in Figure 2.1.

(ii) Accumulative Roll Bonding (ARB)

Another SPD process suitable to produce ultrafine grain structure in sheet metals is the ARB. ARB process involves sample preparation, surface treatment, stacking, heating and rolling. Each rolling pass was maintained with a constant strain. There are two possibilities in ARB. They are (i) severe stress is introduced between rollers and work piece, under dry condition, shear deformation increases the equivalent strain, which promotes the grain refinement (Li et al. 2006) and (ii) formation of new intermetallic elements. After number of ARB passes, number of layers are formed in sample, with some secondary phases formed, contributes to strengthening (Lee et al. 2002). Schematic diagram of ARB process as shown in Figure 2.2.
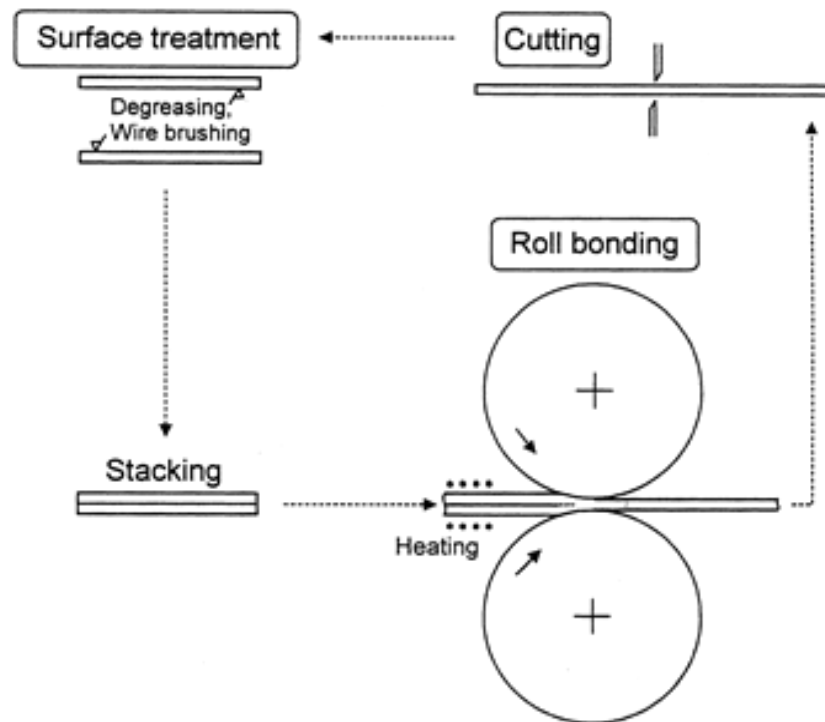
Figure 2.2 Accumulative roll bonding process (Tsuji et al. 1999)

For each pass, initial thickness per layer of the strip is $t_n = t_i/2^n$, where t_i is the initial thickness, n is the number of cycles. After n cycles, total reduction is $r_t = 1 - 1/2^n$. Equivalent plastic strain is $\varepsilon_T = 0.8n$.

(iii) High Pressure Torsion (HPT)
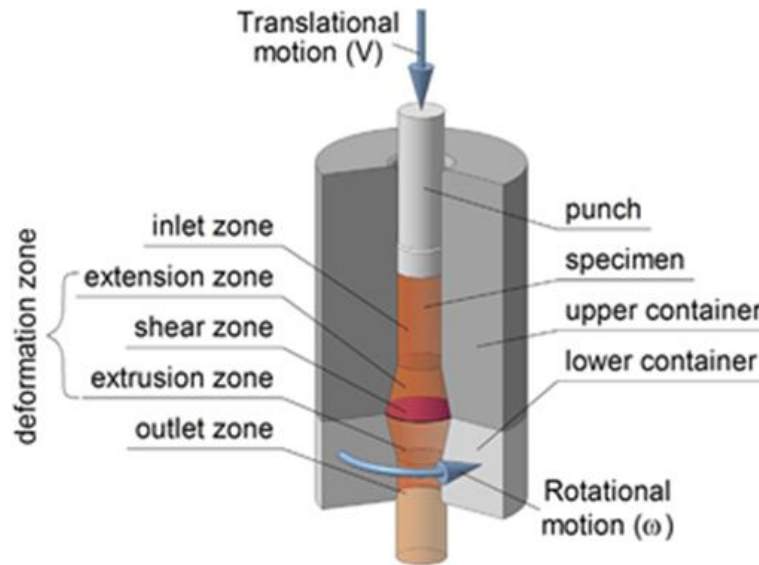
Figure 2.3 Schematic diagram of high-pressure torsion (Ivanisenko et al. 2016).

In HPT, material is deformed through two containers where one is stationary and the other rotates. Sample is placed inside the channel and the outlets are locked. High pressure is applied on stationary container and torsional motion is given by lower container. Deformation occurs by shear, which is attributed to friction forces of the surfaces and the rotation of the lower container. Section view of high-pressure torsion as shown in Figure 2.3.

(iv) Repetitive Corrugation and Straightening (RCS)

Figure 2.4 shows the schematic diagram of repetitive corrugation and straightening. In this process, sheet sample was continuously passed between different set of rolls. Because of this continuous bending and straightening, high strain is induced in the sample, resulting in sample of high density of dislocations and grain refinement. During first pass, samples pass between corrugated roll, then passed through flat rolls without any change in sample dimension.
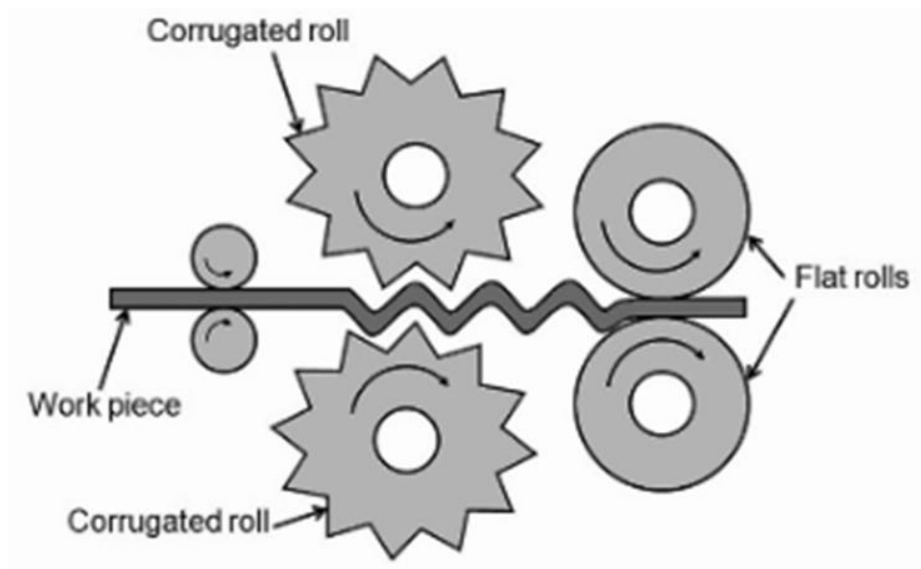
Figure 2.4 Repetitive corrugation and straightening (Sunil et al. 2015)

(v) Constrained Groove Pressing (CGP)
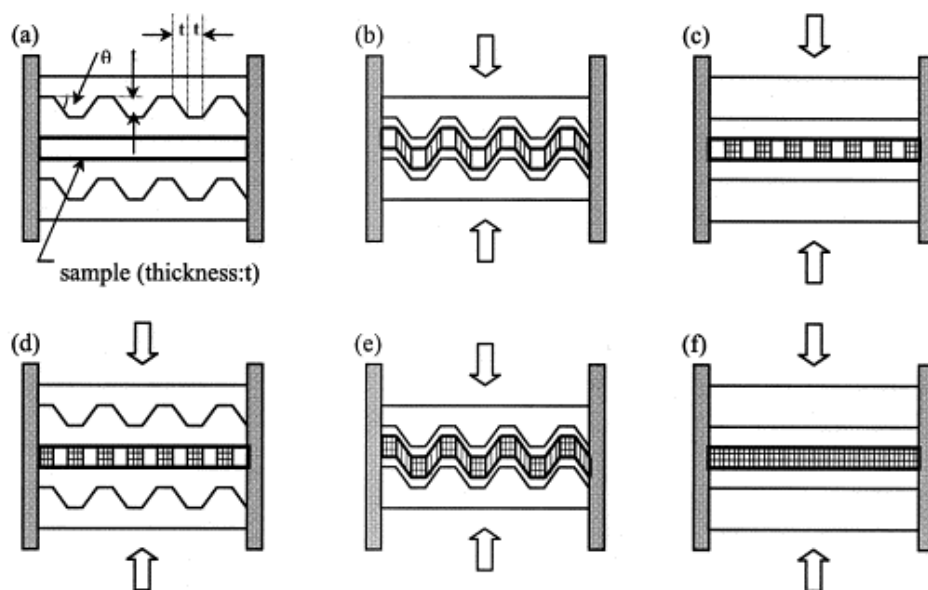
Figure 2.5 Constrained groove pressing die set up

CGP die consists of two asymmetrically grooved plates as shown in Figure 2.5. Flat sample is placed between grooved plates which are constrained by cylinder wall. After pressing, only inclined portion of the sample undergoes shear deformation with plane strain conditions, without any deformation in flat region. In second press, flat face of the die is used for pressing and make the sample flat. Here, the sample was rotated

by 180° and the above-mentioned procedure was followed. This will achieve the homogeneous strain and produce high plastic strain without any change in sample dimension.

2.2 Strengthening Mechanism

Various strengthening mechanisms like strain hardening, grain boundary strengthening, precipitation hardening and solid solution strengthening are used to produce the material with desirable properties. During SPD process, precipitate hardening, dislocation density and grain refinement are responsible for strengthening.

(i) Strain hardening

Strain hardening plays a major role to strengthen the materials during metal forming. When plastic deformation occurs, dislocation (Lavrentev, 1980) is the main reason for strain hardening. Because, dislocations interact with each another to generate stress inside the material. When two dislocations are crossing each other, it forms dislocation tangles and cause jog formation. This jog restricts the movement of dislocation and with increase in dislocation density, yield strength increases. Increase in plastic strain, directly depends on the amount of dislocation density inside the sample. But major disadvantage is the reduction of ductility during strain hardening.

(ii) Grain boundary strengthening

It is a method of strengthening the material by decreasing the grain size. Changes in grain size influence the dislocation movement and yield strength. Strength increases with decrease in grain size, according to the Hall-Petch relationship (Hall, 1951; Petch, 1953). During change in grain size structure, more energy is required for dislocation to move to adjacent grain. In this mechanism, grain boundaries are more disordered than the interior of grain. This movement of dislocations will hinder the plasticity and hence increase the strength of the sample.

Hall-Petch equation is given by

$$\sigma = \sigma_o + \frac{k}{\sqrt{d}}$$ …………………………… (2.1)

Where,

σ = Yield stress (MPa).

σ_o = "Friction stress" representing the overall resistance of the crystal lattice to dislocation movement (MPa).

k = "Locking parameter", which measures the relative hardening contribution of the grain boundaries.

d = Grain size (μm).

(iii) Dynamic recovery

It is the basic mechanism that leads to the annihilation of pairs of dislocations during straining. Low dislocation densities associated with deformation are because of the ease of slip crossing, climbing and dislocation unpinning at nodes at particular temperature regions, during hot working. This deformation mechanism results in microstructure, consisting of elongated grains. Inside these elongated grains, are well developed fine subgrain structure, typically of the order of 1-10 μm. The grains are broken up and reform during the deformation, thus they maintain their equiaxed shape. Dynamic recovery occurs in metals of high stacking fault energy, such as, aluminium, alpha iron and BCC metals (Dieter, 1988). In the study involving warm MAF of austenitic stainless steel, it was suggested that, the evolution of new fine grains could be assisted by dynamic recovery, which promotes dislocation rearrangement at their boundaries (Belyakov et al.2000).

(iv) Precipitation hardening

Precipitates are small, uniformly dispersed secondary phases in the original phase matrix. These secondary phases are dissolved after aging the sample and quenching in solution. Precipitation hardening can be achieved by two steps of heat treatment. First step is solution treatment by quenching process, where all solute atoms are dissolved and form a single phase solution. In second step, samples are aged at lower temperature for a specified time and forms fine dispersed precipitates and acts as barrier to the movement of dislocations. Different stages of hardening are shown in Figure 2.6. This restriction in movement of dislocation increases the strength. There are three types of precipitate hardening: dispersion hardening, internal strain hardening and chemical hardening.
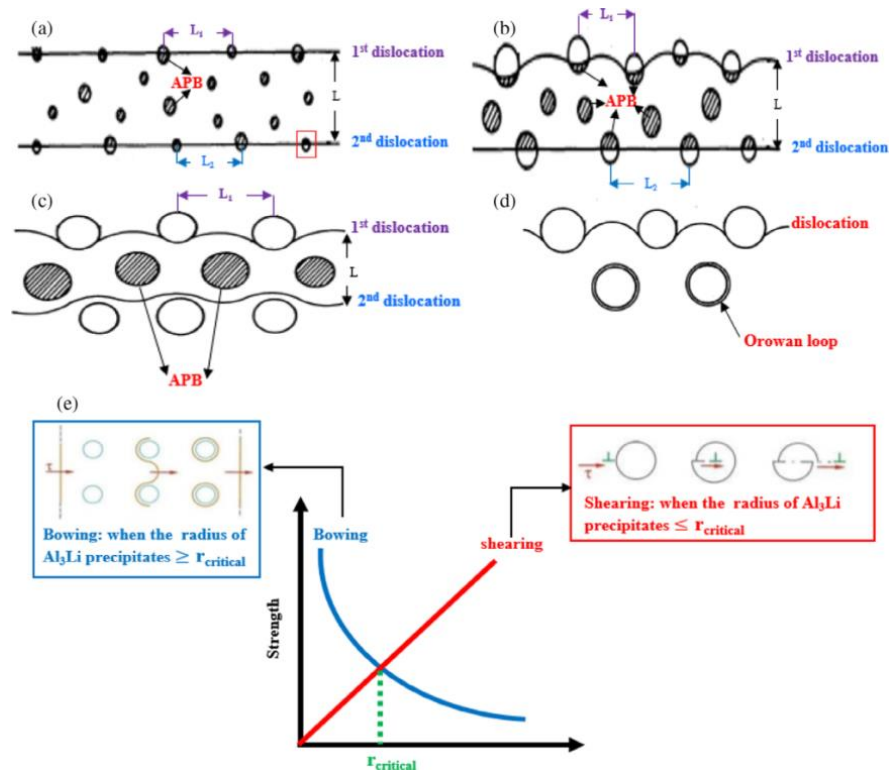
Figure 2.6 Mode of interaction between precipitates and dislocation (a) quenched condition (b) Under-aged (c) peak-aged condition (d) over-aged condition (Ali et al. 2018)

2.3 Mechanism of Grain Refinement

Grain refinement mechanism depends on processing material and processing temperature. Some of the grain refinement mechanisms are discussed below.

(i) Dynamic recrystallization

In dynamic recrystallization, dislocation annihilation occurs when dislocation densities reach to very high levels during deformation (Dieter, 1988). Formation of sub microcrystalline structure in a titanium alloy, was ascribed to dynamic recrystallization and spherodization process (Haung et al. 2006). In warm MAF of austenitic Fe-32 Ni alloy, at 550 °C, continuous dynamic recrystallization was responsible for the evolution of UFG microstructure, as studied by Huang et al. (2006). Continuous dynamic recrystallization can occur under large strain deformation, producing remarkably refined austenite structure. During each deformation step, deformation bands were produced in deformed grains, attributing to slip shear. These deformation bands cross

with other deformation bands, formed in other directions while changing the strain path during successive strain steps. Thus, grains are subdivided into several subgrains. These subgrains get converted into independent grains with a HAGB in subsequent strain steps.

(ii) Slip and twinning

In warm MAF of α-Ti, new grains are formed by the mechanism of slip and twinning. Deformed boundaries in Ti are categorized in two different ways, based on their initiation, viz slip and twinning. Slip causes gradual increase in misorientation angle, whereas twinning immediately gives rise to HAGBS. So, it was concluded that twinning is the deformation mechanism which is dominant in early stages of deformation, while, prismatic slip is the dominant deformation mechanism during the later stages of plastic flow.

(iii) Intersection of micro shear bands

In multi axial compression studies on α-Fe-C at room temperature, grain refinement was explained. But, microbands intersect to form subgrains, because of strain localization. These subgrains subsequently rotate to form ultra-fine crystallites. Grain refinement in hot MAF (490°C) of 7475 Al alloy occurred, via, intersection of micro shear bands, followed by grain boundary sliding, that increased the micro orientation between the subgrains formed. Figure 2.7 shows various stages in grain refinement during the MAF process.

(a) During the first pass of MAF, grains are elongated due to the formation of the deformation band with high dislocation densities.

(b) In second pass, when the loading direction changes, Intersection of deformation bands occurs with those generated during a previous forging pass.

(c) When it changes to third direction, crossing of microshear bands increased and ultrafine grains form at the intersection of deformation bands.

(d) With the repetition of passes, homogeneous ultrafine-equiaxed grains are formed.
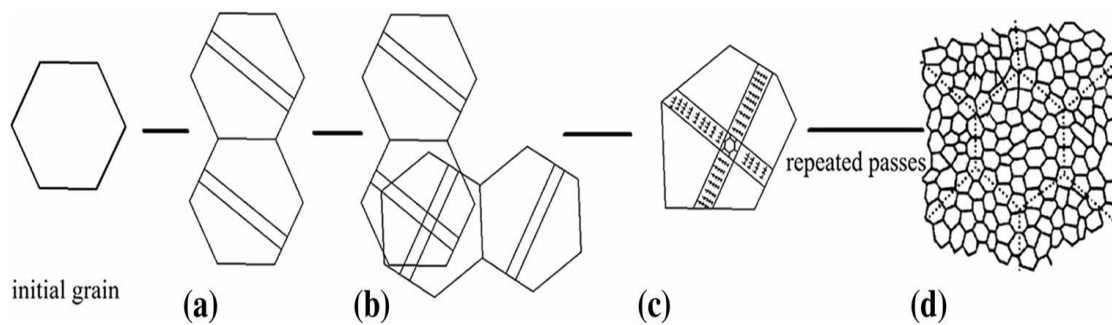
Figure 2.7 Schematic representation of stages in grain refinement during MAF (Wang et al. 2016).

2.4 Brief History of MAF

In 1982, multi axial forging was carried out on 1100 aluminum cubes for the first time by Armstrong et al. (1982) and microstructural features were discussed. Saturated flow stresses were developed in three orthogonal directions, because of high accumulated strain. Saturated flow stress is a function of strain increment and followed by Power Law. Armstrong et al. (1982) discussed and compared the studies on copper and alpha iron by other authors. Copper showed similar, but more pronounced, behavior. Deformed structures by MAF processed Al consist of cells, subgrains and tangles change in microstructure is very systemic in nature with strain accumulation. Variation in size and concentration of cells and subgrains was noticed during unidirectional and multi directional forging. These variations are correlated with sub structured grain formed. These features have correlated the relationship between sub-structural grain. Pure titanium was subjected to multiaxial forging at 773 K. Grain size changed from coarse to ultrafine grains were observed after 6 passes of MAF. Because of continuous dynamic recrystallization induced by deformation bands and subdivisions of grains by mechanical twinning (Bing Feng et al. 2016).

(i) Principle of multi axial forging

MAF is considered as a simple process, where the material is forged sequentially in three orthogonal directions. Thus, even after several cycles of forging, original shape of the material remains unaltered. Microstructures generated are homogeneous and isotropic in terms of mechanical properties, which are generally not found in most of the other SPD processes. Compared to cold/hot deformation, MAF at

cryogenic temperature can produce more refined microstructure, as recovery and recrystallization are completely suppressed at cryogenic temperature, resulting in high dislocation densities and other defects, especially in materials having low stacking fault energy.

(ii) Process parameters of MAF process

a) **Pressing Speed (Strain rate):** In SPD process, strain rate increases grain refinement and mechanical properties. Although, it is known that grain refinement is because of dynamic recrystallization, employment of higher strain rates can have additional effects due to the suppression of recovery.

b) **Pressing Temperature:** In SPD process, temperature plays a major role for obtaining grain refinement and mechanical properties (Sakai et al. 2014). At lower temperature, grain refinement is predominant. But, as temperature increases, load carrying capacity of the sample decreases and grain refinement is less. Figure 2.8 shows the variation of flow stress with cumulative strain for different processing temperatures during processing of Copper.

c) **Lubrication**: Friction is developed between the mating parts in the die. Using proper lubricant (molybdenum di sulphite), friction can be reduced. Otherwise barreling effect is more on the surface of the sample
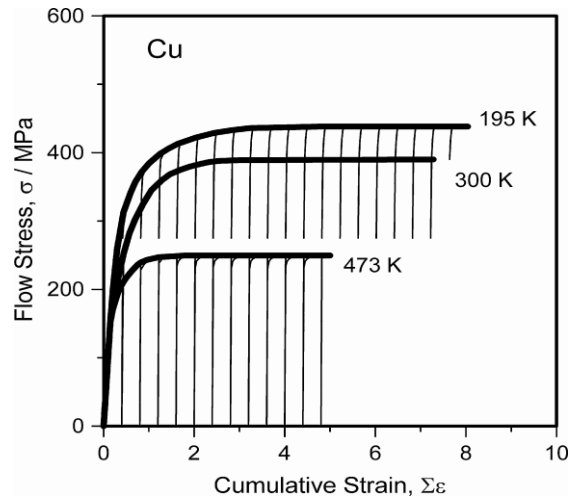
Figure 2.8 Stress-Strain diagram of Cu with strain rate of $3 \times 10^{-3} s^{-1}$ at temperatures of 195K, 300K and 473K (Sakai et al. 2014).

(iii) Advantages of Multi-axial Forging over other SPD process

1. MAF can be carried out using conventional pressing machine without any special machine attachment and can be used in mass production.
2. MAF is a simple repeated pressing process which has the option of changing the loading direction and experiment can be done in both conditions.
3. Shape of the original sample doesn't change after successive MAF passes and analytically studied the microstructure and stress v/s strain relation

2.5 Non-Ferrous Metals and Alloys

(a) Aluminum and copper alloys

Effect of Multiaxial cryoforging on mechanical properties and fracture toughness of Cu-9.6%Zn was investigated by Dasharath et al (2017). Sample was forged to 5, 9 and 11 cycles with a maximum cumulative strain of 6.6. Samples cryo forged upto 11-cycles showed improvement in yield strength (YS) by more than 10 times (818 MPa), as compared to that of the homogenized sample (76 MPa). Ductility of the material decreased by 10%, due to recrystallization and suppression of dynamic recovery during multi axial cryoforging. TEM micrographs and SAED patterns showed the formation of shear bands and deformation twins, at higher passes of MAF at cryogenic temperature.

Dasharath et al. (2017) investigated high cycle fatigue behavior of ultrafine grained Cu-4.5% Al processed by cryo rolling. Cu-4.5% Al was subjected to cryoforging & subsequent short-annealing at 225 °C. Samples showed superior fatigue strength along with best combination of YS, ductility and fracture toughness. High density twin bundles (twin-twin intersections) with 20–50 nm twins spacing are highly susceptible to the contribution of increased fatigue life, hindering the crack propagation. Deformation mechanisms were controlled by the low stacking fault energy of the material.

Dasharath et al. (2016) investigated the mechanical properties and fracture mechanics of low stacking fault energy ultrafine grained Cu-9.6%Zn brass alloy, processed by MAF, at cryogenic temperature. After 12 cycles of cryoforging, the sample was found to develop fine equiaxed subgrains. This is accomplished by the formation of mutual cross bands and accumulation of huge dislocation to form dislocation cells. Maximum yield strength of the material was found to be 680 MPa after 12 cycles

Gupta et al. (2015) conducted MAF on high leaded tin bronze. The effect of MDF after 3, 6 and 9 passes on homogeneity and refinement in terms of dislocation density, twin spacing and their division, has been studied using high-resolution transmission electron microscopy (HRTEM). X-ray diffraction peak broadening was used to find the grain size, which decreased to 90 nm after 9 passes.

Joshi et al. (2016) investigate the mechanical properties of cryo-forged Al 2014 alloy. It was found that mechanical properties improved at cryogenic conditions, because of effective retardation of dynamic recovery at cryogenic temperature. Cryo-forged samples showed an increment of 7% in tensile strength and 3% in yield strength over room temperature-forged samples upto a cumulative strain of 2.4 (4 cycles). Room temperature MAF processed samples showed reduction in dislocation density and dislocation tangling zones, due to dynamic recovery, as compared to cryo-forged alloy samples.

Liu et al. (2015) investigated multi-axial compression behavior of Cu-Al alloys with varying Al content. When Al is increased, stacking fault energy promotes deformation twinning and shear banding, and finally reduces the grain size to 100 to 200 nm for 1,

2 and 4 wt% Al and 65nm was the grain size obtained for lowest stacking fault energy for 6 wt% of Al alloy.

Lu et al. (2006) obtained high- strength and high-conductivity Cu–Fe–P–B–Ce alloy, which was strengthened by cold working and aging. Mechanical properties and electrical conductivity of Cu–Fe–P and Cu–Fe–P–B–Ce alloys were measured. Traces of B and Ce could significantly increase the recrystallization temperature of Cu–Fe–P alloys, which made it possible to obtain good combination of precipitation strengthening and cold working hardening. Cu–Fe–P–B–Ce has excellent properties like tensile strength of 509 Mpa, elongation of 16% and conductivity of 80% IACS.

Li et al. (2016) investigated structural, elastic, mechanical anisotropy and thermodynamic properties of tetragonal Cu-Ti intermetallic ICs by using a first-principle density functional theory (DFT). Tetragonal Cu-Ti is one of the ductile materials, and the brittleness of tetragonal Cu-Ti ranks as follows: Cu-Ti > Cu_4Ti_3 > $CuTi_2$ > Cu_3Ti_2 > CuTi and is shown in Figure 2.9. The Debye temperature and minimum thermal conductivity of Cu-Ti increases along Cu_4Ti_3, Cu_3Ti_2, $CuTi_2$ and CuTi alloys in the same sequence. These parameters are useful to predict new intermetallic materials for high-temperature applications.
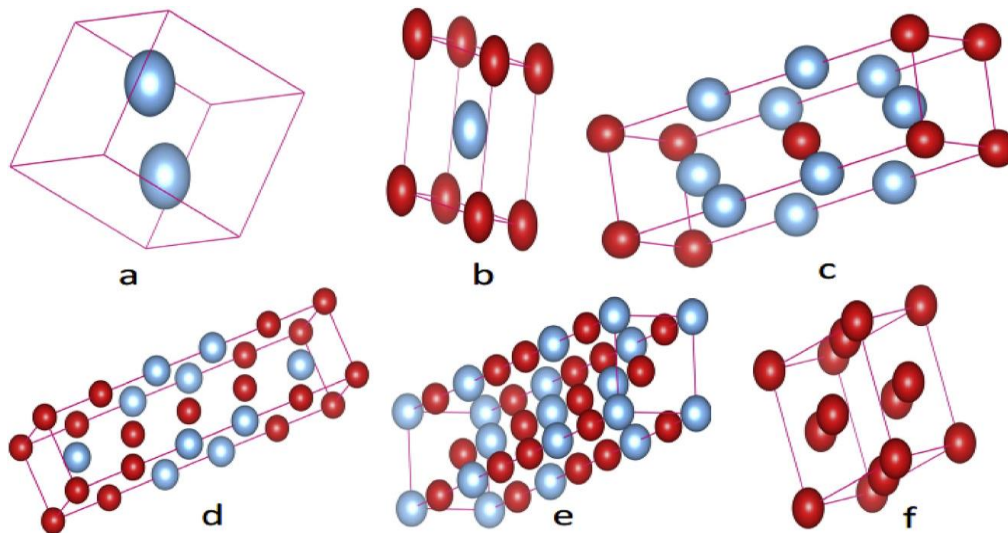
Figure 2.9 Crystal structure of Cu-Ti intermetallic compound (a) Ti, (b) CuTi (c) $CuTi_2$ (d)Cu_3Ti_2 (e) Cu_4Ti_3 (f) Cu (Yong et al. 2016).

Nakao et al. (2007) performed multi directional forging of pure copper at -196° C and 27° C. Samples processed at -196° C showed better grain refinement, which was because of the effect of deformation twins. Strength and hardness were high at -196° C, because of accumulation of high strain energy and increase in nucleation sites developed during MDF at cryogenic temperature to high strain.

Nagarjuna et al. (1995) studied the effect of grain size and titanium content on the flow stress at room temperature for solution-treated Cu-Ti alloys. It was found that Hall-Petch relation was valid for the four compositions tested: Cu-1.5 wt% Ti, Cu-2.7 wt% Ti, Cu-4.5 wt% Ti and Cu-5.4 wt% Ti alloys. As titanium % increased, strength of material also increased.

Variation of mechanical properties and electrical conductivity of Cu–Ti alloys of four compositions, viz. Cu–1.5 wt%Ti, Cu–2.7 wt%Ti, Cu–4.5 wt%Ti, and Cu–5.4 wt%Ti, has been studied in solution treated (ST), solution treated peak aged (ST+PA), and solution treated cold worked peak aged (ST+CW+PA) conditions by Nagarjuna et al. (1999). In ST condition, Ti was found to be a potential solid solution strengthening agent of copper, showing greater effect than other elements like Zn, Ni, Al, Si, Be, and Sn. YS and UTS increased significantly with volume fraction of Cu_4Ti, β precipitate. Cu_4Ti, β precipitate in as-quenched and PA condition and CW in ST+CW+PA condition contribute significantly to the strength of Cu–Ti alloy.

Szkliniarz et al. (2016) investigated the effect of strain rate and temperature on Cu-3Ti, by hot rolling. Samples were subjected to uniaxial hot compression in the range of 700 to 900ºC, and at strain rate of 0.1, 1.0 or 10.0 s^{-1} until 70% (1.2) strain. Recrystallization level and average diameter of recrystallized grains increased with temperature and strain rate. Enhancement of recrystallization level and grain refinement increased of the alloy subjected to hot deformation.

Shakhova et al. (2014) investigated the effect of multi directional forging on Cu-Cr-Zr alloy in both solution treated and aged conditions upto a strain of 4, at temperatures of 27° C and 400° C. After 10 forging passes (to a total strain of 4), at 27° C, mean grain sizes of 1.4 μm and 1.2 μm, were obtained in solution treated and aged samples,

respectively. Grain size of samples processed at 400° C was found to be 0.9 μm and 0.6 μm, respectively, in the solution treated and aged conditions.

Sakai et al. (2009) carried out the MDF experiment on FCC materials (Copper and Aluminum). Evolution of equiaxed fine grains was accelerated by MDF with change in loading direction during each pass, because of the formation of deformation bands in various directions, which resulted in grain fragmentation, followed by full development of a new grained structure with high-angle boundaries.

Semboshi et al. (2017) investigated the dependence of grain boundary distribution for Cu-4Ti % polycrystalline alloy of average grain size of 100 μm (on nucleation of cellular discontinuous precipitates). In an alloy, over-aged at 450° C, cellular discontinuous precipitates consisted of Cu solid solution and stable Cu_4Ti lamellae, nucleated at grain boundaries. Electron backscatter diffraction analysis revealed the presence of discontinuous precipitation reactions, preferentially occurred at random grain boundaries with a $\sum$value of more than 21. According to the coincidence site lattice theory, few cellular discontinuous precipitates nucleated at low-angle and low-$\sum$ boundaries, particularly twin ($\sum$ 3) boundaries. These finding suggest that the nucleation of discontinuous precipitates are closely correlated with grain boundary character and structure.

Vendra et al. (2017) investigated the mechanical behaviour and grain refinement of coarse grained (60μm) Al6063 alloy processed by Cryo MAF and Rolling. Strain rate sensitivity was estimated using tensile and compression test data at different strain rates. Microstructural analysis using EBSD showed that, increase in forging passes led to increase in dislocation density in highly deformed materials, which led to the formation of ultrafine grains, with high angle boundaries. Hardness increased from 60HV to 116HV, tensile strength reached 337MPa and fracture toughness increased from 8.32MPa $m^{1/2}$ to 13.78MPa $m^{1/2}$.

Zhao et al. (2019) studied the effect of different temperatures and strain rates on grain refinement during MDF process. Al-Zn-Mg-Cu alloy was processed at 300° C to 400°C for two different strain rates. Grain refinement was mainly controlled by dynamic

recrystallization. As per continuous dynamic recrystalization mechanism, increase in MDF temperature and decreases in strain rate resulted in grain refinement.

(b) Ferrous alloys

Bhowmik et al. (2012) investigated the microstructure and texture evolution in interstitial-free (IF) Steel processed by Multi-Axial Forging. Grain size reduced from 22 µm (starting material) to 0.3 µm after 4 cycles of MAF. Maximum strength of reached to 600 MPa after 4 cycles. After first cycle, neither increase in the strength, nor the dislocation densities, were noticed in the material and ductility decreases.

Ghosh et al. (2016) studied the effect of temperature on microstructure and mechanical properties of IF steel processed by MAF. Microstructure was analyzed using TEM and EBSD. At 650°C, MAF showed the maximum YS of 601 MPa and UTS 628 MPa with average grain size being reduced from 260 µm to 27 µm. When temperature increased, grain refinement was observed, which reduced the strength and hardness of the sample.

Kumar et al. (2016) conducted cyclic channel die compression on 304L austenitic stainless steel, in warm condition and used EBSD to study the evolution of ultrafine grains and grain boundary characteristics. Grain size was reduced from 15 µm to 0.4 µm, 0.25 µm, for one and two cycles of MDF, respectively, at 500°C.

Padap et al. (2009) investigated the mechanical properties of low carbon steel processed by MAF at 500 °C. UTS increased from ~357 MPa to ~606 MPa for 3 pass and 791 MPa for 9 pass. Hardness increased from 120 HV to 234 HV for 3 pass and 253 HV for 9 pass.

(c) Other alloys

Huang et al. (2016) carried multi direction forging on AZ31 magnesium alloys at two different temperatures (300°C and 400°C). With the increase in MDF passes, YS both at the center and edge regions, first increased and then reduces due to, twin induced dynamic recrystallization, as compared to the edge region. Microstructure evolution occurred at the center, as well as, on the edge of MDF processed sample. Mechanical properties at the center of sample are more superior as compared to side of sample.

Miura at el. (2018) performed MDF on commercially pure titanium at room temperature upto a cumulative strain of 2.0 without cracking. Ultrafine grains of 400 nm were formed, because of mechanical twinning. Hence, kinking strength increased to 710 MPa with 21 % ductility. In second step, same samples were subjected to rolling, grain size further reduced to 100 nm and strength increased to 930 MPa.

Wrought magnesium alloys were subjected to MAF at 400° C by Salandari-Rabor et al. (2016) to investigate microstructure and mechanical properties. After the first pass of MAF, UTS increased from 267 MPa to 460 MPa. With further increase in number of passes, UTS decreases, due to texture weakening. However, reduction in YS (425 to 339 MPa) and UTS (460 to 395 MPa) was observed, when number of passes were increased. Average grain size decreased from 38 μm (at initial state) to 4.8 μm after five MAF passes, due to the occurrence of recrystallization during multi-axial forging.

Sharath et al. (2016) used MAF to process Zinc alloys at 100°C and 200°C, at strains of 0.6 and 1.2. After three passes of MDF at 100°C, UTS increased from 185 to 267 MPa, with increased ductility to 14% and after 6 passes at 200°C, UTS of 267 MPa was obtained. Grain size was reduced from 30 to 2 μm for 3 pass at 100°C and reduced to 1 μm for 6 pass at 200°C.

Wang et al. (2016) obtained ultrafine grained of titanium alloy processed by multi-directional forging at 450℃. Microstructures and micro-textures in the deformed titanium specimens, were investigated by optical microscopy, electron backscattered diffraction technique (EBSD), and transmission electron microscopy (TEM). Titanium specimen experiences recrystallization softening at cumulative strain of 1.2. After six passes, with a cumulative strains of 2.4, coarse grains refined from about 25 μm to about 0.2 μm. Several roughly parallel deformation micro bands develop and intersected each other, while grain misorientations increased with increase in of straining. Grain refinement in Ti during multi-directional forging was dominated by continuous dynamic recrystallization which was enhanced by mechanical twinning bands.

(d) Effect of grain refinement on Wear behavior

UFG are harder than coarse grains, hence higher wear resistance. These UFG materials are used as wear resistant parts, like bearings, engine valve seats and gears. Wear rate is directly related to the hardness of material. When grain refinement occurs, hardness also increases due to increase, in grain boundaries. Kluge et al. (1989) studied the wear behavior and concluded that the relation between wear resistance and hardness was not simple. But experimental results of six different hardness values concluded that wear resistance increased with hardness. Kim et al. (1999) conducted wear study on ISI 1045 steel and the effect of ductility was studied. Specimen with high ductility showed more wear resistance than low ductile materials.

Some of literatures were reported on effect of SPD on wear behavior. SPD has directly affected hardness, as well as, ductility and are explained below.

Chegini et al. (2015) conducted wear test on Al-7075 alloy by pin-on-disc dry sliding test under different load condition (10 N, 20 N and 30 N) with constant sliding speed. Obtained results showed that the wear resistance improved significantly, because of grain refinement during ECAP process. Weight loss rate increases with increase in applied load. Wear mechanisms observed are adhesive wear and delamination wear.

Gao et al. (2008) performed equal channel angular extrusion (ECAE) of Cu–10%Al–4% Fe alloy at high temperature. After 2 passes of ECAE, hardness and strength increased, due to grain refinement. Because of increase in hardness, wear rate decreases and wear resistance increases, due to grain size reduction and arrangement of second phases. As the number of passes increased, frictional coefficient decreased.

Hu et al. (2015) conducted dry sliding wear test on AZ31B magnesium alloy, processed by direct extrusion and extrusion shear (ES). Results showed that wear resistance of ES processed alloy was higher, as compared to direct extrusion, due to high refined microstructure. Friction coefficients and volumetric wear rate of ES processed alloy were lower than that of the direct extruded alloy. Wear mechanism was found to be abrasion sliding, deformation and oxidation delamination.

Purcek et al (2014) observed the effect of ultrafine grains and ageing treatment on wear behavior of Cu-Cr-Zr alloy. Volume loss increased with increase in sliding distances.

When hardness increased, volume loss decreases, according to Archard's approach. Different wear mechanism like adhesive, abrasive, oxidative and delamination were observed. Minimum weight loss was obtained for Equal channel angular extrusion (ECAE), with additional ageing, because of high strength and hardness.

Ramesh et al. (2019) performed pin-on-disc wear test on MDF processed Mg-Zn alloys (2%Zn, 4%Zn and 6 %Zn). Wear was analyzed using two loads (10N & 20 N) and two sliding distances (2000 m & 4000 m) with a constant velocity 3 m/s. Wear resistance increased with increase in MDF passes and increased with %Zn, due to improvement in hardness. Wear mass loss increased with increment in load and decreased with increment of MDF passes.

Sharifzadeh et al. (2015) investigated wear and corrosion resistance of pure magnesium processed by friction stir extrusion. Microstructure of extruded samples had lower friction coefficient and enhanced the wear resistance. Extruded surface possessed good surface finish and fine grains improved the corrosion resistance of the produced samples.

Wang et al (2012) investigated the micro wear behavior of pure titanium processed by high pressure torsion. Coarse grained Ti samples showed extensive plastic deformation, which led to the formation of wedge, producing large wear debris, whereas ultrafine grained samples of Ti were dominated by abrasive wear and produced small wear debris. Deformed samples showed less wear rate and more homogenous wear groove, as compared to unprocessed samples

Wang et al. (2011) performed wear tests on aluminium alloy (Al-1050), processed by ECAP. Coefficient of friction was almost constant for both ECAP processed and unprocessed samples. But, wear resistance increased with increase in number of ECAP passes, due to increases in hardness. Wear mass loss was increased with increment of load. Wear resistance increases with ECAP passes, due to grain refinement and inherent loss of a strain hardening capability.

Xu et al. (2013) carried out ball-on-disc dry sliding wear test on ECAP processed AZ31 magnesium alloy. ECAP processed samples led to reduction in fluctuations of the coefficient of friction (COF) due to enhancement of mechanical properties. Wear mass

loss was found to reduce in ECAP processed samples. Micro wear mechanism was identified as a mix of abrasive wear and oxidation wear. Width of the wear track for ECAP processed samples was small, as compared to unprocessed samples, due to increase in hardness.

(e) Effect of grain refinement on Corrosion behavior

Argade et al. (2012) conducted corrosion studies on Mg-Y-RE wrought magnesium alloy. UFG microstructure showed highest polarization resistance and positive pitting potentials and repassivation potentials, as compared to, coarse grained microstructure. During constant immersion testing, lower corrosion rates were observed for UFG samples compared to coarse grain samples

Huan et al. (2018) investigated the corrosion behavior of Cu-Ti alloys in 3.5% NaCl solution and studied the variations when Ti content is varied. Cu matrix (Ti dissolved) changed the corrosion behavior where compared to pure Cu, that showed active-passive and trans-passive corrosion.

Hadzima et al. (2009) observed that the ECAP processed AZ31 magnesium alloys showed higher charge transfer resistance compared to cast alloy, during electrochemical impedance spectroscopy. Fine-grained microstructure influenced the corrosion resistance.

Li et al (2011) processed Cu-4% Ti alloy at different aging conditions and investigated the corrosion behavior. Both pitting and inter-granular corrosion were observed over the surface of sample. Traces of Cu and precipitates of β-Cu_4Ti were found in the refined microstructure in alternate layers, which improved corrosion resistance and enveloping effect, was developed. \

Mostaed et al. (2014) studied corrosion behavior on ECAP processed ZK60 magnesium alloy by electrochemical measurements and immersion test, in phosphate buffer solution. Results showed improved corrosion resistance in ultra-fine grained (UFG) alloy compared to extruded material. Increase in corrosion resistance is due to secondary phase refinement and redistribution.

Ralston and Birbilis (2010) conducted a review on magnesium and other alloys

regarding the effect of grain size on corrosion. Grain refinement increased the corrosion resistance of magnesium alloys. The primary reason for improvements in corrosion resistance is attributed to improvement in passive film formation and adhesion due to increased grain boundary density.

Wang et al. (2003) investigated the potentiodynamic polarization effect and electrochemical impedance spectroscopy (EIS) of copper using 3.5% NaCl and observed inhibition of Domperidone on copper. It was concluded that domperidone played the role of anodic inhibitor with 94 % efficiency. SEM and AFM images showed copper corrosion that was inhibited due to absorption.

2.6 Gaps found from literature survey

Above critical review of literature showed that by using MAF technique, grain refinement can be achieved for non-ferrous metals. However, more studies are required on MAF processed materials, in view of change of strain path associated with MAF, which makes it an interesting SPD process to study. Based on the applications in the field of electrical, automobiles, and aerospace industries, there is a requirement of good electrical conductivity, high yield and tensile properties and also wear resistance properties of copper alloys. Cu-Be alloys have highest strength, corrosion resistance, wear resistance, but the major disadvantages are high prices and toxic properties. Beryllium compounds are hazardous during melting, casting, pressure welding, and welding, hot deformation, cutting and grinding. The best substitutes for Cu-Be seem to be binary Cu-Ti alloy. Cu-Ti-X alloys demonstrate mechanical properties and conductivity, comparable to those of Cu-Be. limited work has been reported on Cu-Ti alloys processed by SPD and No work is reported Cu-Ti alloy processed at cryogenic condition. Moreover, no work is reported on wear behavior of Cu-Ti alloy by MAF.

Objective of present work is to understand the mechanisms of refinement occurred in microstructure during cryogenic MAF of copper alloy with varying percentages of titanium (1.5%, 3%, and 4.5%). No reported work exists in the literature that attempts to investigate the multiaxial cryo-forging on Cu-Ti alloys.

2.7 Objectives

Based on the developments in the area of copper alloys with SPD process using MAF technique, following objectives have been derived.

a) To develop ultrafine grained materials by using multiaxial cryo-forging.
b) To study the microstructural changes of Cu-Ti processed by MAF at cryogenic temperature.
c) Investigation of mechanical properties of as-received and MAF processed Cu-1.5%Ti, Cu-3%Ti and Cu-4.5%Ti alloys.
d) To study the wear behaviour of as-received and MAF processed Cu-1.5%Ti, Cu-3%Ti, and Cu-4.5% Ti alloys.
e) To investigate the corrosion studies of as-received and MAF processed Cu-1.5%Ti, Cu-3%Ti, and Cu-4.5% Ti alloys

CHAPTER 3

3. EXPERIMENTATION

Flow chart in Figure 3.1 shows the materials used, material processing technique and characterization techniques. Different characterization techniques used to study as-received and MAF processed samples are optical microscopy, scanning electron microscopy, electron back scattered diffraction, transmission electron microscopy and X-ray diffraction. Mechanical testing like tensile test, hardness, wear study and corrosion properties were performed on both as received and MAF processed samples.
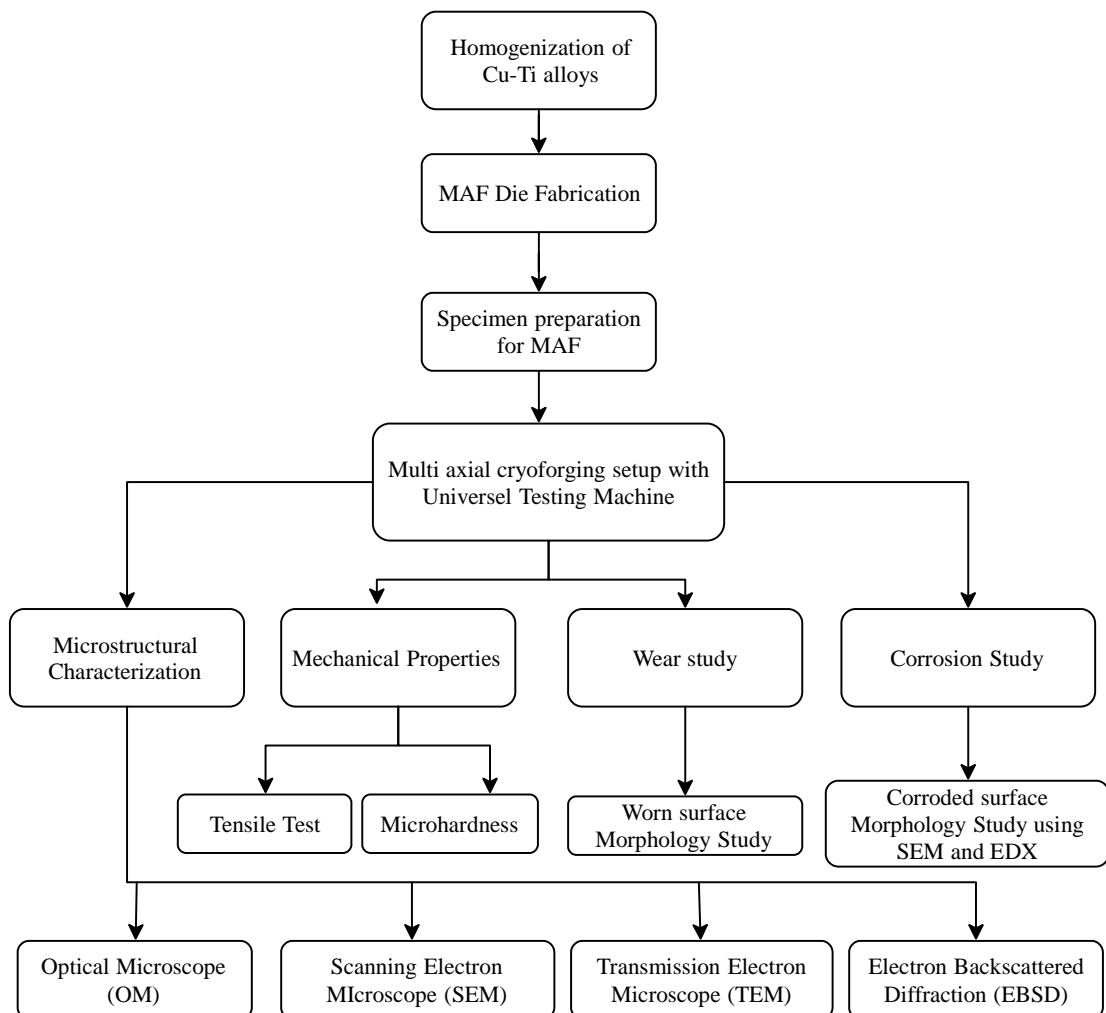
Figure 3.1 Flow chart of present work

3.1 Materials

Cu-Ti alloys, of composition Cu-1.5%Ti, Cu-3%Ti and Cu-4.5%Ti, were procured from Pahwa Metal Tech Pvt. Ltd, Pune. Nominal composition of alloy is shown in Table 1. The alloy components are cut into small cuboidal sample size of 30 mm $\times$ 30 mm $\times$ 25 mm. The cut samples are homogenized at 850°C for 24 hrs. The homogenized alloys are considered as as-received material.

Table 1 Nominal composition of Cu-Ti series alloys (weight percentage)

Alloy	%Ti	%Mn	%	%Sb	%P	%Pb	%Ni	Cu
Cu-1.5%Ti	1.5	0.03	0.15	0.01	0.08	0.01	0.02	Balance
Cu-3%Ti	3	0.04	0.18	0.02	0.06	0.01	0.02	Balance
Cu-4.5%Ti	4.5	0.03	0.13	0.01	0.07	0.02	0.01	Balance

3.2 Experimental Setup

(i) Multi axial Cryo-forging

Multi axial Cryo-forging (MACF) is one of the severe plastic deformation processes to produce ultrafine grains. Samples are forged at liquid nitrogen temperature, because of which, dynamic recovery is suppressed in the sample and strain is retained in the material.

Multi axial cryo-forging setup consists of following equipments

- 100 Ton Universal Testing Machine
- Forging die
- Liquid nitrogen Container
- Safety equipment and digital Vernier caliper

UTM of 100 Tons capacity was used for forging process. Samples was compressed in the die forging for each pass. UTM used in the present work is shown in Figure 3.2

Figure 3.2 Universal Testing Machine used in the experimental process.

Forging die was designed based on plane strain condition using Solid edge 19 V modeling tool. The exploded and assembled views of forging die are shown in Figure 3.3 (a) - (b). According to plane strain condition, deformation occurred in two directions and deformation in third direction is zero. Forging die was made of hot die steel (HDS) and consist of 4 parts: one base plate, two side plates and one plunger fixed with four bolt nut assembly. The die was heat-treated to maintain the hardness of 52 HRC. Final die assembly and die parts are shown in Figure 3.4.
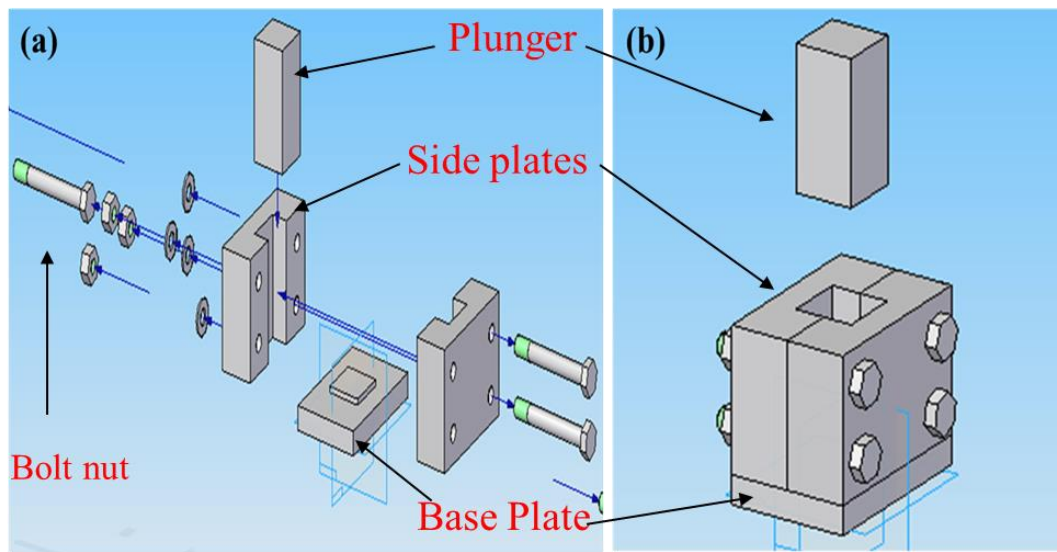
Figure 3.3 CAD model of (a) Exploded view (b) Assembled view
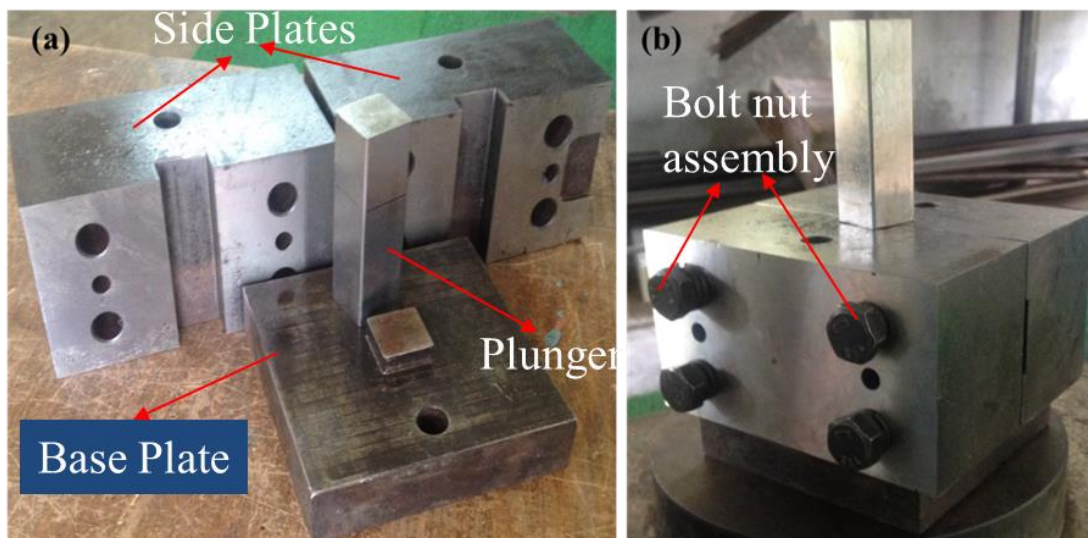
Figure 3.4 MAF dies after machining (a) Exploded view (b) Assembled view

Liquid Nitrogen (LN$_2$) container, of 10 litres capacity, was used to store nitrogen throughout experiment. Sample holder was used to keep the sample inside the LN$_2$ container as shown in Figure 3.5.
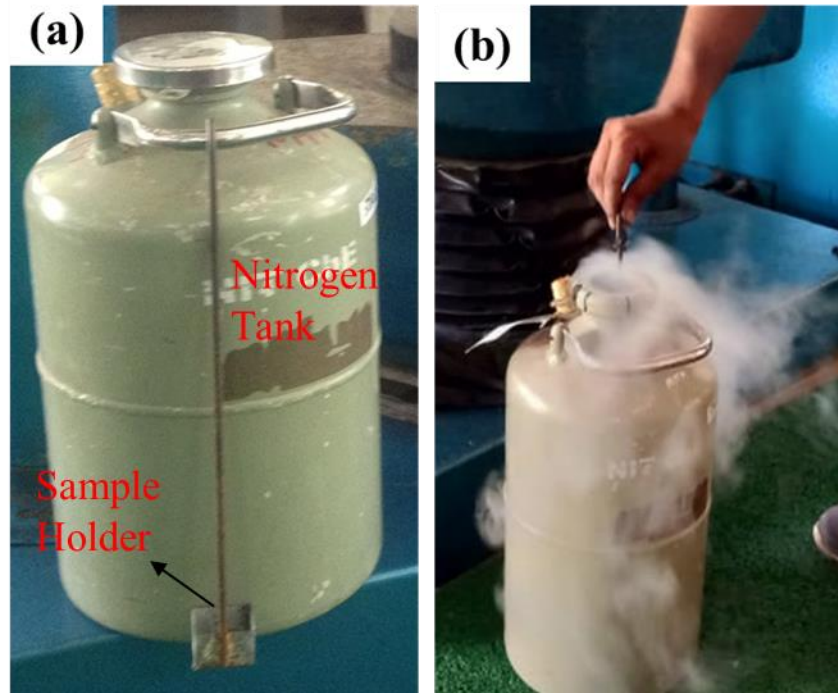
Figure 3.5 Liquid nitrogen contained (a) Nitrogen Container with sample holder (b) Sample keeping inside container.

- Set of gloves was used to handle cryogenic sample during forging.
- Molybdenum-disulfide (MoS_2) is used as a lubricant during forging, to avoid friction between the die and sample.
- Digital Vernier caliper was used to measure the dimension of the sample before and after each pass of forging to maintain consistency.

(ii) Experimental procedure

Prior to forging, samples were machined to a dimension of 30X30X25 mm^3, as per die design, and homogenized Schematic diagram of the multi axial cryo-forging process is shown in Figure 3.6.

- Before forging, die was cleaned to remove residues of previous forging operation and washed with acetone.
- Samples are marked X,Y and Z on three mutually perpendicular directions for easy identification of direction of forging.
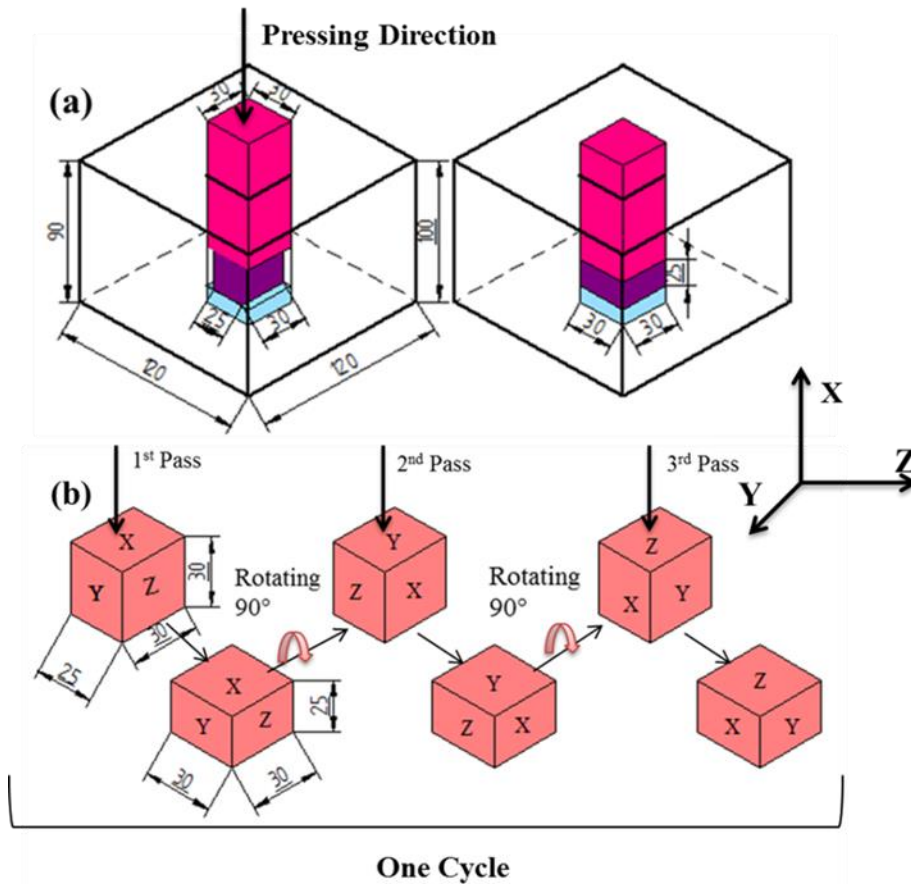
Figure 3.6 Schematic diagram of MAF process (a) Process figure (b) Process notations

- As-received samples were dipped in liquid nitrogen for 20 minutes to attain the saturation temperature of liquid nitrogen until the formation of bubbles is stopped. Schematic of nitrogen treatment to sample as shown in Figure 3.8.

- Longer edge of the sample is kept in the die cavity, such that the surface marked X is facing the upper. Load is applied on the sample at a constant speed of 0.03mm/s, so as to maintain the directions in the ratios of 1:1:1.3. During forging, sample temperature was around -120°C to -80°C.

- During forging, strain is accumulated in the material, the imposed strain is given by $\varepsilon = \ln\left(\frac{h_0}{h}\right)$, where h_0 is initial height and h is the final height of the sample.

  - Strain accumulated in one pass (X- direction) is $\varepsilon_x = \ln\left(\frac{30}{25}\right) = 0.182$
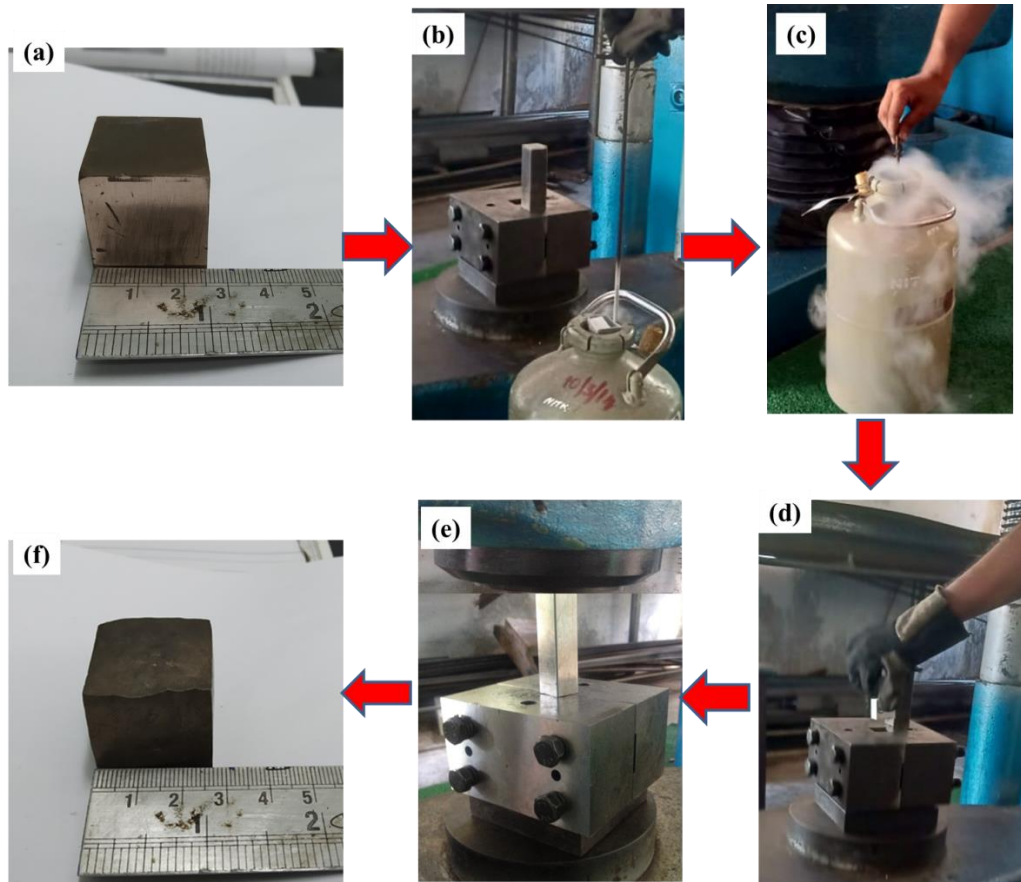
Figure 3.7 Die set up and MAF process (a) as-received (b) die position (c) sample processed in liquid nitrogen (d) placing the sample inside die (e) pressing the sample (f) MAF processed sample.

- Forged sample is immersed in liquid Nitrogen for 5 minutes. The sample is rotated by 90° and placed in the die, such that surface on which Y is marked, is facing the plunger. The schematic diagram of MAF process notation as shown in Figure 3.6 (b).

Strain accumulate in second pass (Y- direction) is $\varepsilon_Y = \ln\left(\frac{30}{25}\right) = 0.182$

- Same procedure is repeated, by keeping the samples which is marked Z, facing the plunger and forged. This completes one cycle of MAF process.

Strain accumulated in the third pass (Z- direction) is $\varepsilon_z = \ln\left(\frac{30}{25}\right) = 0.182$

Total accumulative strain in one cycle is ε_1 cycle= $\varepsilon_x + \varepsilon_Y + \varepsilon_z$

Cumulative strain in one cycle is ε_1 cycle= 0.182+0.182+0.182=0.546
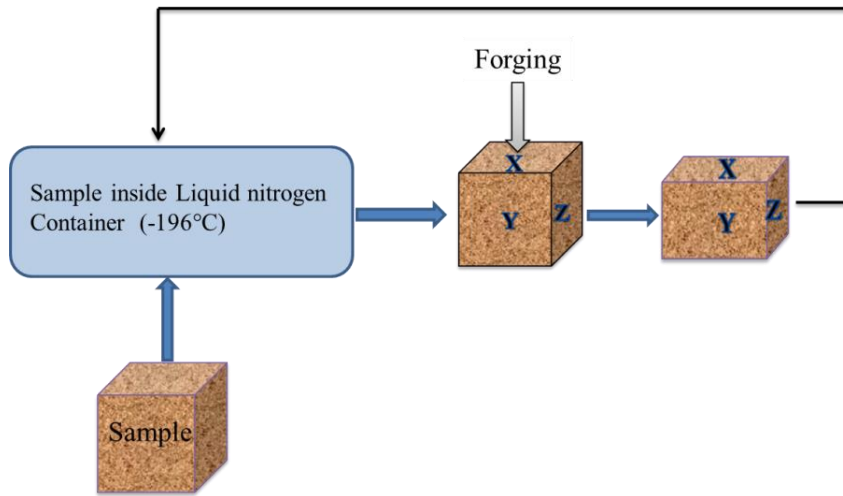
Figure 3.8 Schematic of nitrogen treatment of smaple for MAF process.

- MAF is performed upto 3 cycles. After each cycle, samples are subjected to various testing processes, which will be discussed in following sections and chapters. Cumulative strains, after 2 and 3 cycles are found to be 1.092 and 1.638, respectively. Photograph of experimental process, as-received and one cycle MAF processed samples are shown in Figure 3.7.

3.3 Microstructural characterization

For microstructural characterization and mechanical testing, sample is cut from the middle region in a plane perpendicular to the forging axis of the final pass of the MAF cycle, which is schematically shown in Figure 3.9.
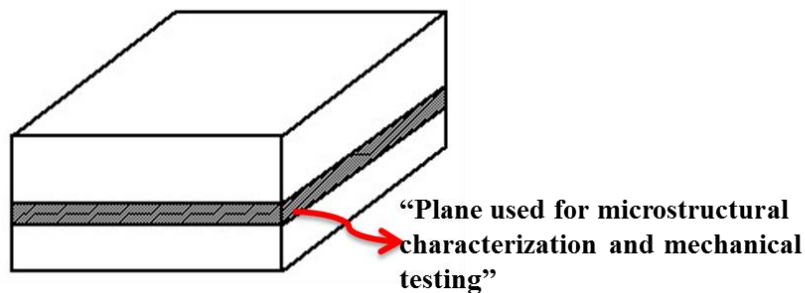
Figure 3.9 Schematic of section used for microstructure and mechanical testing

(i) Optical Microscopy

Microstructures evaluation of as-received Cu-Ti cast alloy (Cu-1.5%Ti, Cu-3%Ti, Cu-4.5%) and samples after MAF process are investigated by using an optical Microscope (OM) and Scanning Electronic Microscope (SEM) with electron diffraction spectroscopy (EDS). Samples for microstructural analysis is selected and sliced as shown in figure 3.9. This portion was selected to avoid any inhomogeneities. Cross-sections, perpendicular to final pressing direction of MAF processed samples, are prepared by mechanical polishing using silicon carbide abrasive papers (grades of 400, 800, 1000, 1200, 1500, 2000). Further, samples were polished using Al_2O_3 as abrasive to get finer finish and finally washed using acetone. Polished, samples were etched using a solution of 10g $K_2Cr_2O_7$, 5ml H_2SO_4, 10 drops of HCL and 95 ml of distilled water (Nagarjuna et al.2008). Samples were etched around for 3 seconds and dried immediately using the dryer. Microstructures of the etched samples were examined using optical microscope (OM) and is shown in Figure 3.10.
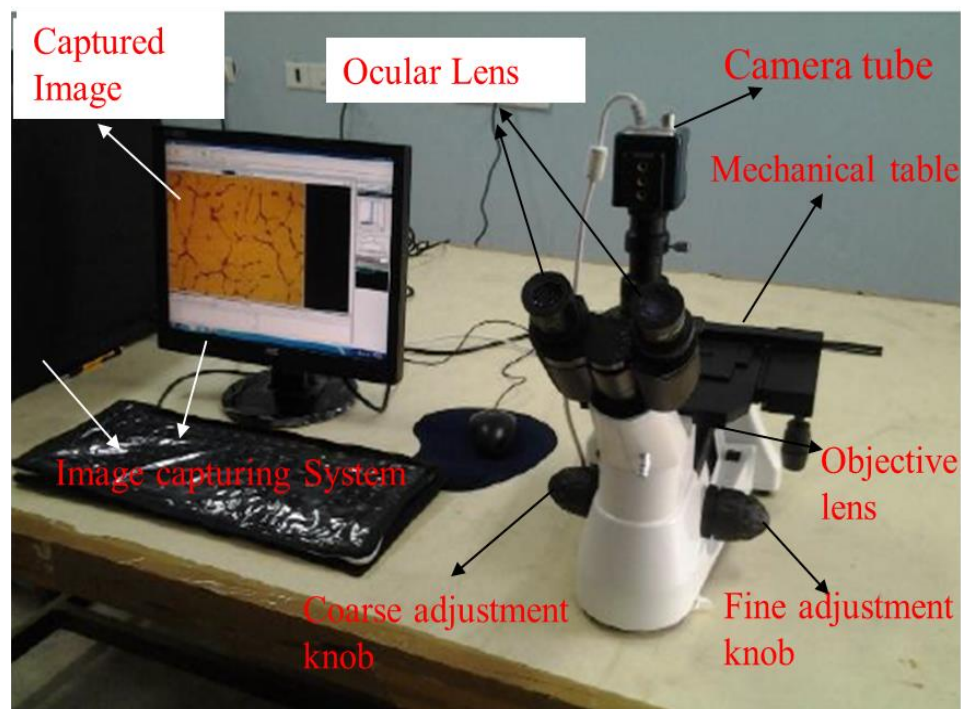
Figure 3.10 Optical microscopy

(ii) Scanning Electron Microscopy (SEM)

Scanning electron microscope (Figure 3.11) makes use of interaction between high energy electron beam and specimen to obtain microstructure. In the present work. microstructure and surface topography were studied using scanning electron microscope (SEM) of Model- JSM-6380LA, JEOL.
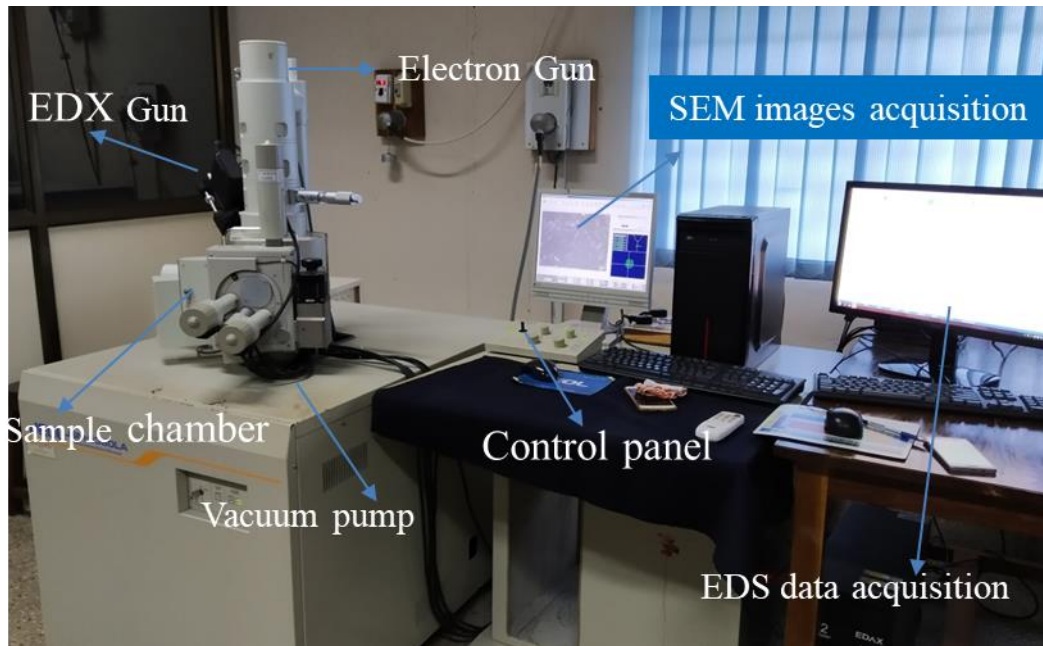
Figure 3.11 Scanning electron microscope with EDS attachment

(iii) Electron back scattered diffraction (EBSD)

Microstructures of as-received and MAF processed samples was analyzed using electron backscatter diffraction (EBSD) using Field Emission Scanning Electron Microscope (JEOL JSM-7100F) (Figure 3.12), for grain structure and grain boundary misorientation angles. Middle portion of the samples was cut into small pieces using diamond wheel cutter and mounted using Acrylic powder and acrylic liquid. Mounted samples are mechanically polished using silicon carbide abrasive paper grades of 400, 800, 1000, 1200,1 500, 2000. Finally, cloth polishing was done using alumina colloidal solution. For Orientation Image Mapping (OIM) characterization, additional electro polishing was done using Struers D2 electrolyte at 10 V for 15 s, at a temperature of - 25 °C to achieve strain free surface. D2 electrolyte solution containing 20% phosphoric acid (H_3PO_4), 50% distilled water, 25% ethanol, propanol 5% was used as electrolyte solution for electropolishing. EBSD was done using Oxford instruments 'Nordlys'

detector attached to 'Zeisis EVO50' SEM. EBSD patterns were acquired at accelerating voltage 20 keV with step size of 1 μm and EBSD camera binning mode was 4X4, area of scan was 465 X 347 mm^2 and Kikuchi patterns were indexed for Cu phase. Obtained results were analyzed using HKL Channel 5 software.
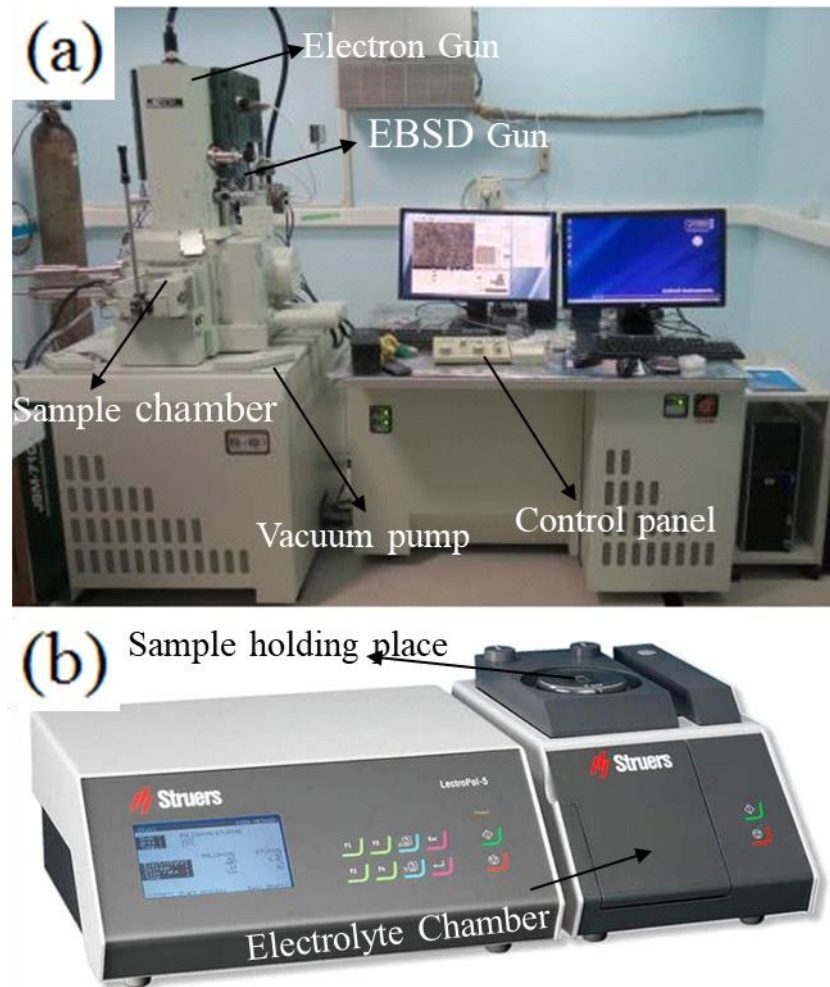
Figure 3.12 (a) FE-SEM (b) Struers electro polishing machine

(iv) Transmission Electron Microscope (TEM)

TEM-JEOL-JEM 2100 (Figure 3.13) was used to analyze the Microstructure of samples processed by MAF. Sample preparation involves mechanical polishing of the sliced samples to ~30 to 40 μm thickness. Polished samples were punched to discs having diameter 3 mm, followed by dimpling to reduce the thickness to ~5-10 μm. Finally, further thinning was carried out using ion milling (Gatan–PIPS 691) on the dimpled sample.

Figure 3.13 Transmission Electron Microscope

(v) X-ray diffraction

X-ray diffraction (XRD) technique was used to find out the elemental phases present in as-received and MAF processed samples. In the present work, JEOL, JDX-@P-XRD model (Figure 3.14), equipped with diffractometer having Ni filter activated at 20 mA and 30 kV through Cu-kα radiation, was used. Samples were scanned at a rate of 2° per minute and diffraction angle (2θ) ranged between 30° to 90°.
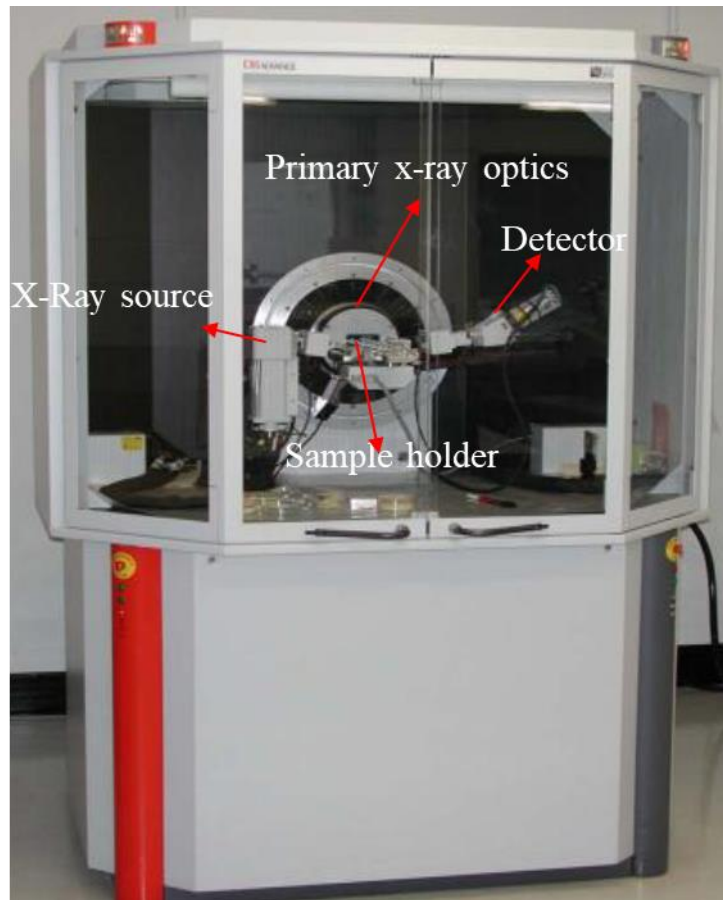
Figure 3.14 X-ray diffraction

3.4 Mechanical testing equipment's and procedure

(i) Tensile testing

Tensile test was performed on as-received and MAF processed samples using Shimadzu (AG–X plus™-100 kN) universal testing machine as shown in Figure 3.15. Tensile specimens were cut from center portion of MAF processed samples and prepared as per ASTM E-8M standards cylindrical dog bone shape samples with 16 mm gauge length were fabricated from MAF processed samples. Photographs of tensile sample before and after testing are shown in Figure 3.16 (b). Testing machine maintains a constant strain rate of 0.5 mm/min at room temperature for all samples. For each condition, 3 samples were tested and average is considered. Schematic diagram of ASTM E8M sample as shown in Figure 3.16 (a).
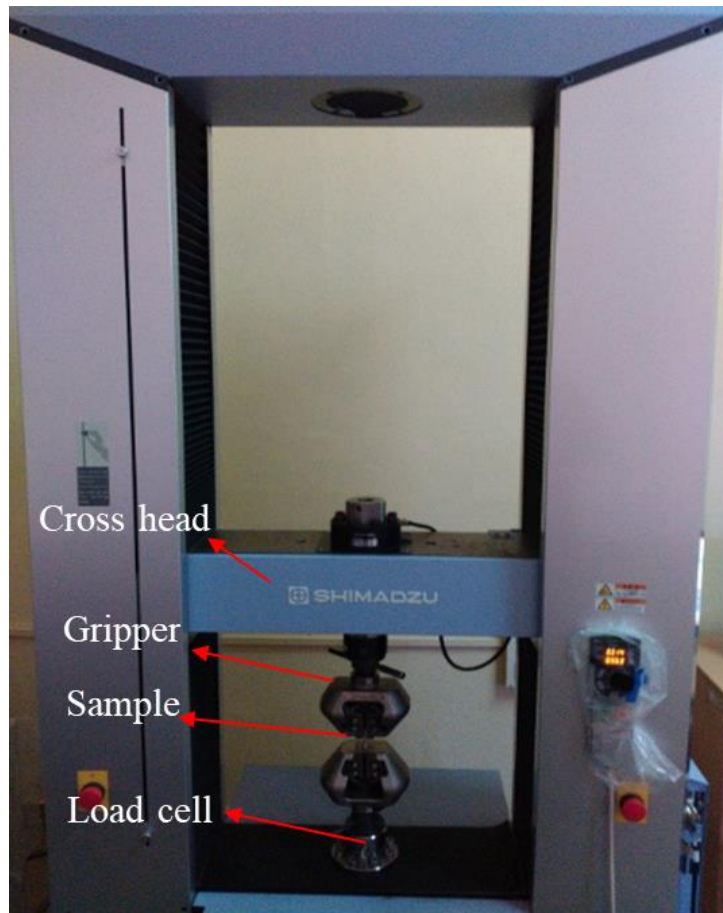
Figure 3.15 Shimadzu Tensile Testing Machine
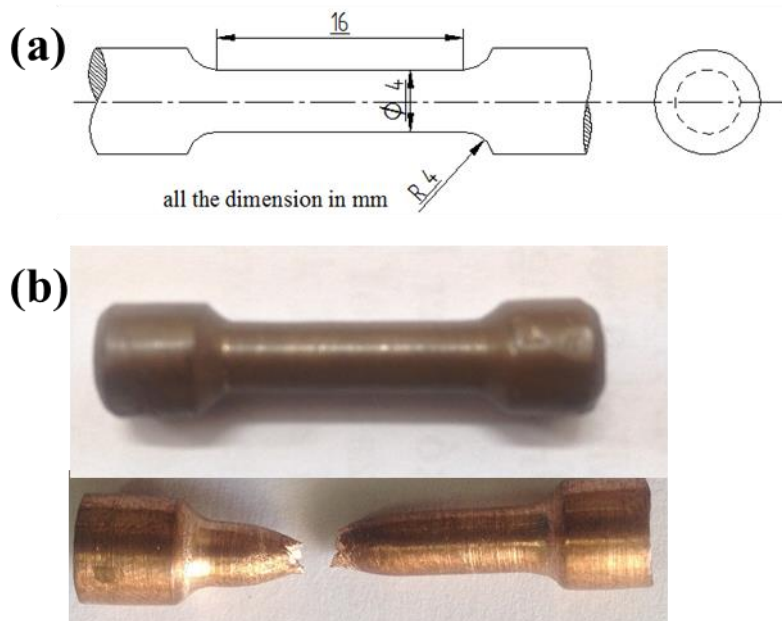
Figure 3.16 Schematic of tensile sample before and after tensile testing

(ii) Microhardness Tester

Hardness values of as-received and MAF processed samples are obtained by subjected the samples to Vickers microhardness tests. Vickers Tester, Omni Tech, MVH-S-Auto, Maharashtra, India, used for the analysis shown in Figure 3.17. Samples used for OM analysis are used for hardness analysis. Vickers microhardness was measured in a plane perpendicular to the final forging axis by applying a load of 100 g for 15 s dwell period. Indentations were taken at 15 different locations and average value was considered.
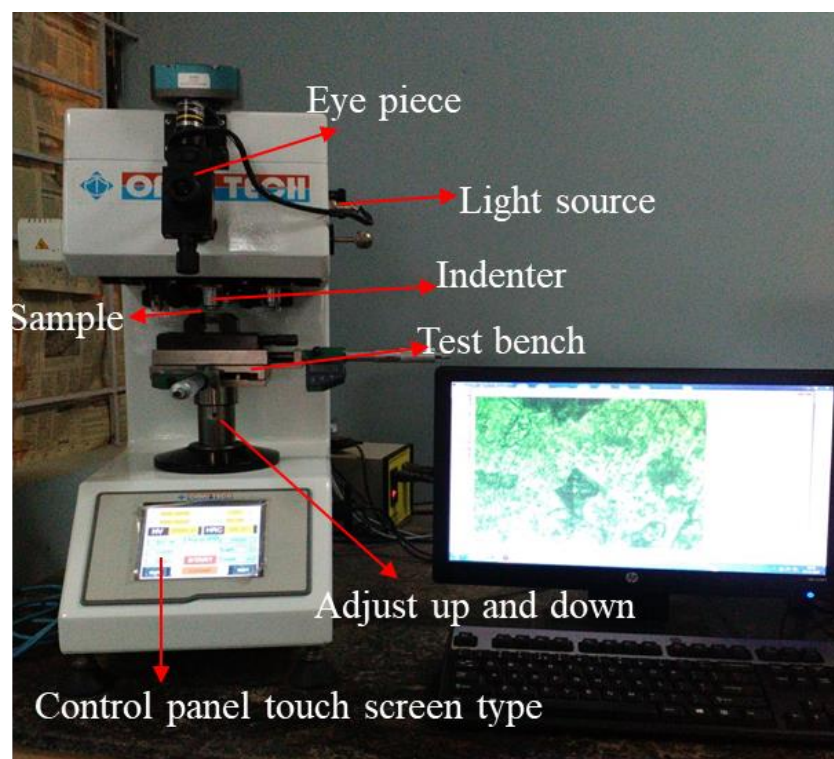
Figure 3.17 Vickers microhardness Tester

3.5 Pin on Disc Wear Testing Machine

Wear tests were performed at room temperature under dry sliding condition using pin-on-disc tribometer (DUCOM-TR-20LE-PHM 400-CHM 600) (Figure 3.18). Specimens were prepared by taking the central region of the unprocessed and ECAP processed samples. Specimens were turned using lathe machine to a diameter of 6 and length of 28 mm, as per ASTMG99-05. Tests were carried out on hard and polished disk (EN31 steel) coated with alumina and HRC 65hardness. Prior to wear test, samples

were ground with SiC papers (1500 and 2000 grit) and followed by cleaning using ultrasonicator for 5-10 min and finally dried and polished to produce mirror finish surface. Cu-Ti alloy samples were exposed to 10 N and 20 N with a sliding distance of 500 m, 1000 m, 1500 m, 2000 m, 2500 m and 3000 m at a speed of 1 m/s and 2 m/s, with track diameter 114 mm. For each test, disc surface was cleaned with SiC paper (1500 grit) and followed by washing using acetone, to remove wear debris from the surface. Worn surface was analyzed using SEM and EDX. X-ray diffraction (XRD) was used to find the phases formed on worn surface.
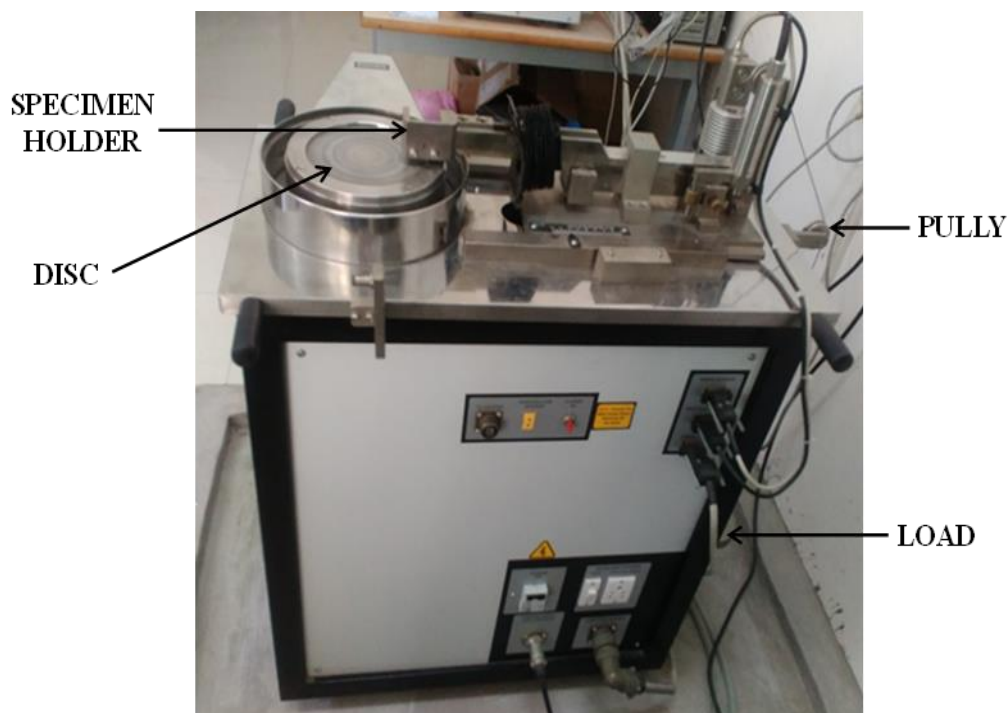
Figure 3.18 Pin-on-disc wear testing machine

3.6 Electrochemical Work Station

Samples used for electrochemical corrosion studies were mirror finished and properly cleaned. Electrochemical testing were carried out using an electrochemical workstation (EC lab-Biologic SP-150) (Figure 3.19), with a standard three-electrode system; saturated calomel electrode (SCE) as reference electrode, a platinum wire as counter electrode. Sample, with 1 cm^2 surface area exposed to solution, was used as working electrode. Aqueous solution of 3.5 Wt % NaCl was prepared using A.R. grade NaCl in distilled water and the pH of solution was maintained at 7.5. During each experiment,

sample was polished using SiC paper (400-2000 grit). Potentiodynamic polarization experiments were carried out at a scan rate of 0.5 mV/s. Cathodic and anodic portions of generated Tafel plots were accordingly extrapolated to calculate the corrosion potential (E_{corr}) and corrosion current density (i_{corr}). Electrochemical impedance spectroscopy (EIS) test were carried out in 3.5 wt. % NaCl solution at room temperature, to compare the corrosion resistance of unprocessed and MAF processed samples. EIS tests were carried out with a frequency, ranging, from 100 kHz to 10 mHz, and the amplitude of sinusoidal potential signal is 5 mV. Surface morphology of the corroded samples was examined by SEM and EDX.
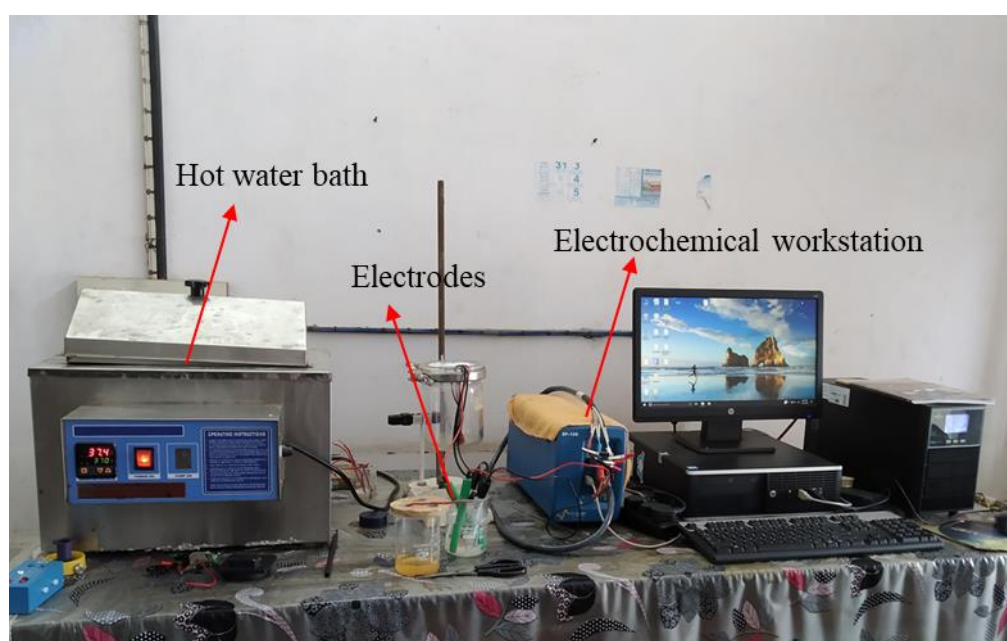
Figure 3.19 Electro chemical work station

CHAPTER 4

4. RESULTS AND DISCUSSION OF Cu-1.5%Ti ALLOY PROCESSED BY MAF

Cu-1.5%Ti alloy was processed by MAF at cryogenic temperature upto 3 cycles. Microstructures of MAF processed samples were characterized using OM and SEM. Samples processed at higher passes were observed under TEM. Microstructures are analyzed by EBSD for grain structure and grain boundaries misorientation angles. XRD was conducted to identify the different phases in the samples. Tensile test, microhardness, wear and corrosion tests were carried out for samples upto 3 cycle and the results are discussed in the following sections.

4.1 Microstructure analysis

(i) Optical microscopy

Optical micrographs of Cu-1.5%Ti alloy in as-received condition as shown in Figure 4.1 (a). As-received material shows equiaxed morphology of homogeneous grains of size 600 ± 20 μm. Figure 4.1 (b-d) shows the optical micrograph of MAF processed samples 1, 2 and 3 cycles at cryogenic temperature respectively. Figure 4.1 (e-h) shows statistics distribution of shear bands and average grain size is tabulated in table 2. After 1 cycle of MAF, strain accumulated in the sample was 0.54, deformation (shear) bands were observed in Figure 4.1 (b). With increase in number of MAF passes, shear band density increased with high dislocation density. After 2 cycles with an accumulated strain of 1.06, formation of shear bands in different directions was observed. Figure 4.1 (d) shows the microstructure after 3 cycles of MAF, which shows fine equiaxed high dislocation sub-grains at strain of 1.56. Similar results were shown by Rao et al. 2014, Dasharath et al. 2016 during severe deformation of Al6061 alloy deformed at liquid nitrogen temperature. Liquid nitrogen causes suppression of dynamic recovery and plastic strain gets accumulated in the sample. This leads to shear band formation because of accumulated plastic strain perpendicular to deformation direction during MAF process (Dasharath et al. 2017, Joshi et al.2016, Gupta et al.2016).
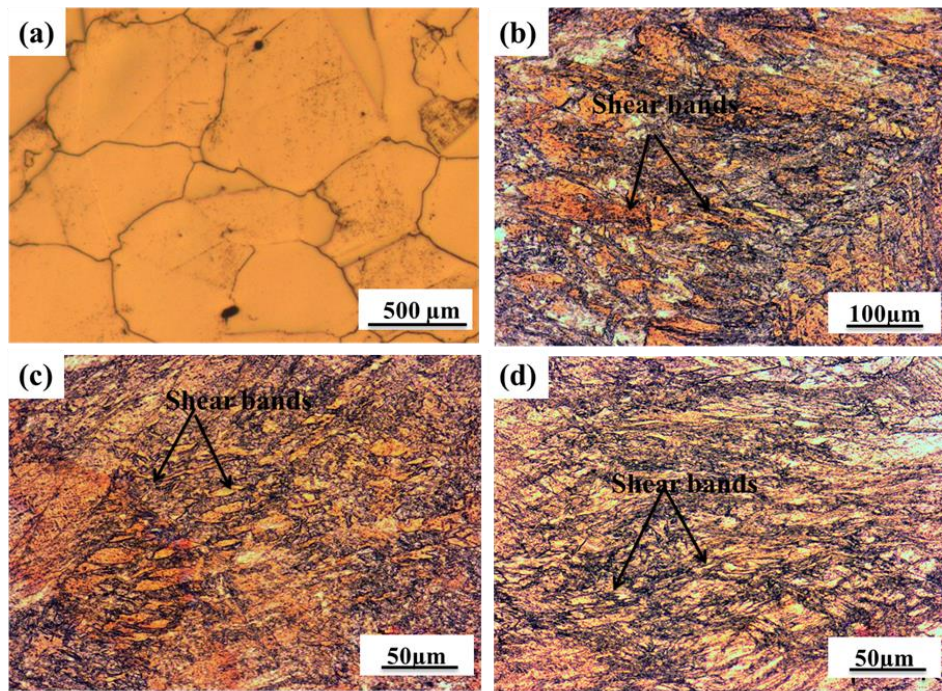
Figure 4.1 Optical microstructure of Cu-1.5% (a) as-received and MAF processed (b) 1 Cycle (c) 2 Cycle (d) 3 Cycle samples,

Deformation bands or shear bands and misorientation of band increases with number of forging passes, finally resulting in fine new equiaxed type substructure/dislocations (Dasharath et al. 2016). By conducting SPD at liquid nitrogen temperature, geometrically necessary boundaries (GNB) like deformation bands and shear bands are developed (Bay et al.1992). As strain increases, with MAF cycles, deformation or shear bands increases resulting in generation of finer grains (Beyakov et al.2000).

(ii) SEM Analysis

SEM micrographs of as-received, 1 cycle, 2 cycle and 3 cycle Cu-1.5%Ti alloy samples are shown in Figure 4.2 (a-d), respectively. As-received sample showed different phases, Cu and Cu_4Ti_3. After 1 cycle of MAF, grains are broken down and forms shear bands, which are clearly visible (Figure 4.2b). As the number of MAF cycles increases, shear bands density increases and is shown in Figure 4.2 (c-d) (Dasharath et al.2016). After 2 and 3 cycles, shear bands width decreased and high dislocation density is observed (Figure 4.2 (c-d)).
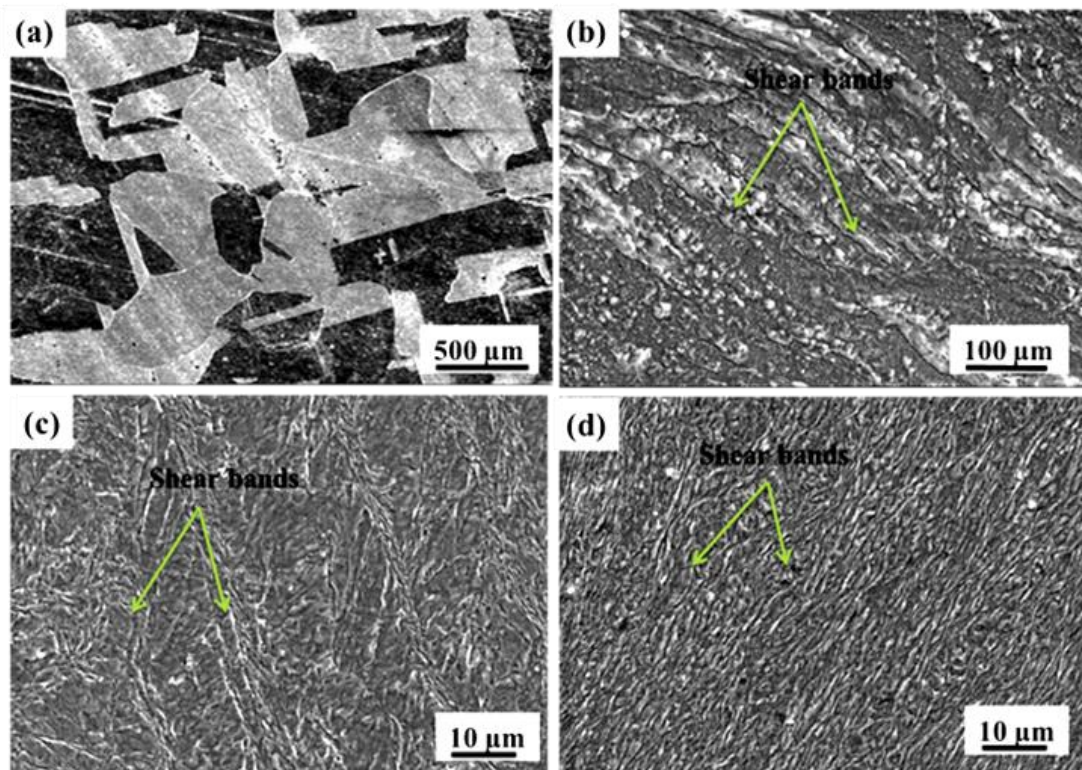
Figure 4.2 SEM images of (a) as received and MAF processed by (b) 1 cycle (c) 2 cycle, (d) 3 cycle samples

(iii) TEM Analysis

Figure 4.3 shows TEM images of samples processed by MAF 3 cycles with selected area electron diffraction (SAED) patterns in the inset. Figure 4.3 (a) shows shear bands and Figure 4.3 (b) shows high dislocation density. Both shear bands and dislocations were marked in figures with white lines. Shear bands density increases with forging passes due to accumulation of high strain. Discontinuous spotty rings with broadened and bright stretched regions on the diffraction spots are seen, because of the deviation of uniaxial grains from the elongated grains (Belyakov et al.2001, Richert et al.2001). Diffraction spots appear to be separated because of low angle grain boundaries (LAGBs).
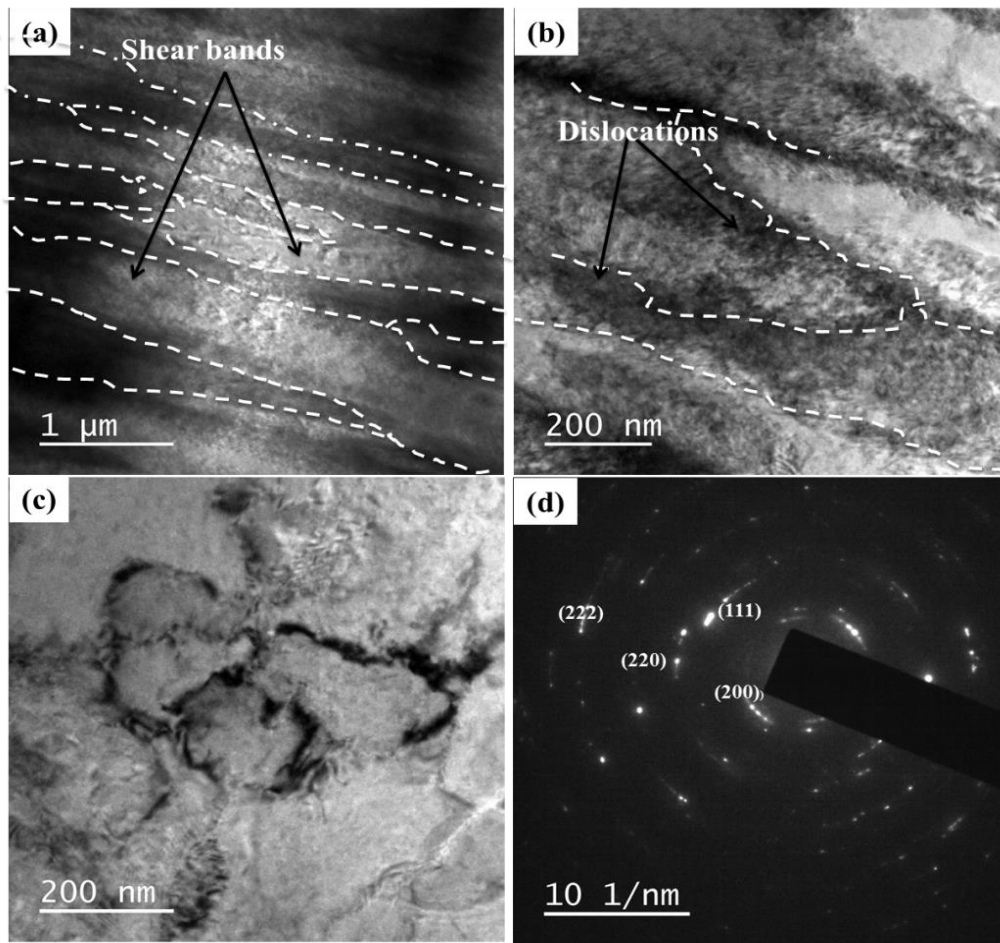
Figure 4.3 TEM micrograph of 3 cycles MAF process sample (a) Shear bands (b) Dislocations (c) Subgrains (d) SAED pattern

(iv) EBSD analysis

Figure 4.4 (a) and (b) shows OIM analyzed inverse pole figure (IPF) map of Cu-1.5%Ti as-received and 3 cycles MAF processed samples at cryogenic temperature. Figure 4.4 (c) and (d) shows OIM analyzed grain boundary map of as received and 3 cycles MAF sample. Figure 4.4 (e) shows the IPF map color to represent a corresponding crystallographic plane direction.
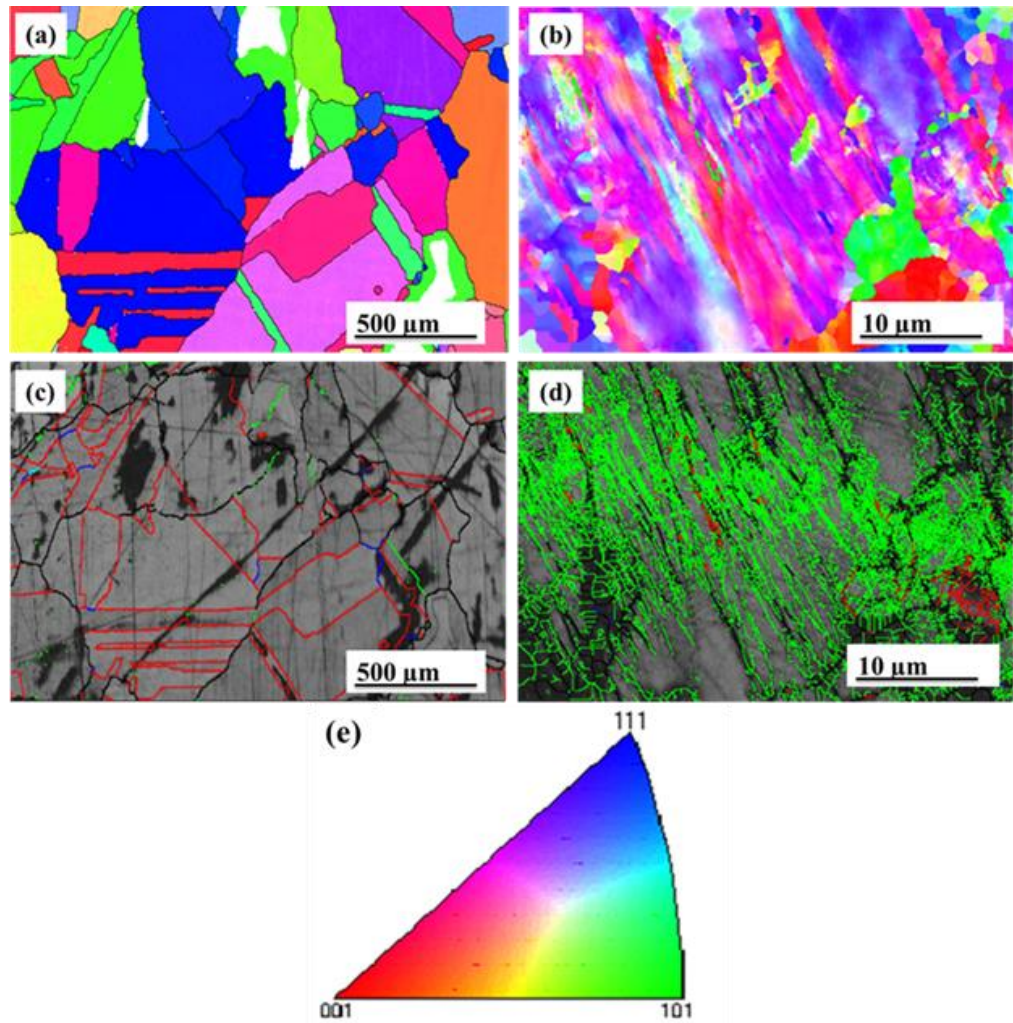
Figure 4.4 EBSD analysis of Cu-1.5%Ti alloy OIM of a) as received sample b) 3 cycle sample and Grain boundary Map of c) as received sample d) 3 cycle sample e) IPF

As-received sample consists of equiaxed fine grains with high angle grain boundaries (HAGBs). In grain boundary map, black color represents high angle boundary and green color represents LAGBs and red color represents the twin boundaries. As-received sample shows strong peaks with high misorientation angles (~60°) and have a high fraction of HAGBs (Figure 4.5 (c)). As the number of MAF pass increases, strain accumulation in sample increases. Subgrains are gradually converted from HAGBs to LAGBs and have a high fraction of LAGBs as compared to HAGBs (Figure 4.5 (d)). After 3 cycles of MAF, grains are elongated and are at small misorientation angles (<10°) (Flausino et al.2019, Kumar et al. 2015). Figure 4.5 shows distribution of grain boundaries misorientation angles of as received and 3 cycle MAF

processed samples. As received sample shows strong peaks with HAGBs. After 3 cycles of MAF, these peaks shift towards LAGBs. Rate of grain refinement is decreased at higher cycles of MAF process.
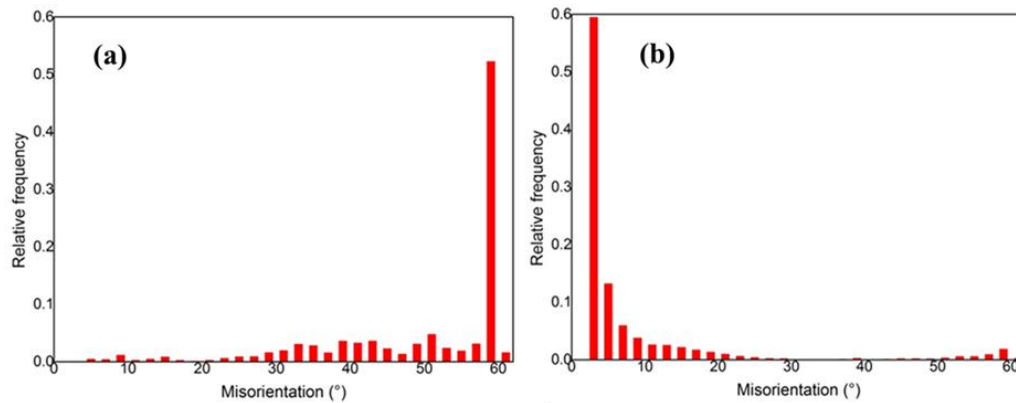
Figure 4.5 Misorintation angle of a) as received samples and b) 3 cycle MAF processed sample

4.2 X-ray diffraction analysis

Figure 4.6 shows XRD profile of as received, 1 cycle, 2 cycle and 3 cycle MAF processed samples. The intensity of planes (111), (200), (220) and (222) in as-received sample is very less. After 1 cycle of MAF, intensity of all peaks increases, peak broadening occurs and all the peaks get shifted by at least one degree which is due to grain refinement in the material. In Figure 4.6 (c), intensity of planes (111) and (200) increases and intensity of planes (220) and (222) decreases. Similarly, in Figure 4.6 (d), intensity of peaks (111), (220), and (222) decreases further and also, peak broadening is more. But, intensity of plane (200) increases drastically. These fluctuations in peak intensity and peak broadening are due to the high dislocation density in the sample (Krishna et al.2017, Gopi at al.2017).
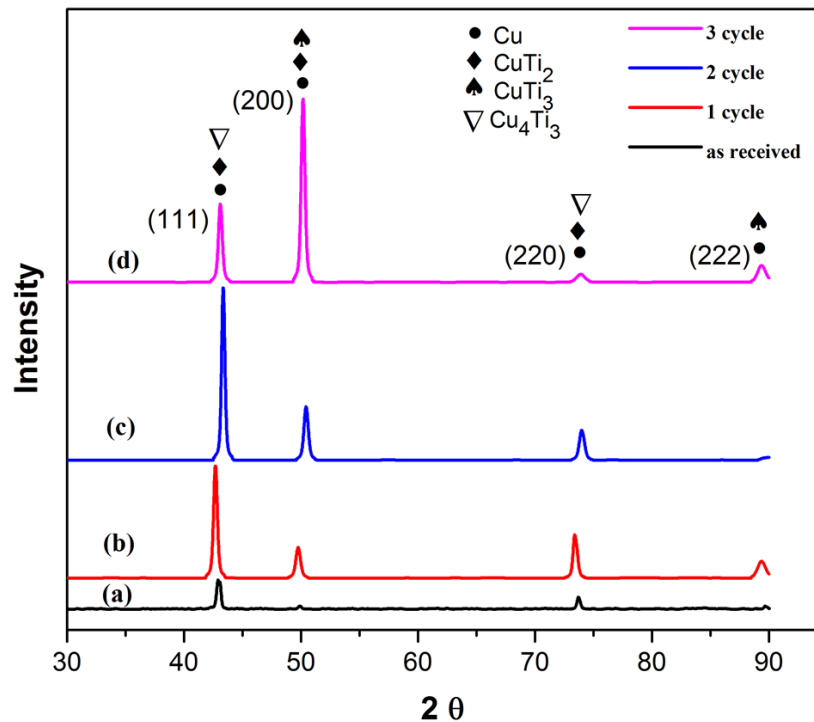
Figure 4.6 XRD peak analysis of as received and MAF processed samples

4.3 Mechanical properties

(i) Tensile behaviour

Figure 4.7 (a) and (b) show the variation of tensile properties of Cu-1.5%Ti alloy samples at different MAF passes. Three set of experiments were conducted for each cycle and average of the results are tabulated in Table 2. Stress-strain curves of as-received and MAF processed samples are shown in Figure 4.7 (a). Yield strength (YS) and Ultimate tensile strength (UTS) of the as-received sample were observed to be 56 MPa and 190 MPa, respectively, with 57 % elongation. YS and UTS subsequently increased to 210 MPa and 390 MPa, respectively, after 1 cycle of MAF with a cumulative strain of 0.56. But ductility reduced to 13%. After 2 cycles, with a strain of 1.06, strength increased to 300 MPa (YS) and 480 MPa (UTS) with 22% elongation. After 2 cycles, strength and ductility increased with increase in number of MAF cycles. This is due to initiation of nucleation of dislocations in grain boundary region and also because of interruption of dislocation movement by the precipitates formed during MAF process. Presence of bimodal grain structure with finer and coarse grains results in better strength and ductility (Kim et al. 2001, 2003, 2005, Cheng et al. 2007, Mao et

al. 2005). Maximum UTS of 596 MPa was obtained for MAF 3 cycle and 26% elongation. Increase in strength after MAF may be due to grain boundary strengthening mechanism, as per Hall-Petch Equation (Nieh et al. 1991). As the number of MAF pass increases, dislocation density also increases. Relationship between UTS, YS, % elongation and grain size are shown in Figure 4.8.
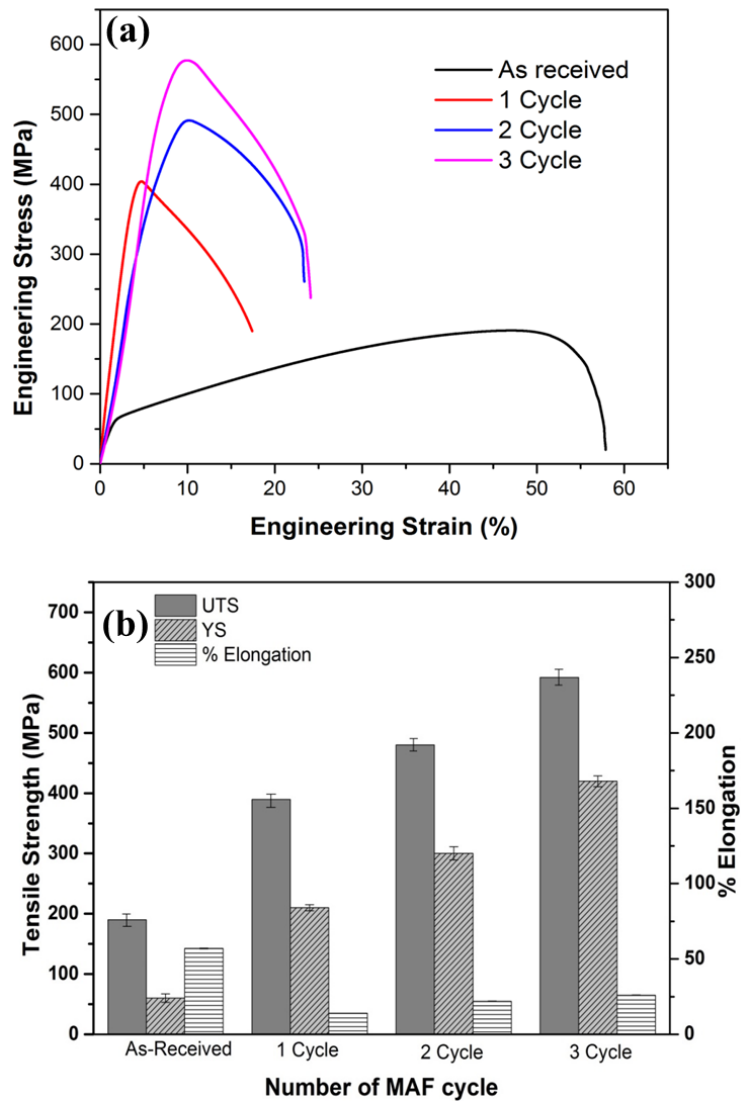
Figure 4.7 Tensile properties of as received and MAF processed samples (a) stress-strain curve (b) Bar chart.

Table 2 Mechanical properties and grain size for all the samples produced by MAF processing.

Sample No.	YS (MPa)	UTS (MPa)	Elongation (%)	Hardness (HV)	Grain Size (μm)
As-	60±7	190±8	57±.32	80±5	600±18
1 cycle	210±5	390±6	14±.13	159±4	40±9
2 cycle	300±11	480±9	22±.17	200±5	14±3
3 cycle	419±15	592±15	26±.20	211±6	2±1
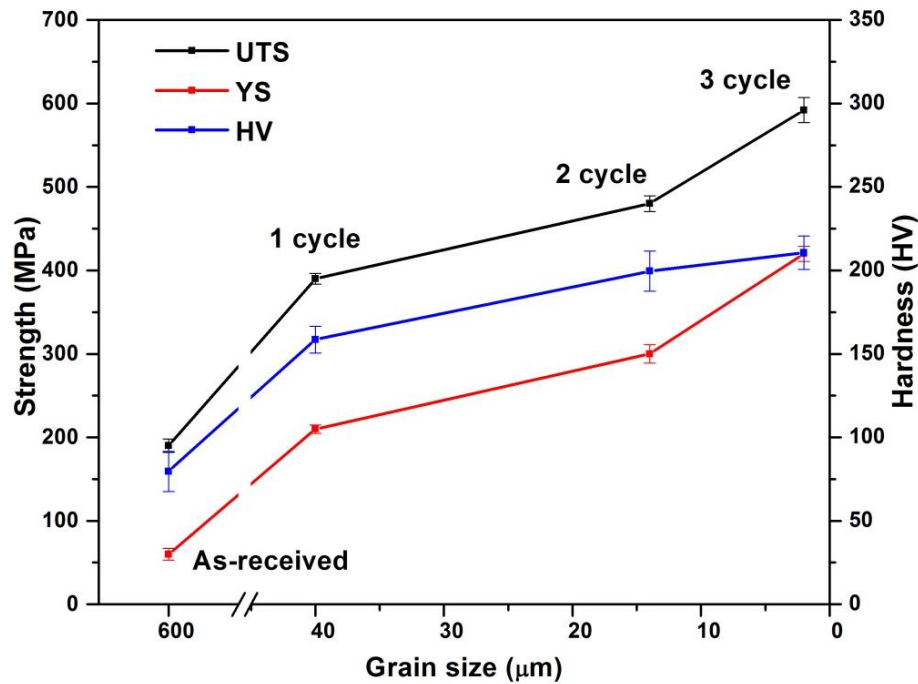
Figure 4.8 Relationship of Mechanical properties with the average grain size

(ii) Vickers Microhardness

Vickers microhardness (HV) was conducted for Cu-1.5%Ti cryoforged alloy using Omni-Tech hardness tester, by applying a load of 100 g for 15s. Indentations were made at various regions on the cross-section of the sample to know the variation of hardness distribution over the surface of deformed sample. Variations of microhardness for as-received, 1, 2, and 3 cycle samples are as shown in Figure 4.9. Microhardness of as-received material was 80 HV. MAF with a cumulative strain of

0.54 (after 1 cycle) leads to increase in hardness from 80 HV to 158 HV. At cumulative strain of 1.06 (after 2 cycles), microhardness increased to 200 HV. Maximum microhardness of 210 HV, was observed at a cumulative strain of 1.62 (after 3 cycles). With increase in number of passes, grain size decreased and hardness increases, because of strain hardening and high dislocation density. At low strain, increase in hardness value is high, as compared to high strain level, because, of high work hardening effect, at lower strain.
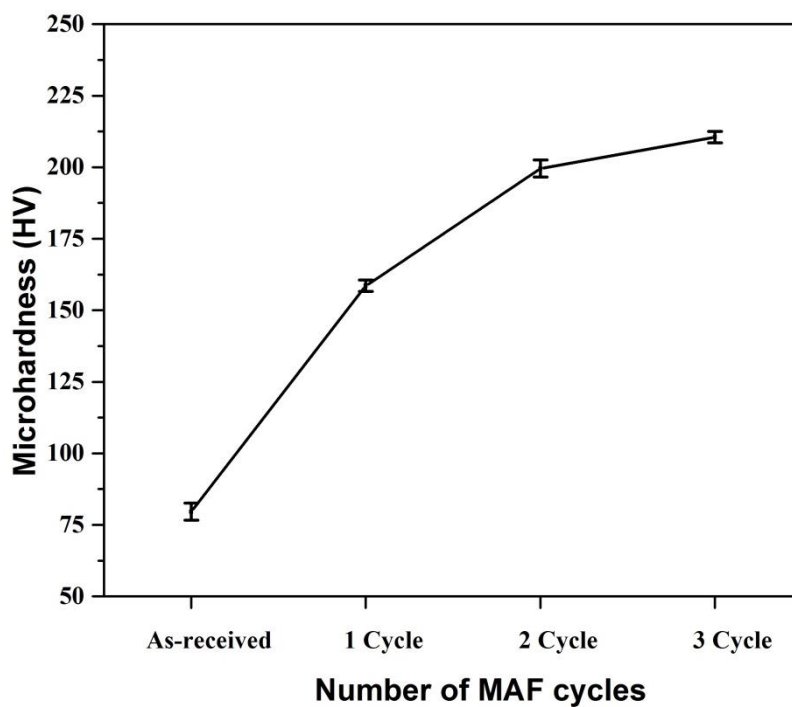
Figure 4.9 Vickers hardness of as received and different cycle of MAF processed samples

(iii) Fractography

Figure 4.10 shows SEM images of fractured surface of as-received and MAF processed samples. As-received sample fractured in a ductile manner, showing large dimples over the fractured surface (average dimple size 28 μm). After 1 cycle of MAF, dimple size decreased to an average value of 7 μm. But, after 2 and 3 cycles, dimple size increased to 12 μm and 15 μm, respectively. From the figure, fractured surfaces appeared to be smoother at higher MAF passes. Tear ridges were observed on as-received and MAF processed samples, and is shown in Figure 4.10 (a and c). This may

be because of plastic deformation at the grain boundaries and the type of fracture is mixed mode (Anne et al. 2017). As MAF cycles increase, cleavage planes decreased as observed in Figure 4.10 (c and d). Both cleavages and dimples were observed on the surfaces and appear to be a fracture of ductile-brittle type (Dasharath et al.2016). After 3 cycles of MAF, fine dimples were observed which are almost uniform in size and thus, shows ductile type of fracture.
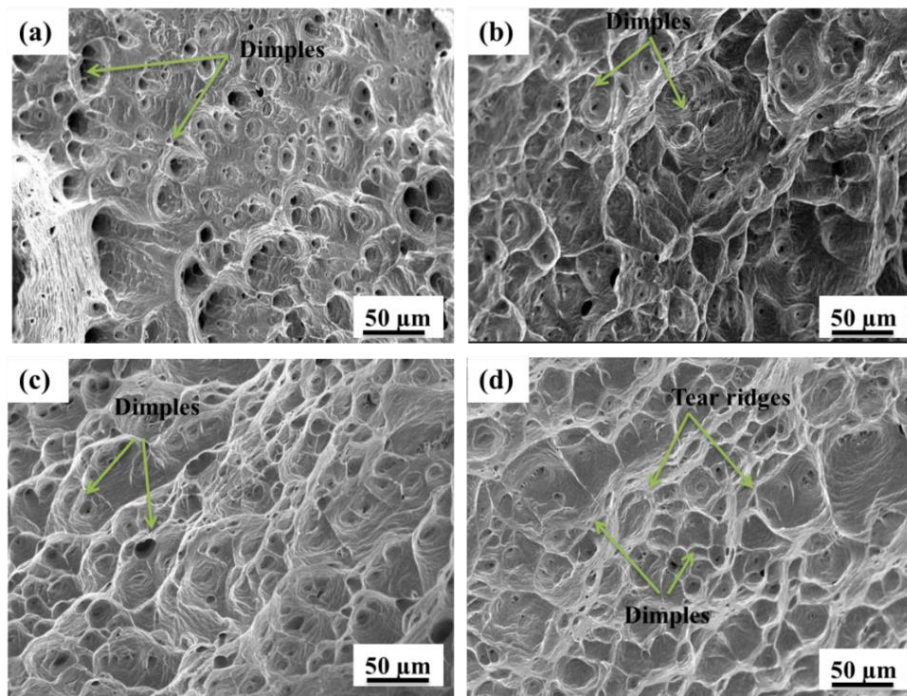
Figure 4.10 SEM micrographs of tensile test fractured surfaces for (a) as-received sample and MAF processed (b) 1 cycle, (c) 2 cycle, and (d) 3 cycle samples.

4.4 Wear Analysis

(i) Coefficient of Friction (COF)

Wear test was performed on as-received and MAF processed samples, at 10 N and 20 N, under sliding distance of 500 m, 1000 m, 1500 m, 2000 m, 2500 m and 3000 m. COF curves are plotted for different velocity and sliding distances under different loads for as-received and MAF processed samples and are shown in Figure 4.11. Variation in coefficient of friction is less for 10 N load compared to 20 N load and tabulated in table 3
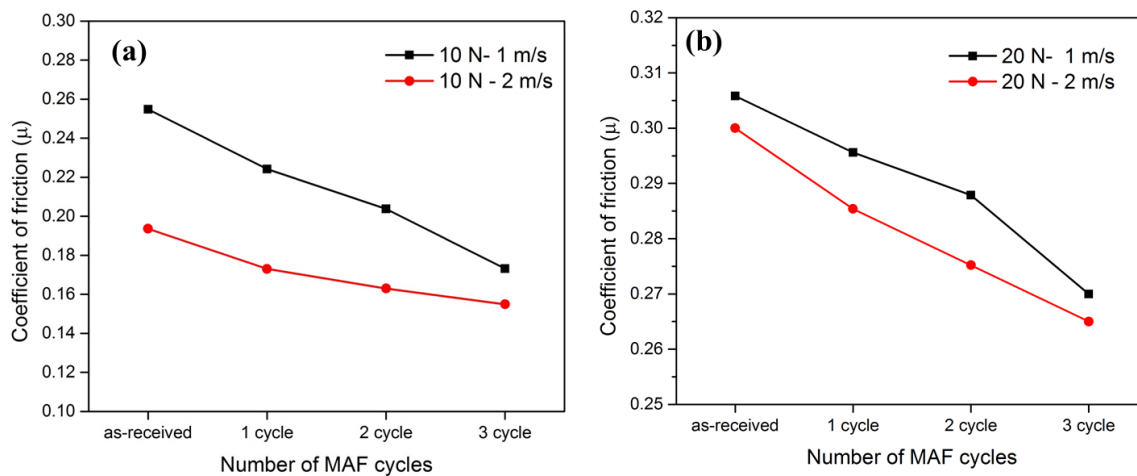
Figure 4.11 COF curves for samples under 10 N and 20 N load with sliding velocities
(a) 10 N-1m/s, 10N-2 m/s 500 m b) 20 N-1m/s, 20N-2 m/s.

Table 3. COF value for different load and different velocities.

Material/Condition	10 N-1 m/s	10 N-2 m/s	20 N-1 m/s	20 N-2 m/s
As-received	0.35	0.32	0.42	0.4
1 cycle	0.34	0.31	0.39	0.38
2 cycle	0.31	0.29	0.39	0.37
3 cycle	0.28	0.26	0.37	0.35

From Figure 4.11(b), it can be seen that improved COF values are observed for MAF processed samples, under 10 N and 20 N loads for sliding velocities. MAF 3 cycle sample showed least coefficient of friction. Above results indicate the reduction in COF values in MAF processed samples. MAF processed samples showed improvement in wear resistance because of their improvement in mechanical properties.

(ii) Volume mass loss (mm^3)

In wear analysis, volume of material lost is a function of sliding distance. Figure 4.12 shows the variation of wear volume loss with different sliding distance for both as-received and MAF processed samples.
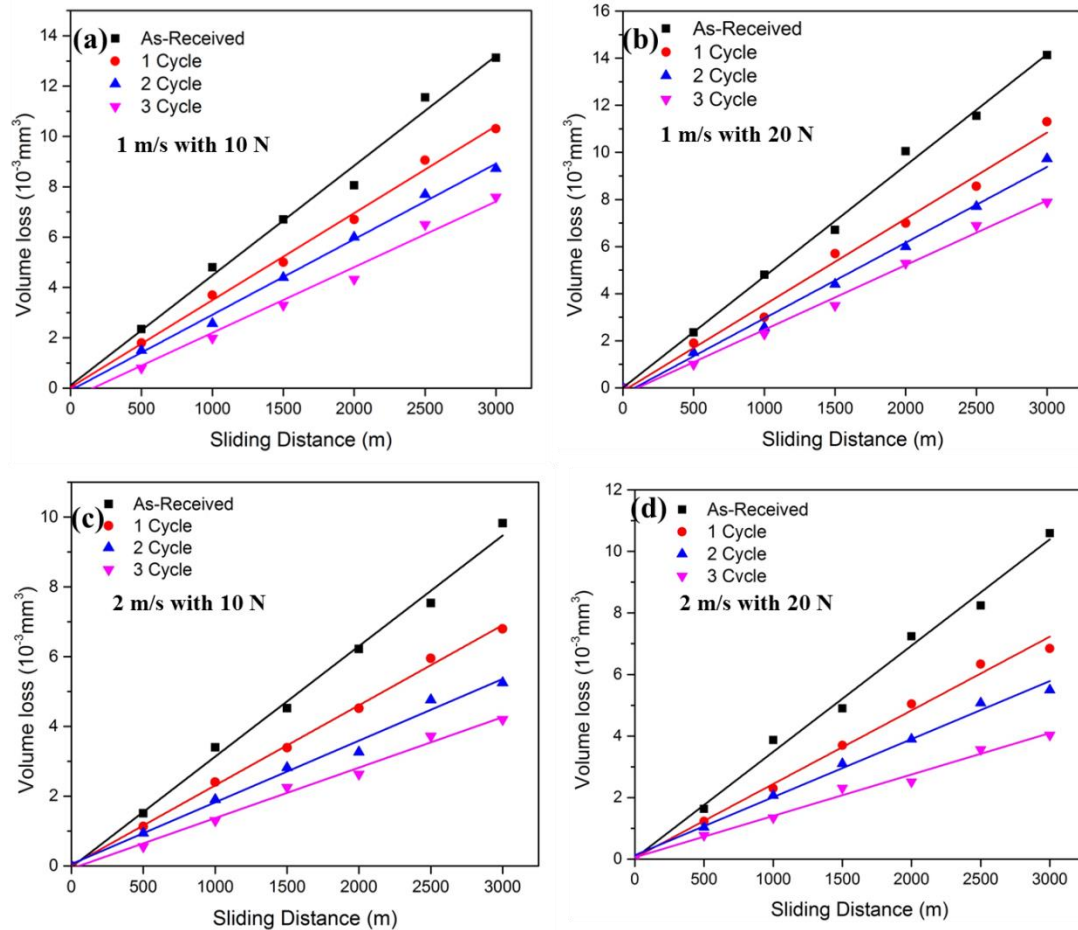
Figure 4.12 Variation of volume mass loss with sliding distance for samples processed by MAF at different loading condition.

Figure 4.12 (a) and (b) shows the variation of volume mass loss, tested at 1 m/s with two different loads. Similarly, fFigure 4.12 (c) and (d) shows the volume mass loss, at 2 m/s with 10 N and 20 N. It is observed that cumulative volume loss varied linearly with the sliding distance, for both as-received and MAF processed samples. Volume loss increased with increase in load and sliding velocity. As the number of MAF cycles increased, volume mass loss decreased due to improvement of hardness.

(iii) Wear Rate (mm^3/sec)

Wear test was conducted for as-received and MAF processed samples and the results are shown in Figure 4.13. Wear rate obtained for as-received and MAF processed samples are as shown in Figure 4.13. Tests were conducted for two different loads (10 N and 20 N) and six different sliding distances (500 m, 1000 m, 1500 m, 2000 m, 2500 m, 3000 m). It is observed from Figure 4.13, wear rate decreased, as MAF cycles increased, indicating increase in wear rate in MAF processed samples. Wear rate is less in the case of samples subjected to wear at sliding distance of 500 m when compared to 3000 m.
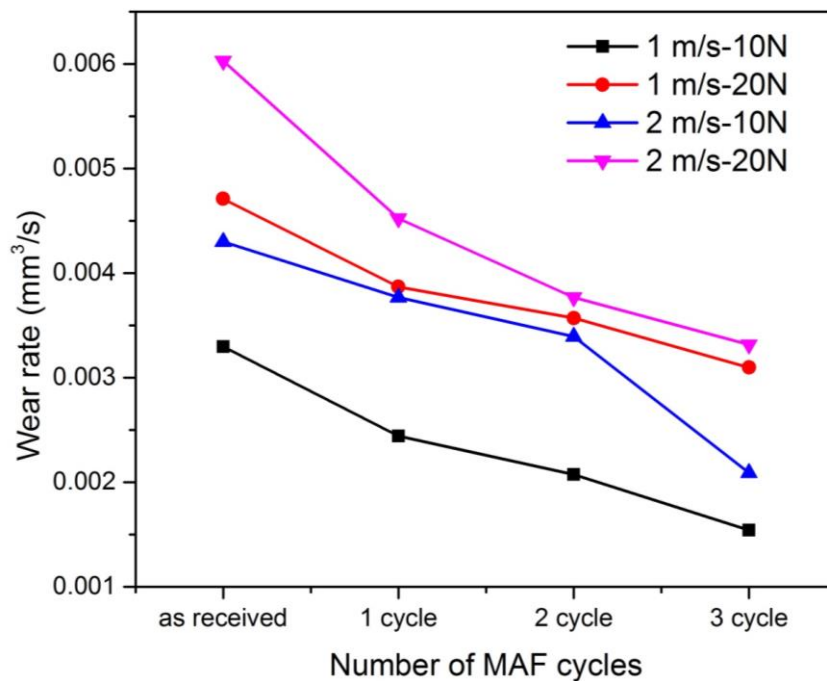
Figure 4.13 wear rate v/s MAF cycles with different loading condition

 Figure 4.13 indicate an increase in wear rate with increasing load and sliding distances for all samples. Table 4 shows wear rate at different velocities and different sliding velocities. Samples, processed through MAF, possesses higher microhardness, as shown in figure.4.13 and causes lower wear rate, as explained by Archard Equation (Archard et al. 1953). Since MAF process gives better microhardness, because of grain refinement in the material, wear rate of MAF processed samples is reduced.

Table 4 Wear rate at different velocities and different loads

Material/Condition	10 N-1 m/s	10 N-2 m/s	20 N-1 m/s	20 N-2 m/s
As-received	0.0033	0.0043	0.00471	0.00603
1 cycle	0.00244	0.00377	0.00387	0.00452
2 cycle	0.00207	0.00339	0.00357	0.00377
3 cycle	0.00154	0.00209	0.0031	0.00331

(iv) Wear surface study

Figure 4.14 and Figure 4.15 show wear surfaces of as-received and MAF processed samples, at load of 10 N, with sliding velocity 1 m/s and sliding distance 3000 m. Similarly, Figure 4.16 and Figure 4.17 show wear surfaces of as-received and MAF processed samples, for 20 N load with sliding velocity 2 m/s. Delamination, grooves, cracks and wear debris were observed on wear surfaces. Small grooves formed by ploughing, parallel to sliding direction which exhibits plastic deformation. From Figure 4.14 to Figure 4.16, it is observed that, as MAF cycles increase, smooth wear surfaces can be observed, which may be because of enhanced microhardness distribution, which hinders fatigue crack. Further, during cyclic sliding process, wear debris and delamination are reduced (Xu et al. 2013). Variation of load has not shown much change on the surface morphology. But, with variation of sliding distance, wear surface is not smooth in case of samples subjected to sliding distance 3000 m (Figure 4.14 and 4.15). From Figure 4.14 to 4.17, it is clear that the wear surface consists of plastic deformation zones, delamination, debris and micro-ploughing, down the sliding path. Hence, wear mechanism may be identified as abrasive wear (Xu et al. 2013). With the above discussion, it can be seen that MAF processed samples possesses superior wear resistance properties.
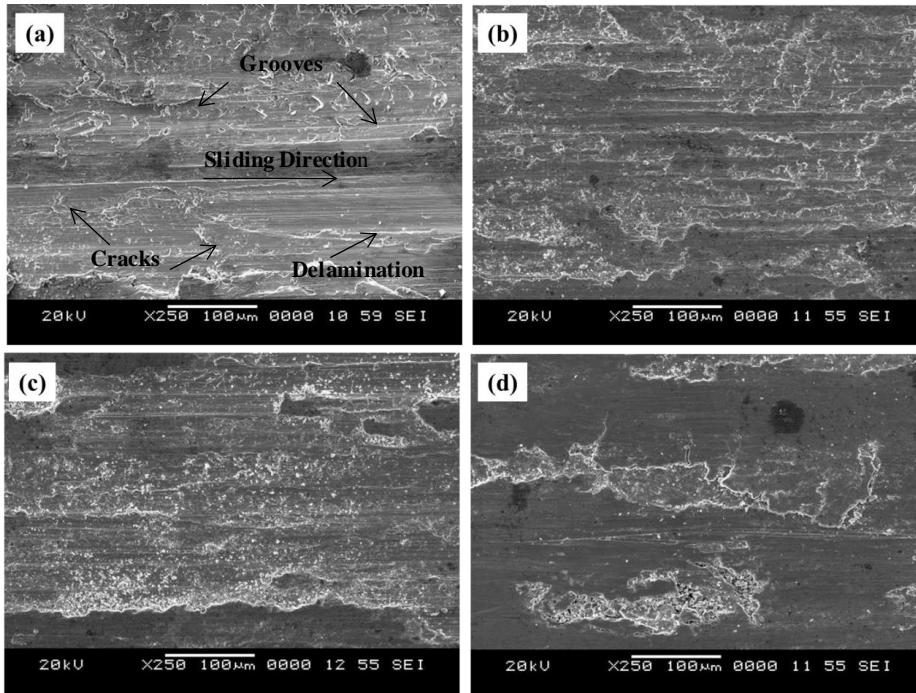
Figure 4.14 SEM images of worn surfaces of (a) As-received and MAF processed (b) 1 cycle, (c) 2 cycle, and (d) 3 cycle samples under 10 N load, 1 m/s with sliding distance 3000 m
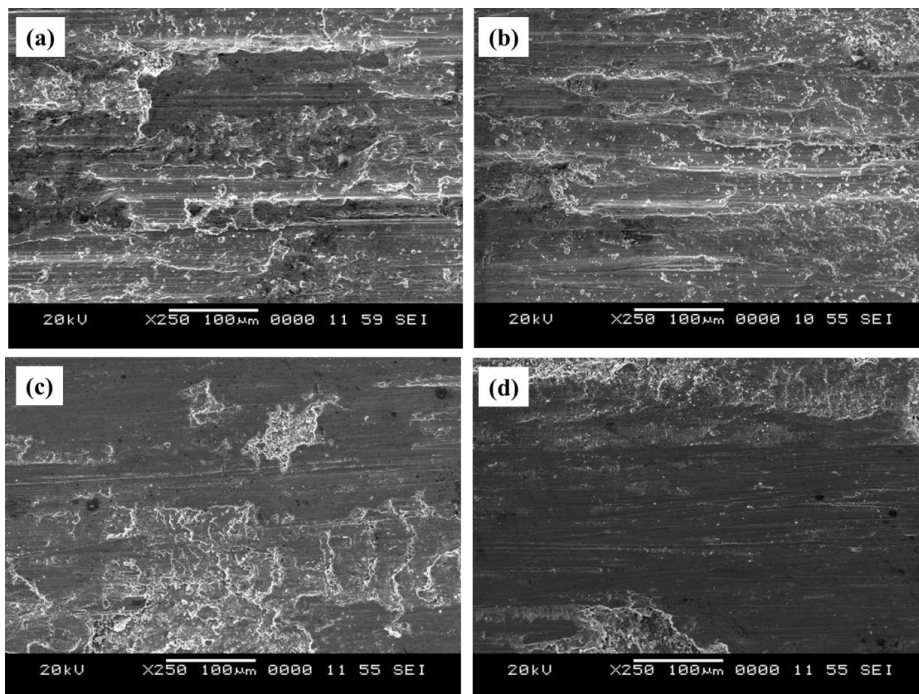
Figure 4.15 SEM images of worn surfaces of (a) As-received and MAF processed (b) 1 cycle, (c) 2 cycle, and (d) 3 cycle samples under 20 N load, 1 m/s with sliding distance 3000 m
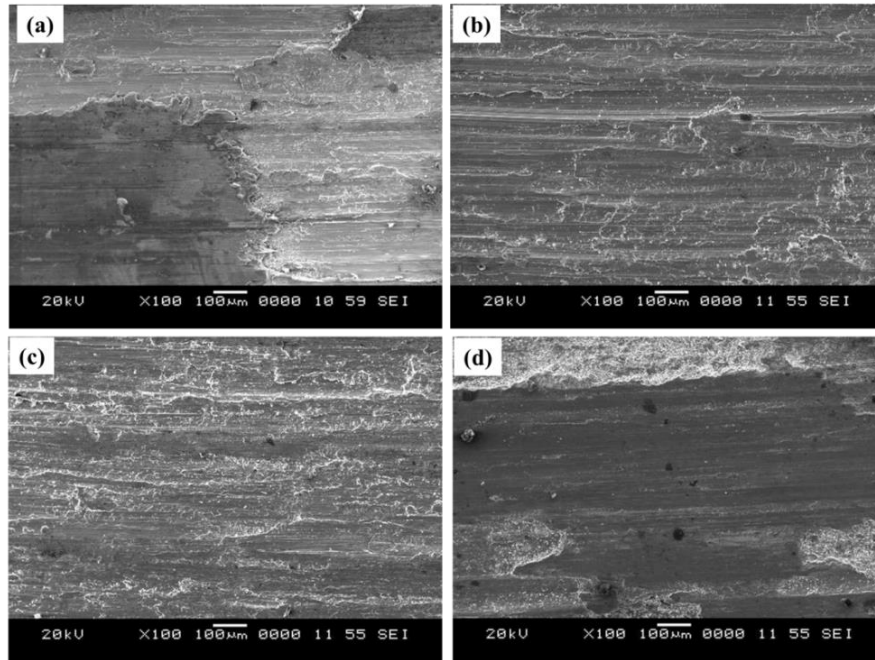
Figure 4.16 SEM images of worn surfaces of (a) As-received and MAF processed (b) 1 cycle, (c) 2 cycle, and (d) 3 cycle samples under 10 N load, 2 m/s with sliding distance 3000 m
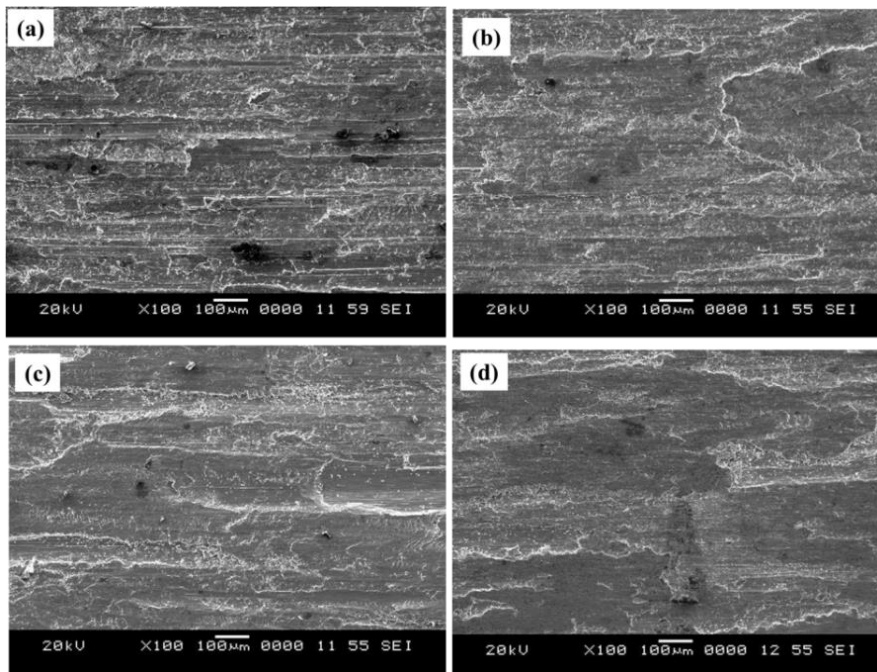
Figure 4.17 SEM images of worn surfaces of (a) As-received and MAF processed (b) 1 cycle, (c) 2 cycle, and (d) 3 cycle samples under 20 N load, 2 m/s with sliding distance 3000 m
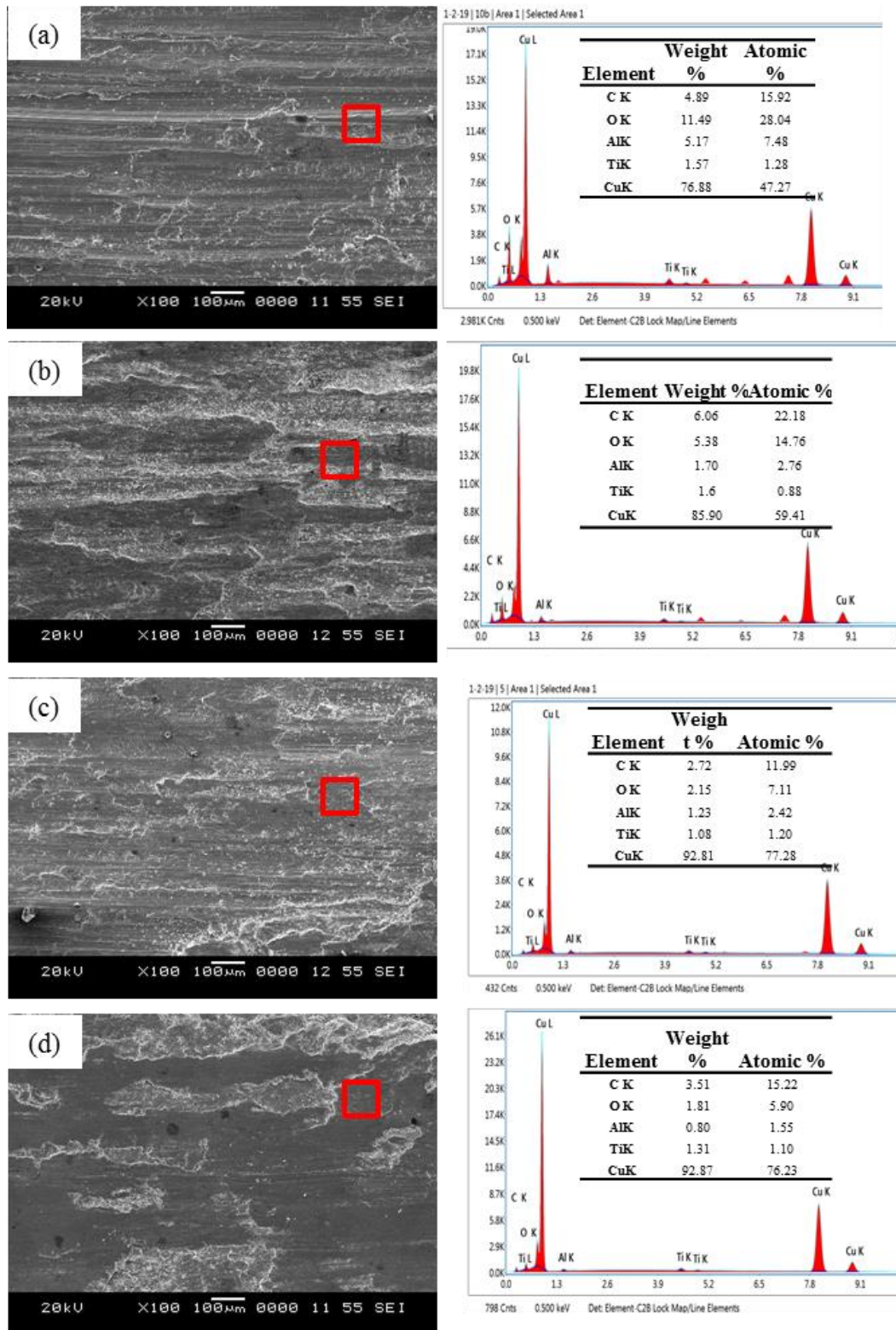
Figure 4.18 EDS analysis for (a) As-received (b) 1 cycle (c) 2 cycle and (d) 3 cycle MAF processed under 20 N load.

Worn surfaces are analyzed by EDS and the results are as shown in Figure 4.18. From EDS analysis, it was observed that the surface contained traces of copper, titanium and oxygen were visible in the areas of delamination, debris and ploughing. Copper alloys possess high tendency towards oxidation, so it plays major role in wear behavior. Similar chemical composition was observed on wear surfaces of both as-received and MAF samples. So, the wear mechanism from the above discussions can be identified as both abrasive and oxidation wear.

4.5 Corrosion behaviour

Electrochemical measurements were carried out using EC-biologic SP-150 workstation for as-received and MAF processed samples using 3.5 Wt% NaCl solution.

(i) Potentiodynamic polarization study

Potentiodynamic polarization tests were performed to investigate the corrosion behavior of copper alloy and it gives various electrochemical information like corrosion potential (E_{corr}), corrosion current density (I_{corr}) and corrosion rate (mm/y). Tofel extrapolation method gives E_{corr} and I_{corr} values from the anodic part of polarization curves (Figure 4.19). Electrochemical kinetics parameters extracted from polarization plots such as E_{corr}, I_{corr} and corrosion rate (mm/y) for as received and MAF processed samples are shown in table 5. From the figure 4.19, it can be observed that, as the number of MAF cycles increases, E_{corr} value shifted to nobler direction and causes decrease in I_{corr} value. Lower I_{corr} values indicate high corrosion resistance. It can be observed that corrosion rate decreases with increase in MAF cycles, indicating improvement in corrosion resistance and current density with decrease in I_{corr} value. Main reason for enhancement in corrosion resistance of grain-refined materials is attributed to improvement in passive film formation and adhesion due to increased grain boundary density (Ralston et al.2010). Decrease in corrosion rate is due to increased cathodic kinetics attributed, to break-up and redistribution of the intermetallics. Homogeneous solute distribution could have an effect on the protection of surface film and presence of Ti is beneficial in reducing the anodic reaction kinetics (Orlov et al.2011).
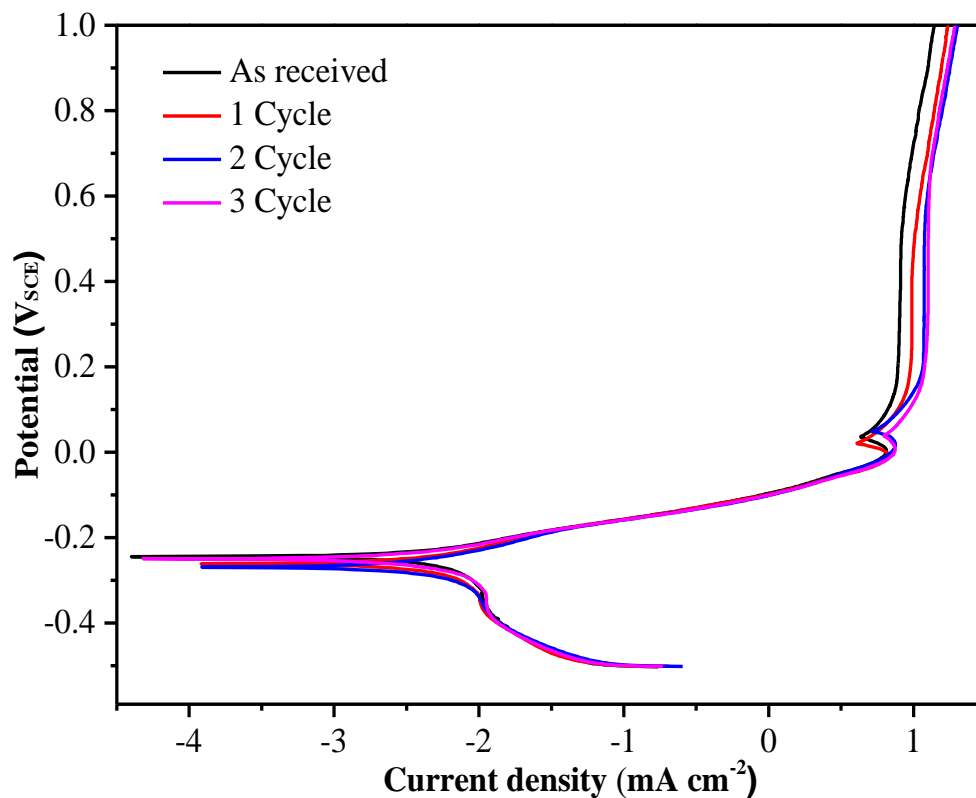
Figure 4.19 Electrochemical potentiodynamic polarization plots of as-received and MAF processed samples

Table 5 Electrochemical kinetic parameters like corrosion potential, corrosion current and corrosion rate (mm/y).

Materials Cu-1.5%Ti	E_{corr} (V_{SCE})	I_{corr} ($\mu A/cm^2$)	Corrosion rate (mm/y)
As-received	-326.8	4.200	0.093
1 Cycle	-181.68	2.407	0.052
2 Cycle	-180.6	2.148	0.036
3 Cycle	-125.7	1.083	0.024

From the above discussion, it can be concluded that increase in corrosion resistance may be because of equiaxed ultrafine grained structure and β phases. Corrosion activation of the MAF 3 cycles sample may be due to the presence of larger crystalline defects like energetic grain boundaries and dislocations.

(ii) Electrochemical impedance spectroscopy (EIS)

EIS is used for investigating electrochemical interface between electrodes and electrolytes and provides impedance and capacitance loop which is evidence for the mechanism of corrosion process. Figure 4.20 (a) shows the Nyquist plots for as-received, 1 cycle, 2 cycle and 3 cycle MAF processed Cu-1.5%Ti alloy. There are two semicircles, bigger one is the capacitance arc and smaller is the inductive loop, which indicates the formation and degradation of protective films on the surface, respectively. Diameter of capacitive arcs represents the corrosion rate of the sample. As the arc diameter increases, better will be corrosion rate. 3 cycle MAF processed alloy sample exhibits slightly larger diameter of capacitive arcs than that of the As-received alloy which implies increased corrosion resistance. Figure 4.20 (b) shows the Radles Circuit which exhibits equivalent circuit to interpret the Nyquist plots of As-received and MAF processed alloys.
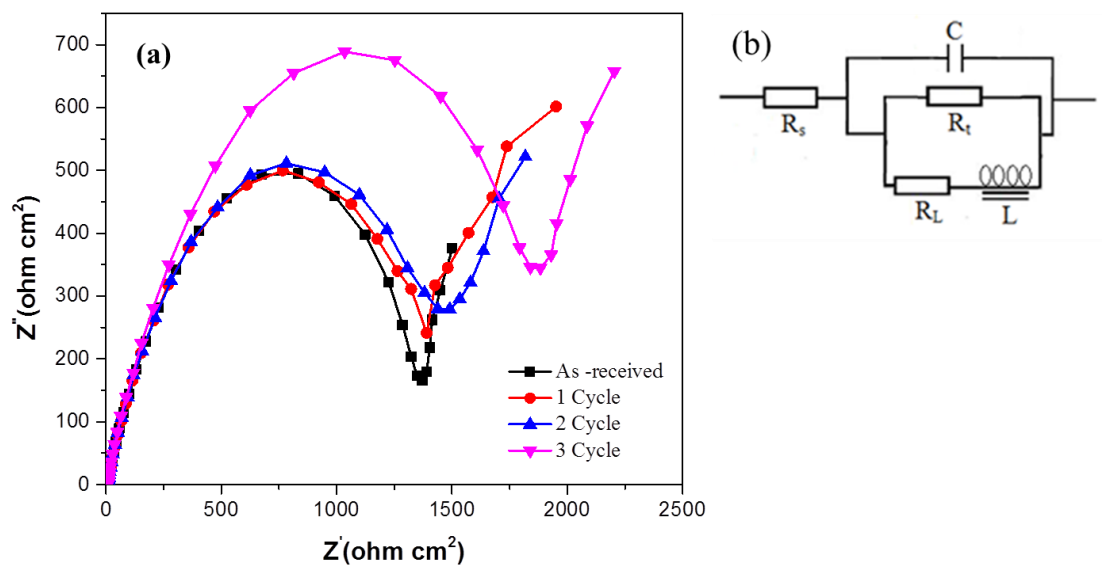
Figure 4.20 Nyquist plots of (a) as-received and MAF processed samples (b) Radles circuit.

A pair of parallel circuits consisting of electrolyte resistance (R_s), capacitance (C), and charge transfer resistance (R_t) is used to describe the electrode reaction process. Nyquist plots for as-received and MAF processed Cu-1.5%Ti alloys shows depressed semicircles. If the metals exhibit better corrosion resistance properties, it is difficult to transfer charges between sample surface and solution, R_t would be higher, which

indicates that 3 cycle MAF alloy has higher corrosion resistance. Corrosion tendency of the As-received and 3 cycle MAF alloy displays good correlation with the polarization study and EIS.
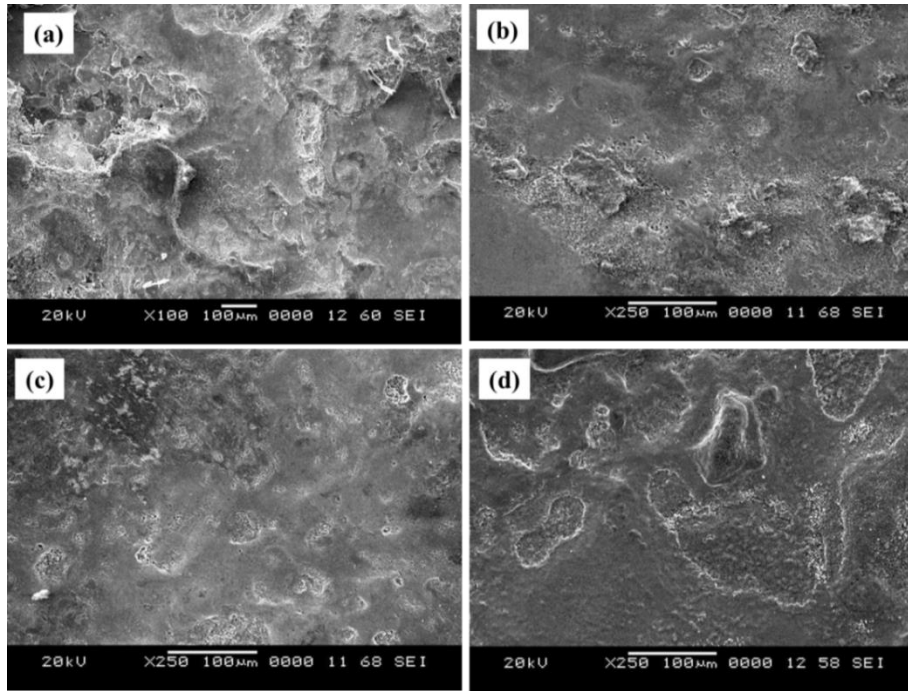
Figure 4.21 SEM images of corrosion samples for different MAF samples

SEM images of Cu-1.5%Ti sample after removing corrosion product on the surface is shown in figure 4.21. Intergranullar and pitting corrosion were observed, because of susceptibility of copper to intergranular corrosion in chlorine solution. Pitting corrosion occurred, because of micro-galvanic coupling between Cu and Ti. A significant dissolution, more corrosion products, cracks and pits were seen in as-received sample (Figure 21 (a)). 3 cycle MAF processed samples were covered with only few pits, indicating better corrosion resistance (figure 4.21 (b)).

Figure 4.22 shows EDS mapping on the corroded surface. As-received sample produced oxide layer of 25.17 wt%. With increase in number of MAF cycles, oxide formation on sample surface reduced, because of increased grain boundaries which acts as corrosion barrier and increased the corrosion resistance.

Figure 4.23 shows the XRD pattern of corroded surface of the as-received and 3 cycle MAF processed at cryogenic conditioned sample is immersed in 3.5% NaCl solution. Some of the corroded product was identified Cu_2O and CuCl.
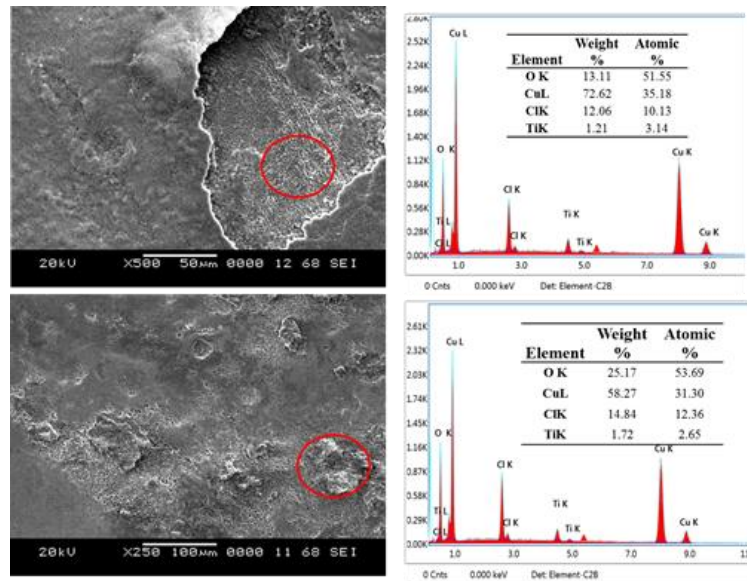
Figure 4.22 SEM images with EDS and elemental mapping of (a) as-received and (b) 3 cycle samples
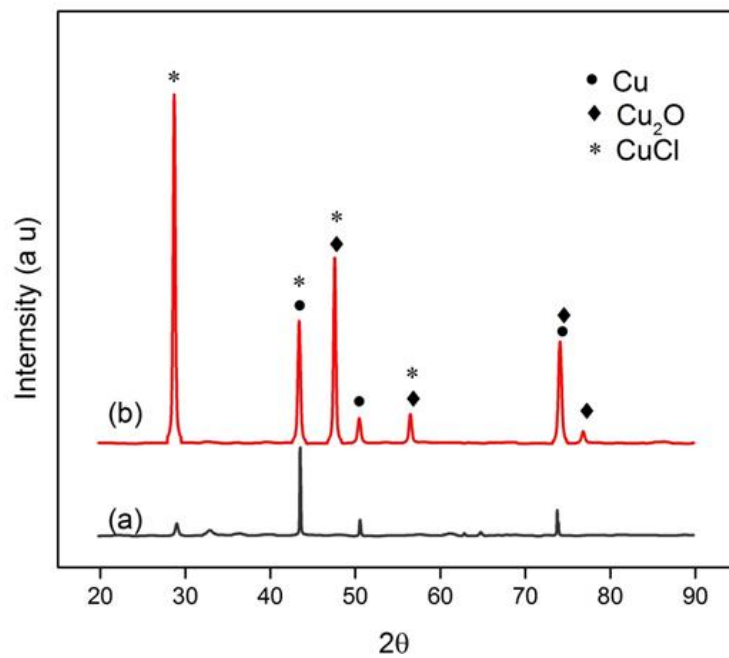
Figure 4.23 XRD pattren of Corroded surface (a) as-received and (b) 3 cycle sample

4.6 Summary

MAF has been successfully carried out on Cu-1.5Ti alloy at cryogenic temperature to study microstructural changes, mechanical, wear and corrosion properties. The obtained results are summarized as below:

- Cu-1.5Ti alloy was processed by MAF at cryogenic temperature. Grain size reduced to 2 µm after 3 cycles of MAF. Density of shear bands increased and width of the shear bands decreased as the number of MAF passes increased.

- Tensile tests showed an increment of 3.1 times in UTS for 3 cycle MAF processed sample. YS also increased up to 3 cycle, which was 6.9 times higher than that of as-received sample. Ductility for 3 cycle sample was 26 %, while it was 2.1 times less than as-received sample. YS and UTS increased drastically with increase in MAF passes which are due to grain boundary strengthening mechanism. Percentage elongation decreased initially, but it increased during the 2 and 3 cycles.

- Maximum hardness value reached to 211 HV after 3 cycles of MAF. As the number of forging cycle increases, hardness increases due to increase in dislocation density and increasesing starin hardening effect.

- Tensile fractured surface showed that the dimple size decreased for 1 cycle of MAF. But after 2 and 3 cycles of MAF, dimple size increased slightly because of increase in ductility and it's a depending function of ductility.

- High wear resistance was observed in 3 cycle MAF processed samples, due to increases in hardness of Cu-1.5%Ti alloy as compared to As-received alloy. COF decreased with increase in MAF cycles, but increased as the load and sliding distance increased.

- SEM micrograph of worn surface showed the surface plastic deformation, Scratches, delamination, and ploughing were less in MAF processed sample, and exhibited abrasive wear mechanism and formation of the oxides controlled the wear behaviour. EDS analysis showed presence of oxygen peaks along with copper peak on the wear surface. its shows the abrasion and oxidation wear mechanism.

- EIS plots and Potentiodynamic polarization showed the corrosion behaviour of as-received and MAF processed samples. MAF processed samples showed better corrosion resistance properties due to refined microstructure.

CHAPTER 5

5. RESULTS AND DISCUSSION OF Cu-3%Ti PROCESSED BY MAF

Cu-3%Ti alloy samples were processed by MAF upto 3 cycles at cryogenic temperature. Microstructures of the processed samples were characterized using OM, SEM and TEM. Microstructures are analyzed by EBSD for grain structure and grain boundaries misorientation angles. XRD was conducted to identify different phases in samples. Tensile and microhardness tests was carried out for MAF processed samples. MAF processed samples were subjected to wear tests at different conditions. Further, MAF processed samples tested for corrosion and the results are discussed.

5.1 Microstructure analysis

(i) Optical and SEM analysis

Figure 5.1 (a)–(d) show optical micrographs of as-received and MAF processed samples. It is observed that the as-received Cu-3%Ti alloy has equiaxed grains with traces of twins (Figure 5.1 (a)) with average grain size of ~ 80 μm. Optical micrographs of MAF processed samples (Figure 5.1 (b)-(d)) clearly show the formation of ultrafine grains during MAF processing at cryogenic temperature. Figure 5.1 (b) shows that deformation/shear bands formed within the grains after MAF 1-cycle. At lower strain of 0.546 (after 1 cycle), shear bands were focused along one direction inside the grain and randomly oriented in other grains. As the number of cycles (for 2 and 3 cycle samples) increases, due to higher strain, shear bands intersect with each other resulting in the formation of intersecting slip bands, because of deformation along the different directions during MAF process (Padap et al. 2009). Density of shear bands increase due to increase in MAF passes and it was observed that grain boundaries became ambiguous, as shown in Figure 5.1 (d). High dislocation density and deformation bands, with reduced gaps, were observed in MAF 3 cycle sample as shown in Figure 5.1 (d), where subgrains are formed inside the grain. Formation of new grain or subgrain were observed in SEM images (Figure 5.2), which are difficult to witness in OM images due to existence of high dislocation density and greater crossing of shear bands.
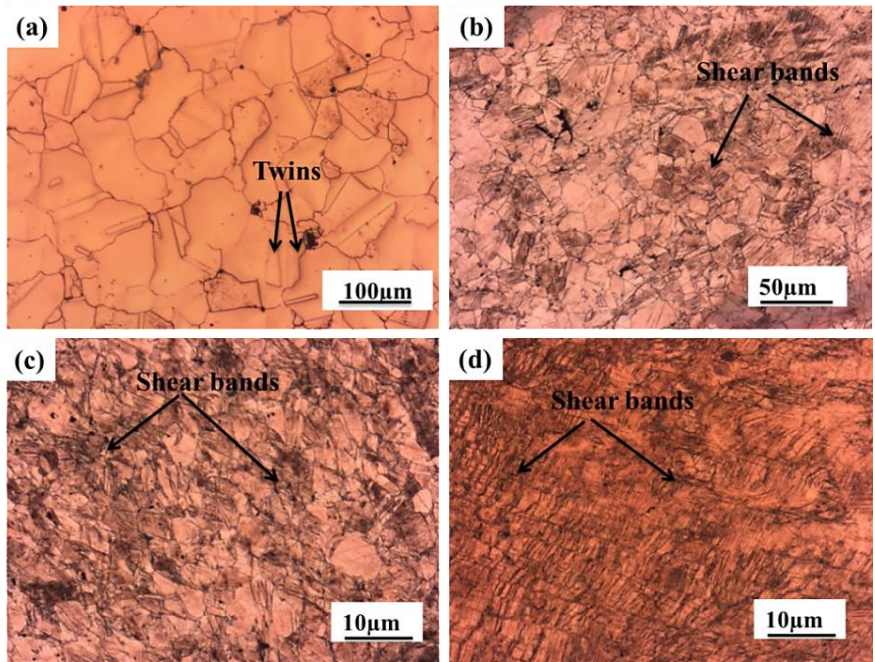
Figure 5.1 Optical Microstructures of (a) as received (b) 1 cycle (c) 2 cycle and (d) 3 cycle MAF processed samples
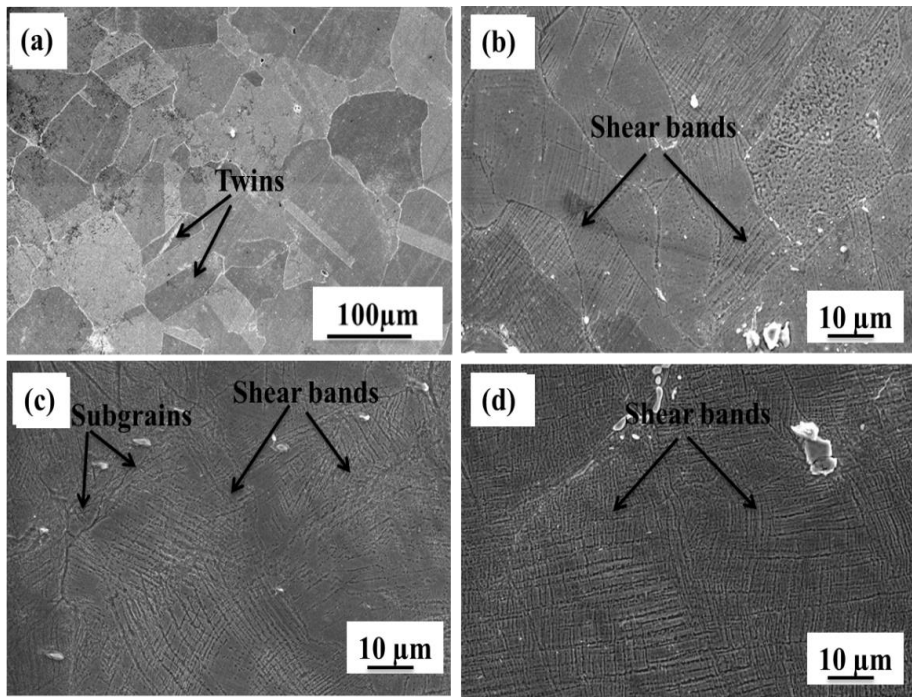
Figure 5.2 SEM micrographs of (a) as received (b) 1 cycle (c) 2 cycle and (d) 3 cycle MAF processed samples

(ii) TEM analysis

In order to further appreciate tiny features, TEM images were taken for samples of higher cycle. Figure 5.3 shows TEM images with corresponding selected area electron diffraction (SAED) patterns of samples processed MAF for 2 and 3 cycles. These images clearly showed the formation of shear bands with deformation twins that were gradually established due to increase in MAF cycles under cryogenic temperature. MAF 2 cycle sample exhibits dislocation substructures / twins inside the coarse grains. Presence of LAGBs is explained from SAED pattern, as presented in the inset of figure 5.3 (b). SAED pattern showed intermittent spotty rings with stretched and broadened regions, because of diffraction due to presence of coarser and elongated grains. While the narrow regions in the form of rings are because of the presence of fine deformed grains (Dasharath et al. 2016) .
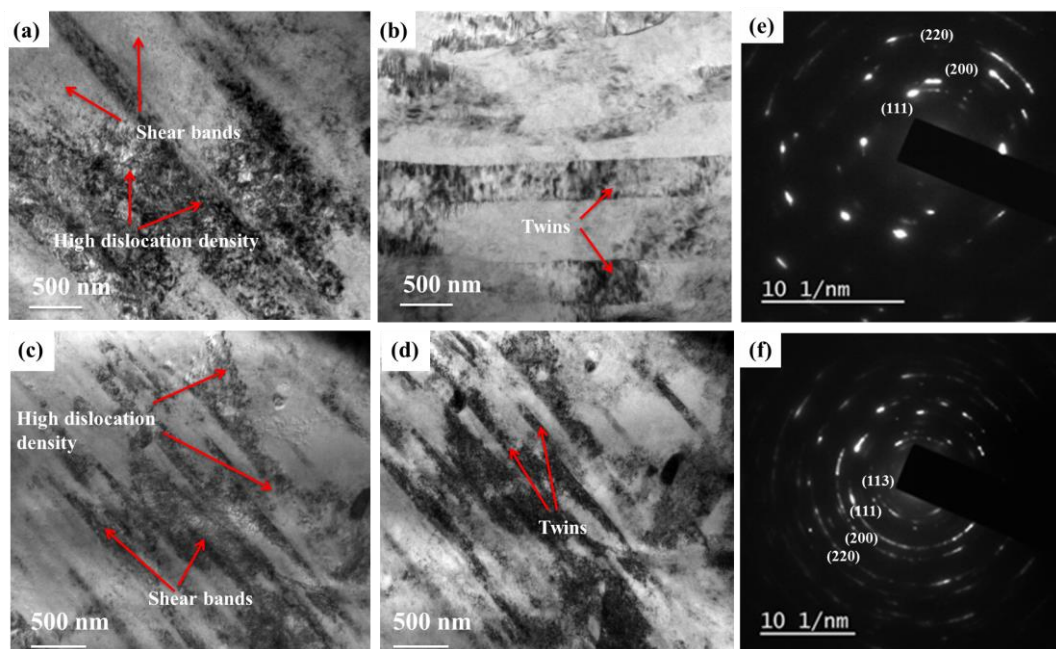
Figure 5.3 TEM images of (a) 2 cycle and (b) 3 cycle samples

Figure 5.3 (c) shows the TEM images of 3 cycle MAF processed samples, which shows highly deformed grains consisting of high-density dislocation substructures and shear bands of high density and reduced. SAED pattern in figure 5.3 (d) display endless, but stretched rings, suggesting the formation of ultrafine substructures with LAGBs.

Ultrafine twins are generated inside the substructures due to low stacking fault energy. Because of increase in deformation strain from 1.09 to 1.64 (from 2 to 3 cycles), lamellar grain structures with HAGBs are steadily transformed to ultrafine dislocation substructures along with fine twins which twins provide twin boundary strengthening and improves ductility (Gupta et al. 2016, Rao et al. 2014).
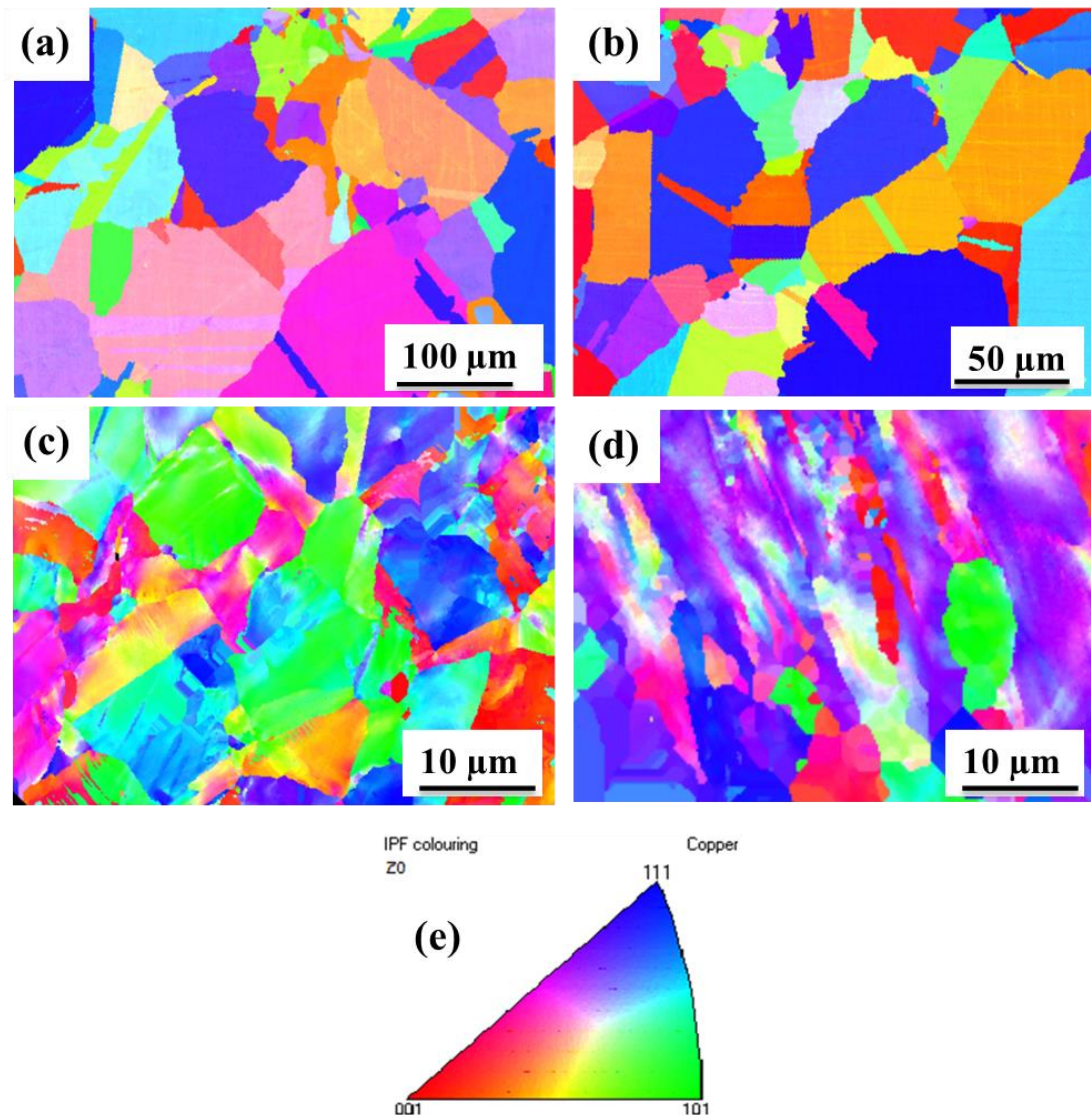
Figure 5.4 IPF map of (a) as-received, (b) MAF 1 cycle, (c) MAF 2 cycle, and (d) MAF 3 cycle samples

Figure 5.4 shows OIM analyzed inverse pole figure (IPF) map of as-received and MAF processed samples. Color in IPF map (Figure 5.4 (e)) represents different crystal orientation. As-received sample shows heterogeneous structure Figure 5.4 (a)) and

grain size decreases with increase in number of cycles, as shown in Figure 5.4 (b)-(d), respectively. 3 cycle sample consists of fine (sub) grains with LAGBs. As the number of MAF cycle increases, subgrain boundaries gradually transform from HAGBs to LAGBs, because of increase in cumulative strain (Nieh et al. 1991, Dao et al. 2006). Further, in 3 cycle samples (Figure 5.4 (d)), grains are elongated. Figure 5.5 shows the distribution of grain boundaries, misorientation angles of as-received and MAF processed samples. As-received sample shows strong peaks with high misorientation angles (~60°). Whereas samples processed by MAF for 3 cycles showed reduction in misorientation angle (<10º) of the grain boundaries. Grain refinement rate decreases for higher cycles of MAF.
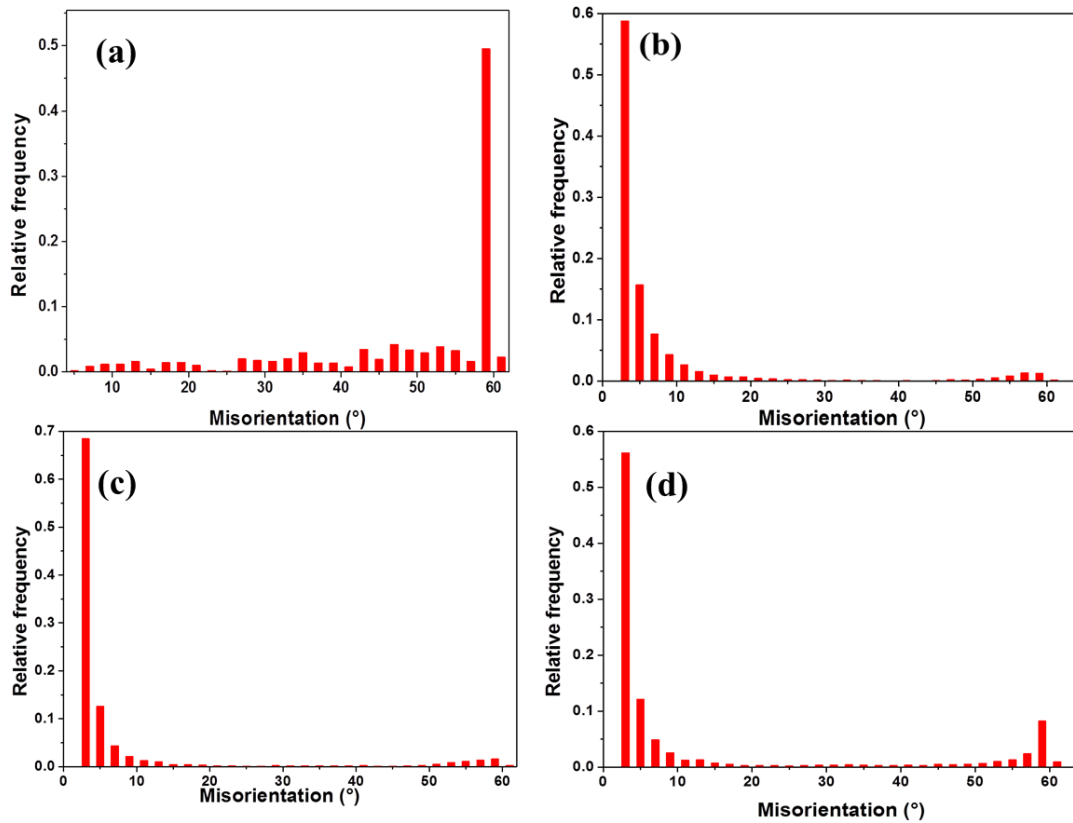
Figure 5.5 Misorientation angle of (a) as received (b) 1 cycle (c) 2 cycle and (b) 3 cycle MAF sample

Initial texture ranged from (001) to (111) with larger grains having either (001) or (111) orientation and it is can be clearly seen as blue and red grains in the IPF map (Figure 5.4(a)). Texture to (101) after 1 cycle indicated by green color in the IPF map Figure 5.4 (c-d). After 3 cycles, elongated grains are formed with severe grains refinement.

Coarse grains were broken into ultrafine grains with increased number of MAF cycles and at MAF 3 cycle, majority of grain structure is covered with ultrafine grains (Sahu et al. 2017).

5.2 X-ray diffraction analysis

Figure 5.6 shows XRD plot of as-received and MAF processed samples. Intensity of planes (111) and (311), observed in as-received sample, show strong peaks initially, but after 3 cycles of MAF, intensity of planes (111) and (311) decreases. Planes (200) and (220) show sudden increase in intensity along with peak broadening, because of strain hardening of sample, after MAF 3 cycles. Peak shifting occurred at 1° after MAF 3 cycles, because of high dislocation density in the material. After MAF 3 cycles, variation in the peaks is observed due to change in texture because of shear deformation.
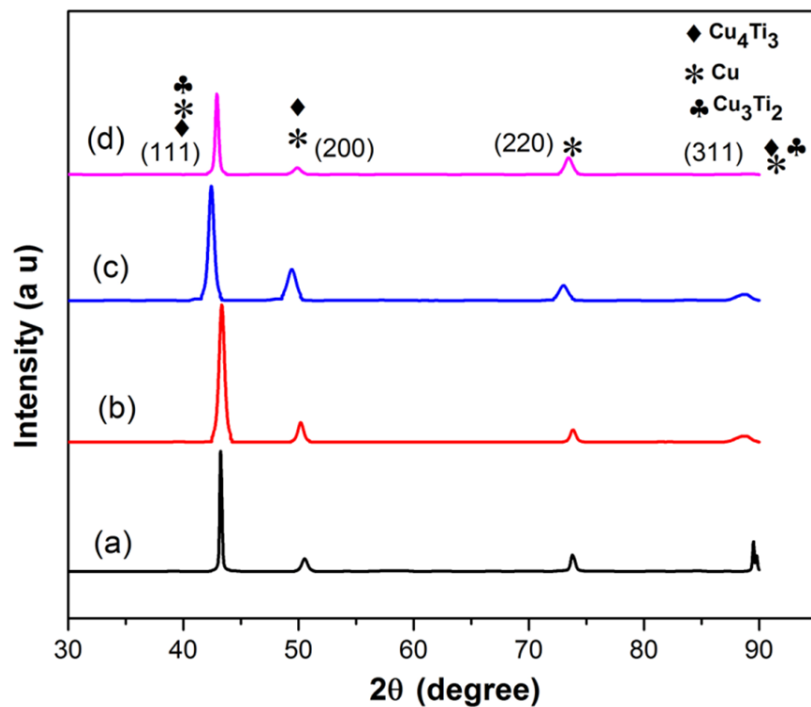
Figure 5.6 XRD analysis of (a) as received (b) 1 cycle (c) 2 cycle and (d) 3 cycle MAF samples

5.3 Mechanical properties

(i) Tensile behaviour

Stress-strain curve of as-received and MAF processed samples of Cu-3%Ti alloy are shown in Figure 5.7 (a).
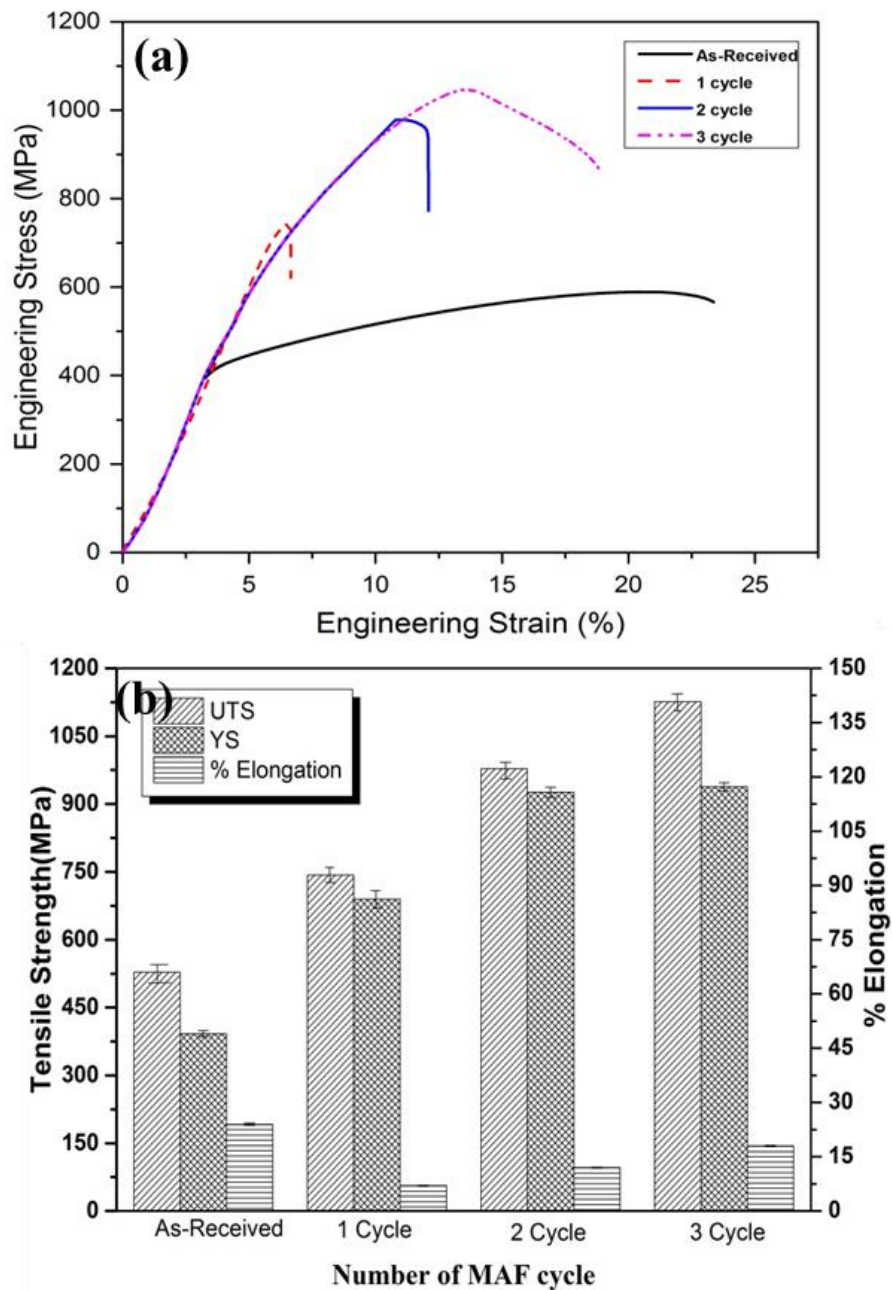
Figure 5.7 (a) Stress-strain curve, (b) UTS, YS and % elongation variation plots

UTS, YS and % elongation are plotted and are shown Figure 5.7 (b). Summary of mechanical properties for all the samples are shown in table 6. For each condition, 3 samples were tested for confirming the tensile properties. YS and UTS obtained for as-received alloy are 392 MPa and 528 MPa, respectively, with 24% elongation. After 1 cycle of MAF with cumulative strain, ε=0.54, YS and UTS increased to 717 MPa and 743 MPa, respectively. YS and UTS increased further with increase in MAF cycles and reached to maximum of 978 MPa and 1126 MPa, respectively for MAF 3-cycle sample. Increase in strength is due to two reasons. First, due to grain boundary strengthening mechanism according to which strength increases with decrease in grain size as per Hall-Petch equation (Dieter. 1988). Second, due to increase in dislocation density with increase in number of forging passes. After 1 cycle, elongation decreased to 7%. However, with further cycles, it kept on increasing and reached to 12% for 2 cycle and 18% for 3 cycle sample. Both, ductility and strength increased during 2nd and 3rd cycles of MAF, due to decrease in shear band width and twin width/spacing. After 1 cycle, the increase in strength and ductility was due to decrease in twin spacing during MAF process.

Table 6 Mechanical properties and grain size for all samples processed by MAF cryo-forging

Sample no.	UTS (MPa)	YS (MPa)	Elongation (%)	Hardness (Hv)	Avg. grain size (μm)
As-received	528±8	392±7	24±0.30	224±12	80±10
1 cycle	743±6.5	717±5	7±0.13	340±8	7±2.5
2 cycle	978±9.5	926±11	12±0.17	388±12	0.9±.02
3 cycle	1126±15	938±9	18±0.20	402±10	0.25±.015

(ii) Vickers Microhardness

Microhardness (HV) tests were conducted on as-received and MAF processed samples, using Omni-Tech Vickers Hardness tester with a load of 100 g and dwell time 15 s. Test was conducted on the cross-section of sample to check the consistency of hardness distribution over the surface. Variations in microhardness values for as-received and MAF pass samples are shown in Figure 5.9. As-received sample shows hardness of 224 HV and with increase in MAF passes, hardness increased to 340 HV for 1 cycle, 388

HV for 2 cycles and 402 HV for 3 cycle sample. Increase in hardness is due to strain hardening, high dislocation density and also, due to formation of ultrafine grains (Toroghinejad et al. 2014). Variation in microhardness is related to YS and UTS, as they are mutually interdependent on one another. Relationship between hardness, YS and UTS with average grain size is shown in Figure 5.10.
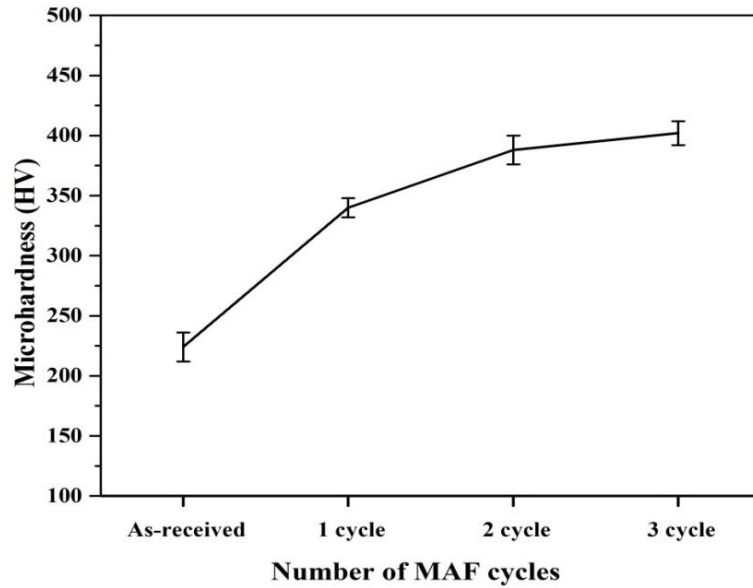
Figure 5.8 Vickers microhardness of as-received and MAF processed samples
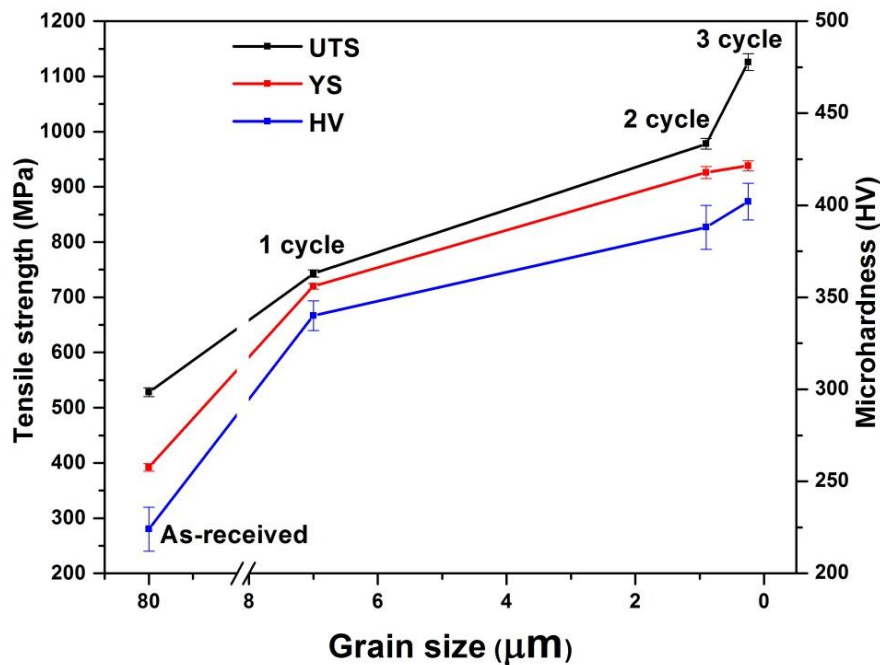
Figure 5.9 Relationship between mechanical properties and Average grain size

(iii) Fractography

Fracture topography of MAF processed Cu-3%Ti alloy after tensile test was evaluated by SEM. Fracture surface of as-received and MAF1, 2, 3 cycle samples are shown in Figure 5.11. As-received specimen shows ductile fracture having large size dimples (30 μm). These large size dimples are due to large grain size in the sample and also, because of coalescence of voids in ductile materials. Coarse dimples were the indication of good ductility. After 1 cycle, dimple size reduced to 3 μm and % elongation decreased to 7%. Dimple size increased to 10 μm and 20 μm after 2 and 3 cycles, respectively and % elongation increased to 12% and 18%, respectively. Variation in dimple size during MAF is due to the development of ultrafine dislocation substructure or subgrains.
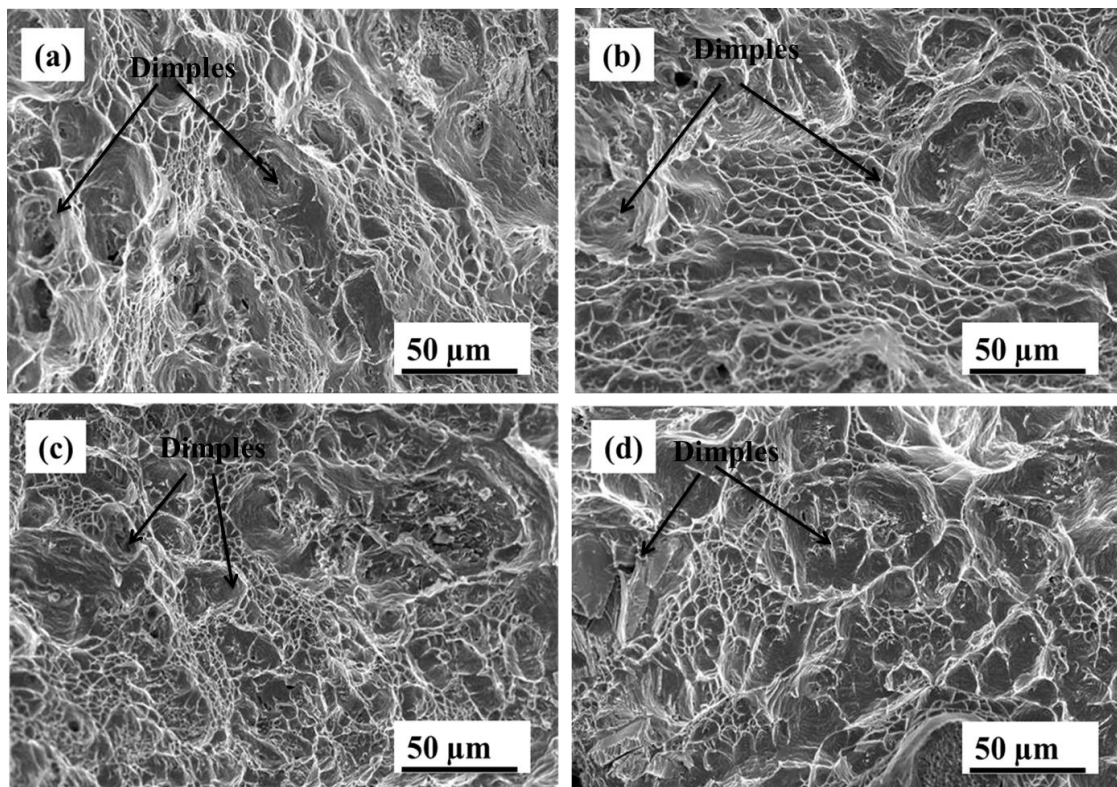
Figure 5.10 Fractured micrographs of (a) as-received and MAF (b) 1 cycle, (c) 2 cycle, and (d) 3 cycle samples

5.4 Wear behaviour

(i) COF during wear test

As-received and MAF processed samples were subjected to wear test at two different loads (10 N and 20 N) with six sliding distance (500 m to 3000 m) at a speed of 1 m/s and 2 m/s and track diameter 114 mm. Figure 5.11 shows the variation of COF with MAF passes for different speeds and loads. More fluctuation in COF is seen in samples subjected to 20 N load, but when samples subjected to 10 N load, fluctuation is reduced.
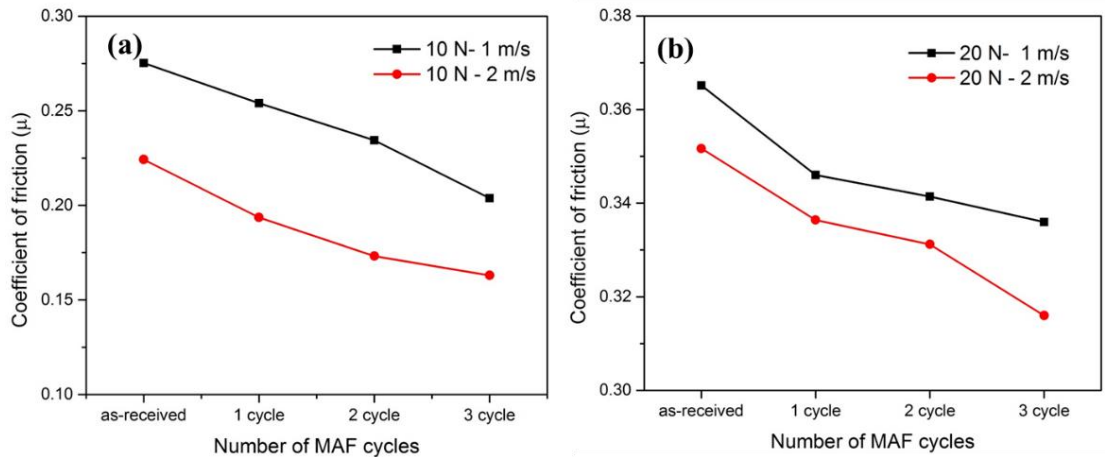
Figure 5.11 COF curves for samples under 10 N and 20 N load with (a) 10N with 1 m/s and 2 m/s (b) 20 N with 1 m/s and 2 m/s at 3000 m.

COF values improved for MAF processed samples at all loading conditions (10 N and 20N). Among MAF processed samples, 3 cycle sample indicated lower COF compared to other samples. COF values for two different speed and load is tabulated in table 7. Fluctuations increase at 20 N load, because of increase in surface contact between sample and steel disc. Hence, MAF process leads to the decrement of COF values due to their hardness properties and exhibited wear resistance properties (Li et al. 2010).

Table 7 COF value for different load and different velocities

Material/Condition	10 N-1 m/s	10 N-2 m/s	20 N-1 m/s	20 N-2 m/s
As-received	0.27	0.22	0.36	0.35
1 cycle	0.25	0.19	0.34	0.33
2 cycle	0.23	0.17	0.34	0.33
3 cycle	0.20	0.16	0.33	0.31

(ii) Volume mass loss (mm^3)

Figure 5.12 shows the variation of wear volume loss with different sliding distance for as-received and MAF processed samples. Figure 5.12 (a) and (b) show the results when tested at 1 m/s with 10 N and 20 N.
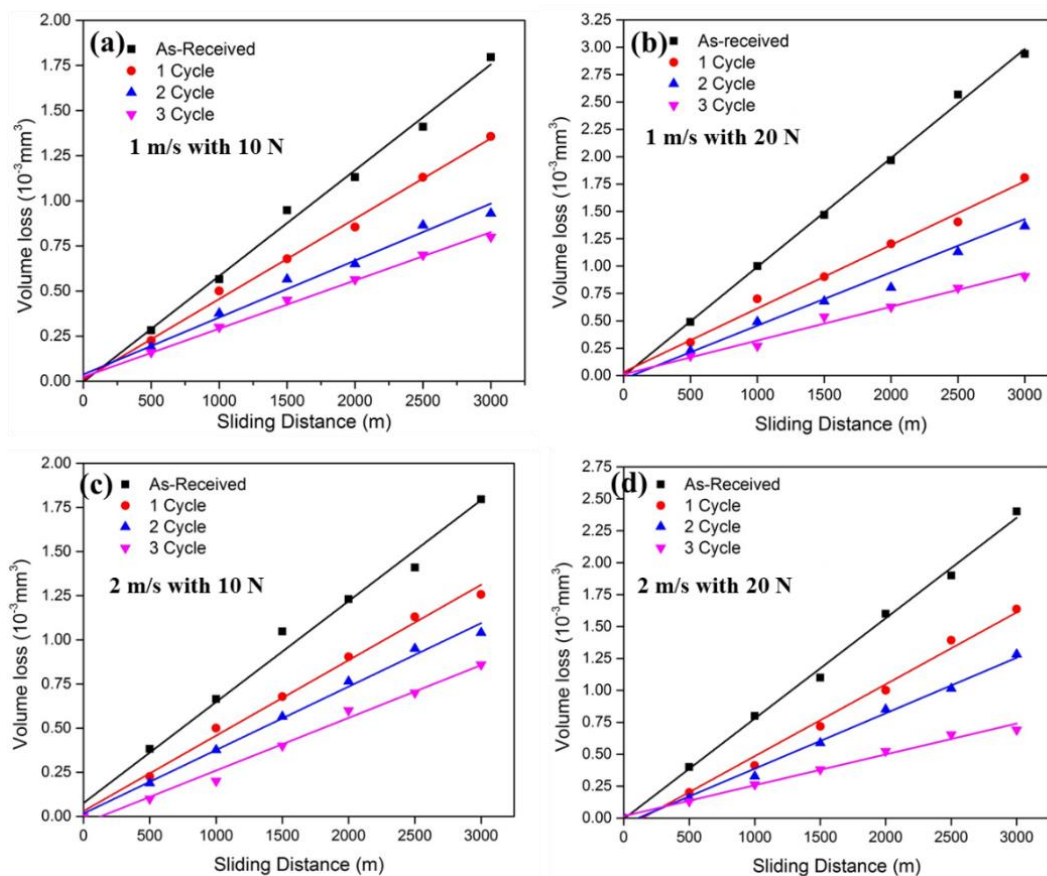
Figure 5.12 Volume mass loss (mm^3) v/s Different sliding distances (a) 1 m/s with 10 N (b) 1 m/s with 20 N (c) 2 m/s with 10 N (d) 2 m/s with 20 N.

Variation in volume mass loss is a derivative of sliding distance. Relationship between volume loss v/s different sliding distances as shown in Figure 5.13. The volume loss for 1 m/s and load of 10 N conditions was depicted in Fig.5.13 (a). As-received samples have more volume loss as compared to forged samples due to low hardness and volume loss is linearly varying with sliding distance. Figure 5.13 (b) shows the result obtained at 1 m/s with 20 N loads. Similarly figure 5.13 (c and d) shows the results at 2 m/s with 10 N and 20 N. Cumulative volume loss is higher in higher sliding distance and more volume loss is observed in higher load. As the number of MAF cycles increases, volume mass loss decreases due to improvement of hardness.As received samples exhibited higher volume mass loss. Higher wear resistance was observed in higher MAF cycles, due to increases in hardness and grain refinement. With increases in load, volume mass loss increases these variations and is shown in figure 5.13. Volume mass loss is related to hardness demonstrated Archard Equation.

Similarly, fFigure 5.12 (c) and (d) shows the results at 2 m/s with 10 N and 20 N. It is observed that cumulative volume loss is linearly varied with the sliding distance for as-received and MAF processed samples. Volume loss increases with increase in load and sliding velocity. As the number of MAF cycles increases, volume mass loss decreased due to improvement of hardness (Manjunath et al. 2018).

(iii) Wear Rate and wear morphology

Figure 5.13 shows the variation of wear rate with number of MAF cycles for different loading and sliding conditions. MAF processed samples showed decreased wear rate. With increase in load and sliding distance, wear rate increases for all samples and is shown in   Figure 5.13. Wear rate at different velocities and different loads is tabulated in table 8. As number of MAF cycle increases, wear rate reduces, due to increases in hardness. Worn surfaces showed grooves, micro cracks, delamination, ploughing and wear debris along the sliding direction, which are caused due to initiation and propagation of subsurface cracks, resulting in removal of material in the form of flakes or wear debris and are shown in Figure 5.14 to 5.18.
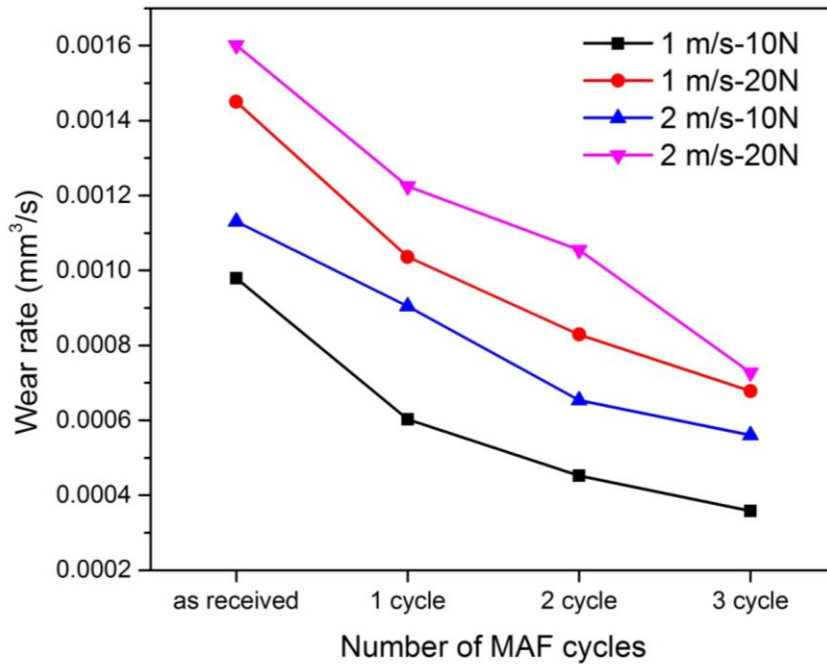
Figure 5.13 Wear rate versus MAF cycles

Table 8 Wear rate at different velocities and different loads

Material/Condition	10 N-1 m/s	10 N-2 m/s	20 N-1 m/s	20 N-2 m/s
As-received	9.796×10^{-4}	11.3×10^{-4}	14.5×10^{-4}	16×10^{-4}
1 cycle	6.0288×10^{-4}	9.0432×10^{-4}	10.4×10^{-4}	12.2×10^{-4}
2 cycle	4.5216×10^{-4}	6.536×10^{-4}	8.289×10^{-4}	10.6×10^{-4}
3 cycle	3.5796×10^{-4}	5.6056×10^{-4}	6.7824×10^{-4}	7.2752×10^{-4}

Wear surfaces appear to be smooth in case of MAF processed samples, due to improved microhardness distribution which helps in avoiding the formation of wear debris. Delamination, wear debris and ploughing areas were analyzed by EDS and are shown in Figure 5.18. Copper, titanium and oxygen peaks were identified and since Copper reacts with oxygen, it might also be the reason for wear behavior. So, oxidation wear is also considered as one of the wear mechanisms.
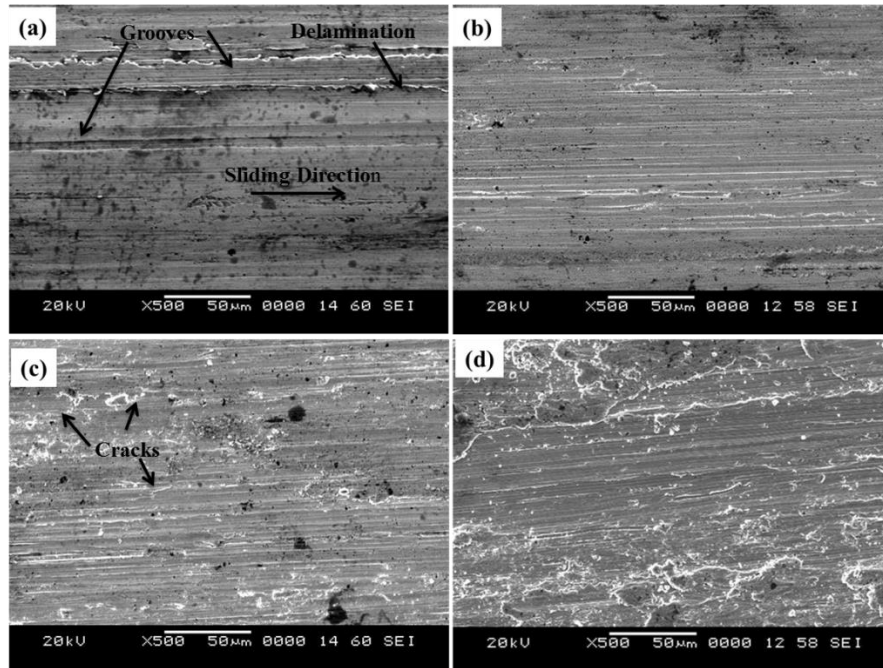
Figure 5.14 SEM images of worn surfaces of (a) As-received and MAF processed (b) 1 cycle, (c) 2 cycle, and (d) 3 cycle samples under 10 N load, 1 m/s with sliding distance 3000 m
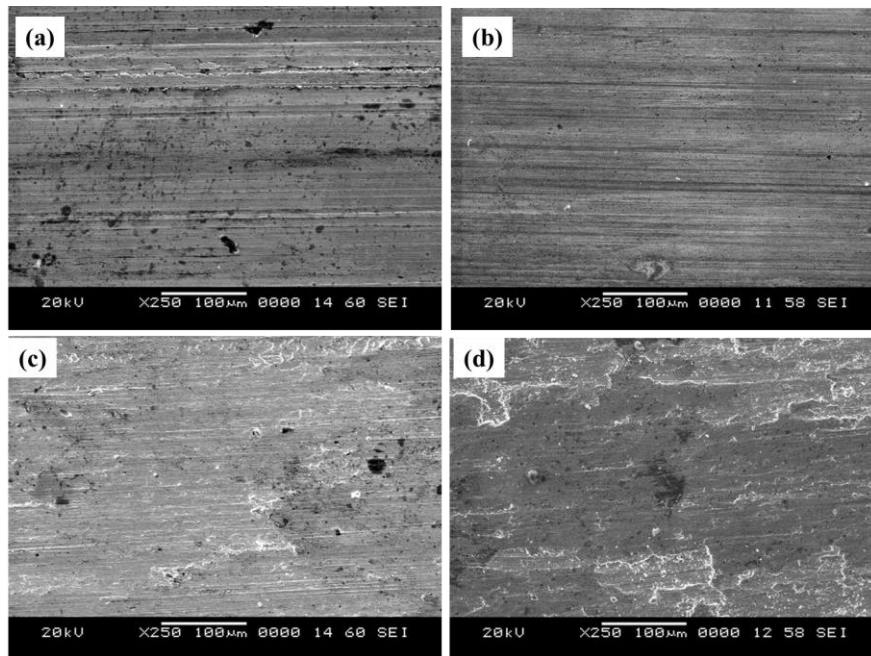
Figure 5.15 SEM images of worn surfaces of (a) As-received and MAF processed (b) 1 cycle, (c) 2 cycle, and (d) 3 cycle samples under 20 N load, 1 m/s with sliding distance 3000 m
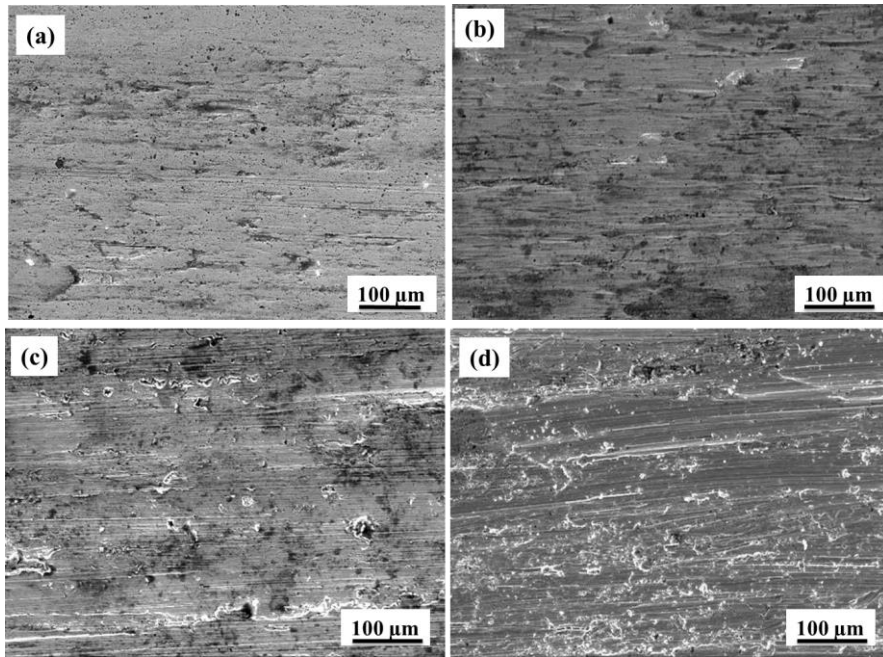
Figure 5.16 SEM images of worn surfaces of (a) As-received and MAF processed (b) 1 cycle, (c) 2 cycle, and (d) 3 cycle samples under 10 N load, 2 m/s with sliding distance 3000 m
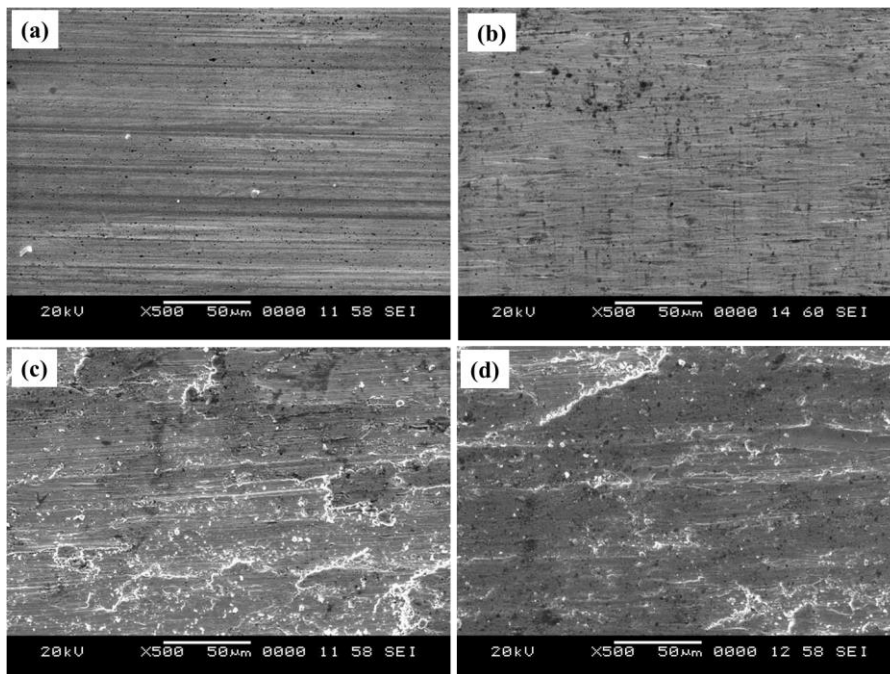
Figure 5.17 SEM images of worn surfaces of (a) As-received and MAF processed (b) 1 cycle, (c) 2 cycle, and (d) 3 cycle samples under 20 N load, 2 m/s with sliding distance 3000 m
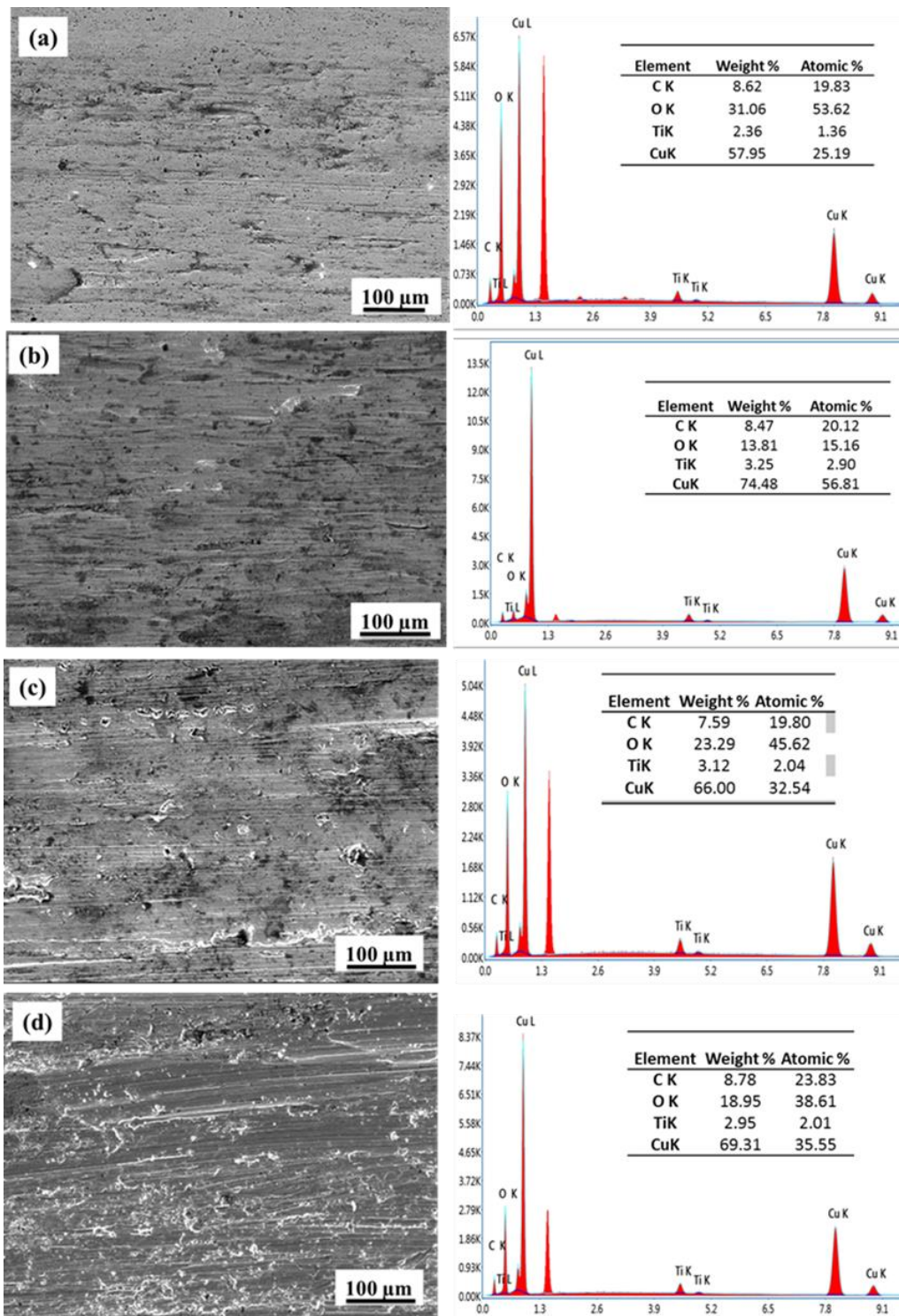
Figure 5.18 EDS analysis of Cu-3%Ti (a) as-received, (b) MAF 1 cycle (c) 2 cycle and (d) 3 cycle

5.5 Corrosion Behavior

Electrochemical measurements were carried out using EC-biologic SP-150 workstation for as-received and MAF processed samples using 3.5 wt%NaCl solution.

(i) Potentiodynamic polarization study

Electrochemical parameters like corrosion potential (E_{corr}), corrosion current density (i_{corr}) and corrosion rate (mm/y) are extracted from Tafel extrapolation method and potentiodynamic polarization curves are represented in Figure 5.19 and values are shown in Table 9. Corrosion rate is dependent on corrosion current density (i_{corr}). Decrease in i_{corr} value decreases the corrosion rate.
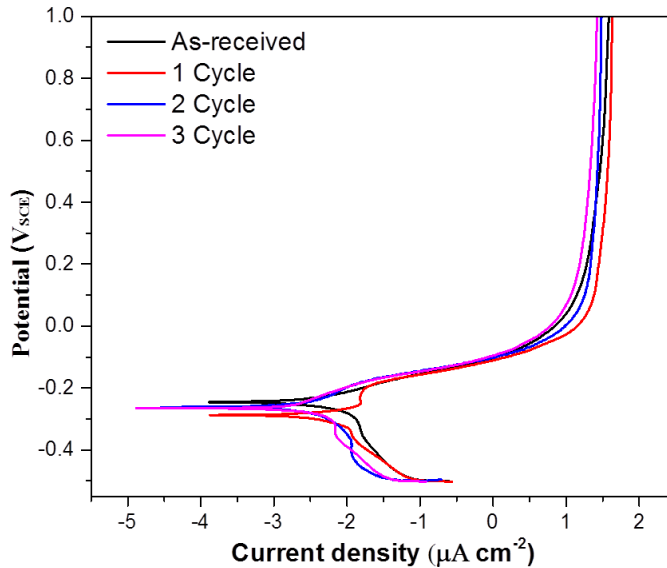
Figure 5.19 Electrochemical potentiodynamic polarization plots of as-received and MAF processed samples.

Corrosion resistance increases with increase in MAF cycles, as MAF processed samples have lower i_{corr} values. Improvement in corrosion resistance is due to ultrafine grained microstructure and uniform distribution of secondary particles which helped in passive film formation ($Cu(OH)_2$) and adhesion due to increased grain boundary density which increases the corrosion resistance.

Table 9 Electrochemical kinetic parameters like corrosion potential, corrosion current density, corrosion rate (mm/y)

Materials Cu-4.5%Ti	E_{corr} (V_{SCE})	I_{corr} ($\mu A/cm^2$)	Corrosion rate (mm/y)
As-received	-233.22	6.590	0.153
1 Cycle	-230.68	3.473	0.081
2 Cycle	-223.662	2.831	0.066
3 Cycle	-232.988	1.827	0.042

(ii) Electrochemical Impedance Spectroscopy (EIS)

EIS test for unprocessed and MAF processed samples were carried out to further study the corrosion behavior.
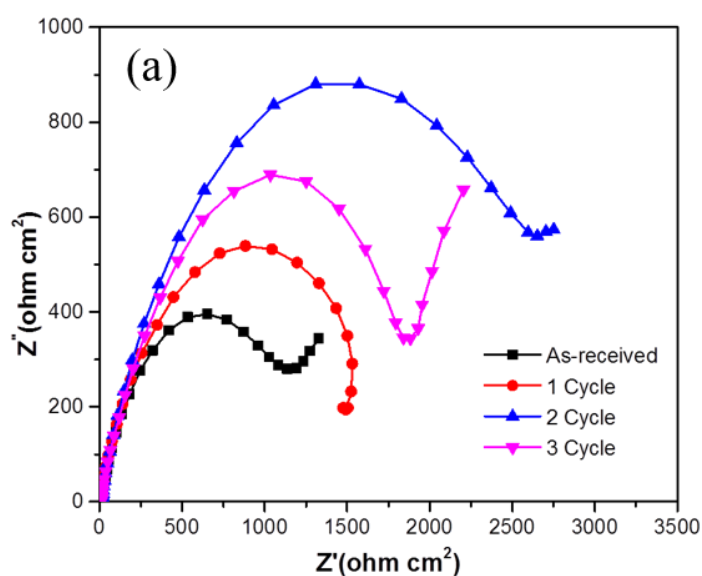
Figure 5.20 Nyquist plots of as-received and MAF processed samples

Figure 5.20 shows Nyquist plots of samples immersed in 3.5%wt NaCl solution. The arc diameters of capacitive arcs of the MAF processed samples are increasing with increase in number of MAF cycles and this is due to increased corrosion resistance which shows the protective layer in the interface and the second represents the damaged protective layer.
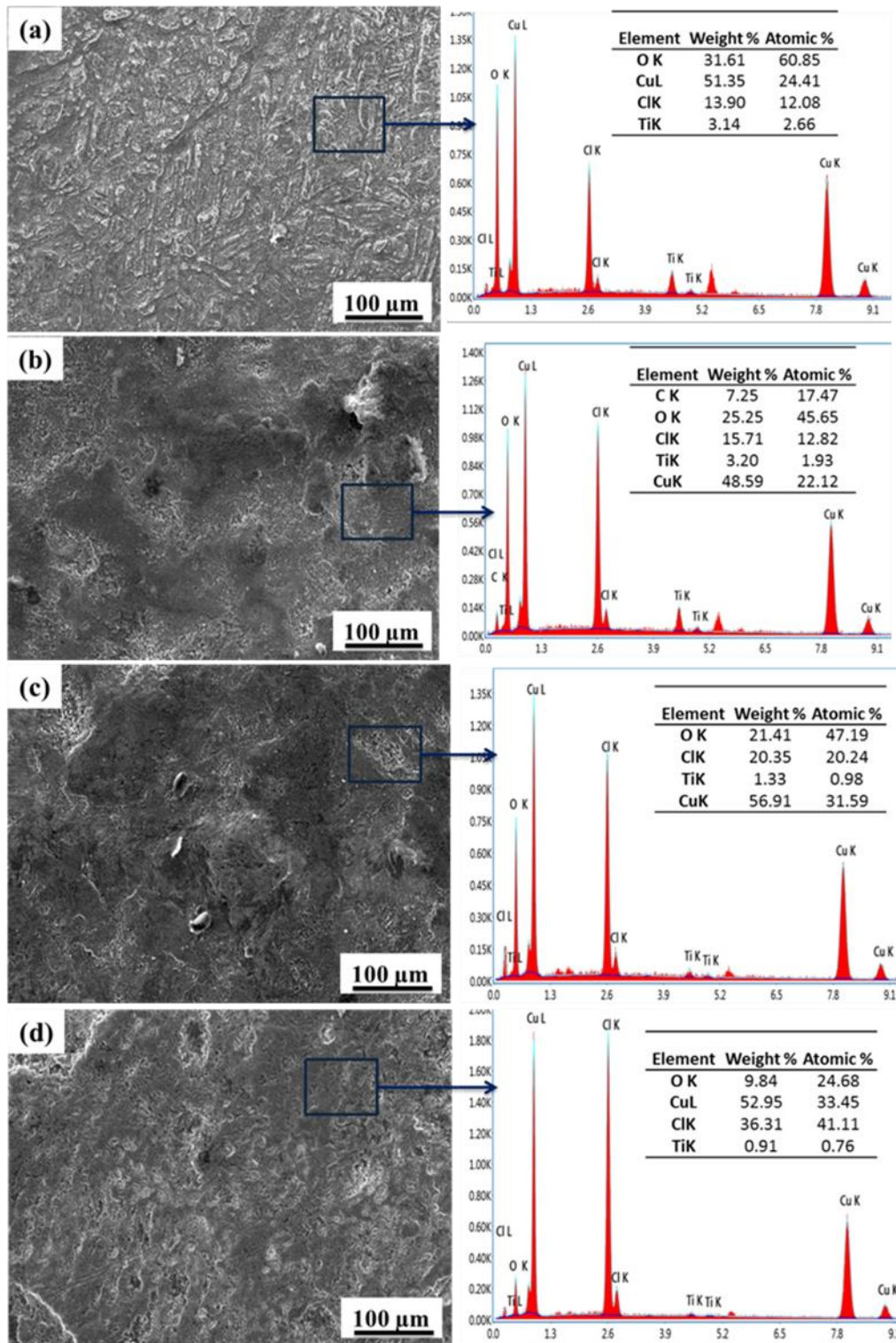
Figure 5.21 SEM images of corrosion samples for different MAF (a) as-received (b) 1 cycle (c) 2 cycle and (d) 3 cycle

SEM images of Cu-3%Ti sample after removing corrosion product on the surface is shown in Figure 5.21. Intergranular and pitting corrosion was observed, because of susceptibility of copper to intergranular corrosion in chlorine solution. Pitting corrosion occurred, because of micro-galvanic coupling between Cu and Ti. Figure 5.21 shows EDS mapping on corroded surface. As-received sample produced oxide layer of 36.29 wt%. With increase in number of MAF cycles, oxide formation on sample surface reduced, because of increased grain boundaries which acts as corrosion barrier and increased the corrosion resistance. Figure 5.22 shows XRD pattern of corroded sample processed by MAF for 3 cycles. CuCl and Cu_2O are the corrosion products observed in the XRD and act as protective passivation layer, which reduces corrosion attack on the sample.
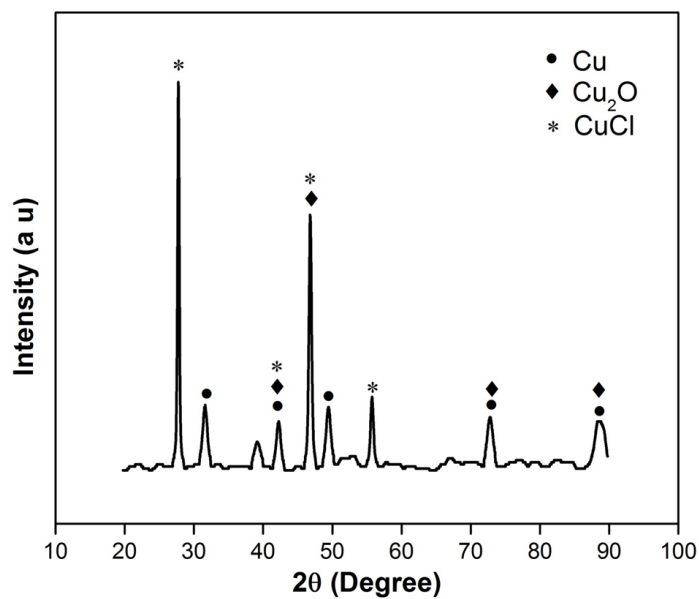
Figure 5.22 X-Ray Diffraction pattern of Corroded surface of 3 cycle MAF processed sample

5.6 Summary

MAF has been successfully carried out on Cu-3%Ti alloy at cryogenic temperature to study the microstructural changes, mechanical, wear and corrosion properties. The obtained results are summarized as below,

- Grain size decreased to ~250 nm after 3 cycles of MAF, resulting in micro-shear bands formation and transformation of grain boundaries from high angle to low angle.

- Mechanical properties improved in samples forged at cryogenic temperature. Maximum UTS (1126 MPa) was obtained in samples processed by MAF for 3 cycle with 18% elongation. Increase in the strength is due to grain boundary strengthening mechanism and increase in dislocation density with increase in number of MAF passes. Decreasing shear band width/twin width is also reason for improvement in both, strength and ductility of material.

- Hardness increased from 244 to 340 HV after 1 cycle of MAF. As the number of forging cycle increases, hardness increases due to increase in dislocation density and grain refinement. Maximum hardness value reached to 402 HV after 3 cycles of MAF.

- Fracture analysis of MAF processed sample shows that dimple size decreases after 1 cycle sample, because of grain refinement and strain hardening. After 1 cycle, dimple size started increasing. Increase in ductility for higher MAF cycles is due to decrease in the shear band width and twin width.

- As-received and 1 cycle, 2 cycle, 3 cycle MAF processed samples were subjected to dry sliding wear test to know the COF behaviour for different loading condition. COF value decreased for MAF processed samples. MAF processed samples showed low wear rate and wear resistance increased with increase MAF cycles due to increased hardness of samples.

- SEM micrograph of worn surface showed surface plastic deformation, ploughing and scratches, which increased with increase in load and decreased with increase in number of MAF passes. EDS analysis showed presence of oxygen peaks along with copper peak on the wear surface, thereby, confirming abrasion and oxidation wear mechanisms.

- EIS plots and Potentiodynamic polarization showed the corrosion behaviour of as-received and MAF processed samples. MAF processed samples showed better corrosion resistance properties due to refined microstructure.

CHAPTER 6

6. RESULTS AND DISCUSSION OF Cu-4.5%Ti ALLOY PROCESSED BY MAF

Cu-4.5%Ti alloy was processed by MAF at cryogenic temperature upto 3 cycles. As received and MAF processed samples were characterized for microstructure, mechanical properties and results are discussed in the following sections. MAF processed samples are subjected to wear studies at 10 and 20 N load at different speed and sliding distance. MAF processed samples were subjected to corrosion studies to know corrosion properties of unprocessed and MAF processed samples.

6.1 Microstructure Analysis

(i) Optical and SEM analysis

Figure 6.1(a) shows the optical micrograph of as-received sample, which shows equiaxed grains of size 70 µm with small fraction of twins. Figure 6.1 (b) shows microstructure of sample of 1 cycle MAF, with the formation of shear bands within the grains and average grain size was found to be 5 µm. Figure 6.1(c) shows optical micrographs of 2 cycle MAF processed samples (ε= 1.06), indicating the formation of shear bands. Grain boundaries become ambiguous and identification of individual grains became difficult, because of high density of shear bands, which directly depends on the accumulated strain at higher forging cycles. Figure 6.1 (d) shows optical micrograph of 3 cycle MAF sample, with cumulative strain of 1.64. Fine subgrain and high-density shear bands were observed, with minimum in gap between the shear-bands. Similar micrographs were observed in multiaxial cryo-forged Copper (Kobayashi et al. 2017) and Al 6061 alloy (Huang et al. 2004). At low temperature, shear bands are easily developed during deformation. Finally, elongated type of grain substructure was observed (Dasharath et al. 2016).

SEM micrographs are shown in Figure 6.2. Bimodal grain structure is observed in as received sample. Figure 6.2 (b) shows microstructure after 1 cycle of MAF, which shows the formation of shear bands within the grain. Figure 6.2 (c)-(d) shows increasing density of shear bands and it is difficult to identify the individual grains after 3 cycles of MAF.
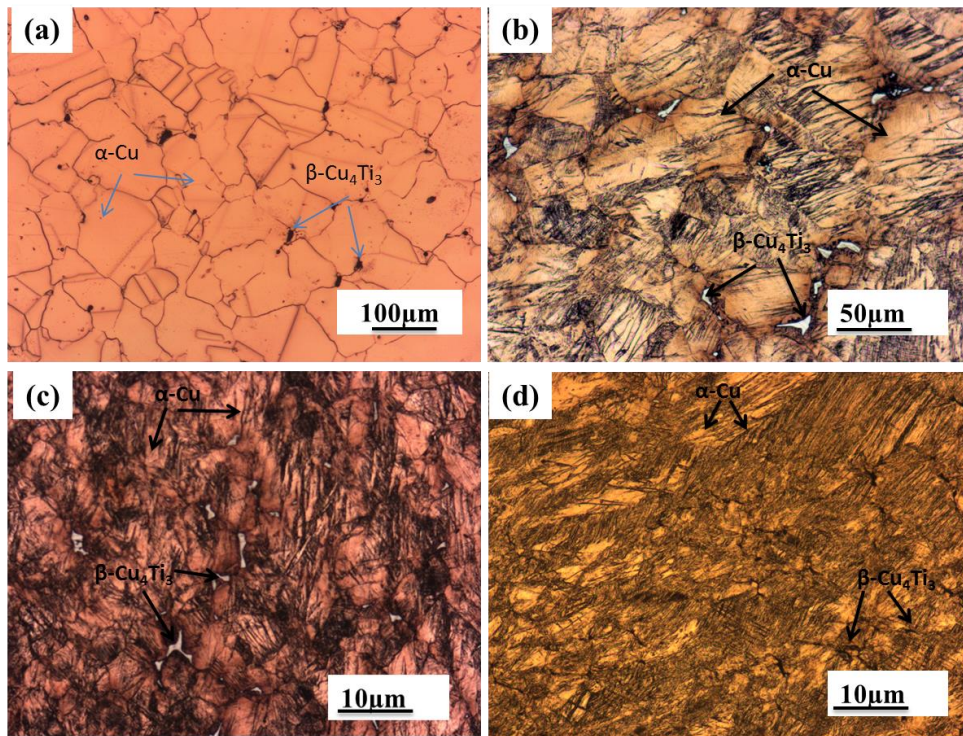
Figure 6.1 Optical micrography of (a) As- received and MAF processed (b) 1 cycle (c) 2 cycles (d) 3 cycles
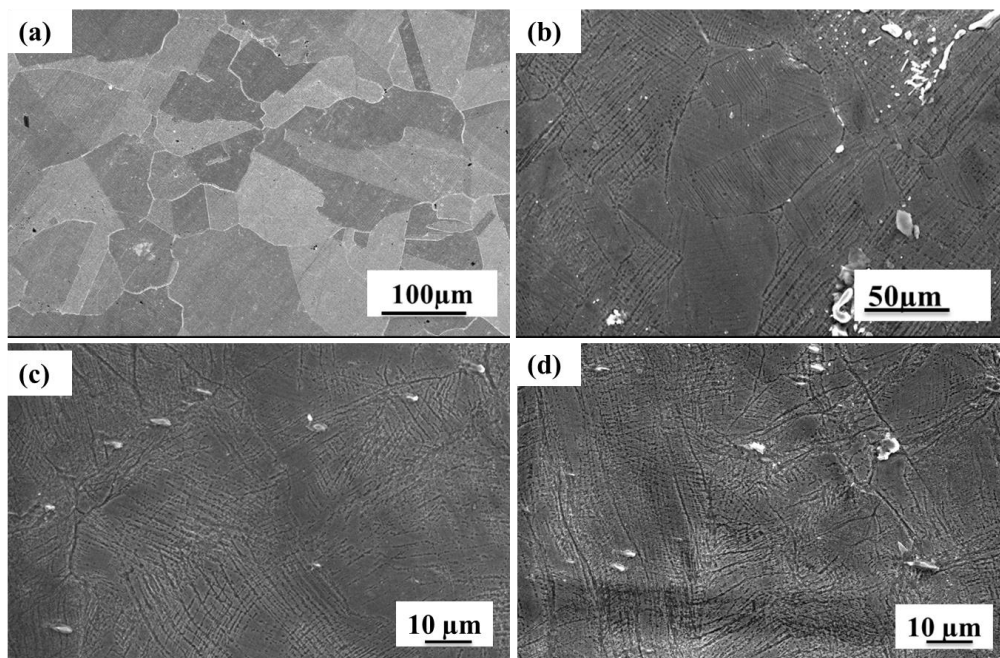
Figure 6.2 SEM images of sample processed by different MAF cycle (a) As- received (b) 1 cycle (c) 2 cycles (d) 3 cycles

(ii) TEM analysis

Figure 6.3 depicts the TEM micrographs of samples processed by 2 and 3 cycle MAF, with insets showing SAED patterns. Figure 6.3 (a) and (b) show formation of shear bands, samples deformed by 2 cycles MAF process. Figure 6.3 (c) shows the electron diffraction pattern of 2 cycle sample with zone axis (Z) of [011] on the same pattern. Figure 6.3 (d-e) shows the TEM micrograph of 3 cycles cryo-forging sample and Figure 6.3 (f) shows electron diffraction pattern of same sample. 3 cycle, SAED pattern contains continuous rings with planes are mentioned (101), (110), (111), (200) and (113). After 3 cycles, shear band thickness reduced to 200 mm, with increase in shear band density, because of accumulation of large strain. Figure 6.3 (b) and corresponding SAED pattern (Figure 6.3 c) show periodically arranged spotted rings with broad and bright regions that are stretched, because of diffraction from elongated grains. SAED pattern in Figure 6.3 (f) shows continuous and narrow rings, because of fine deformed grains with LAGBs (Dasharath et al. 2016).
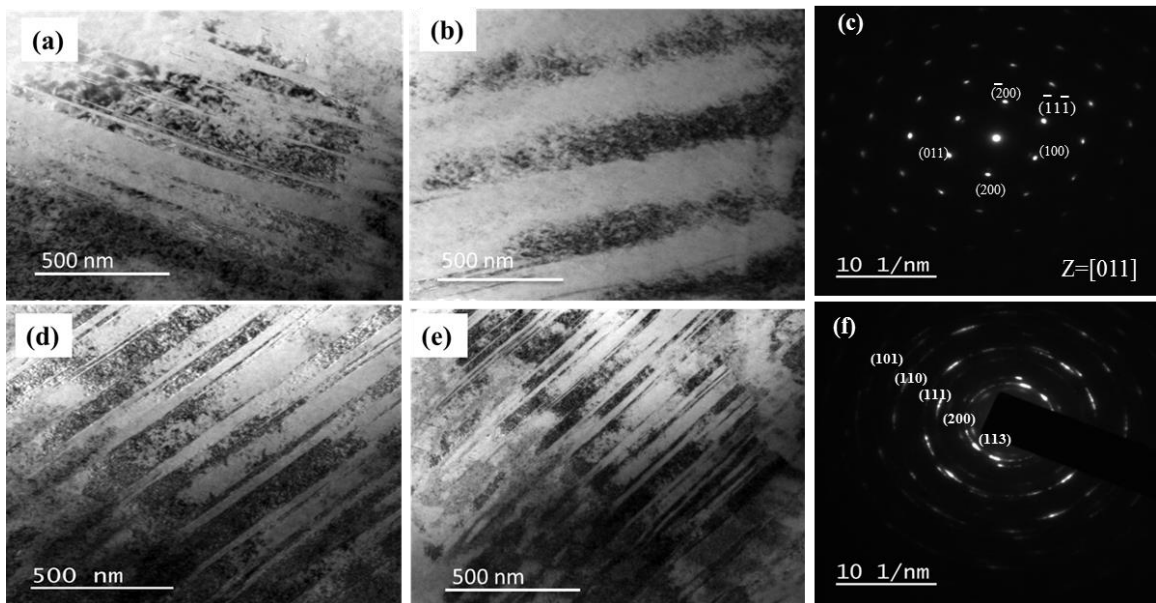
Figure 6.3 TEM micrographs of MAF processed (a-b) 2 cycles, (c) Electron diffraction pattern of 2 cycle and (c-d) 3 cycles samples, (f) Electron diffraction pattern of 3 cycle

(iii) EBSD analysis

Figure 6.4 (a)-(d) show Inverse Pole Figure (IPF) maps of as-received and MAF processed samples. Crystallographic orientations were observed and are expressed in different colors in a standard stereographic triangle (Figure 6.4 (e)). As-received sample shows equiaxed grains and fine elongated grains were observed in MAF 3 cycle sample. Misorientation angle distribution of as-received and MAF processed samples is shown in Figure 6.5.
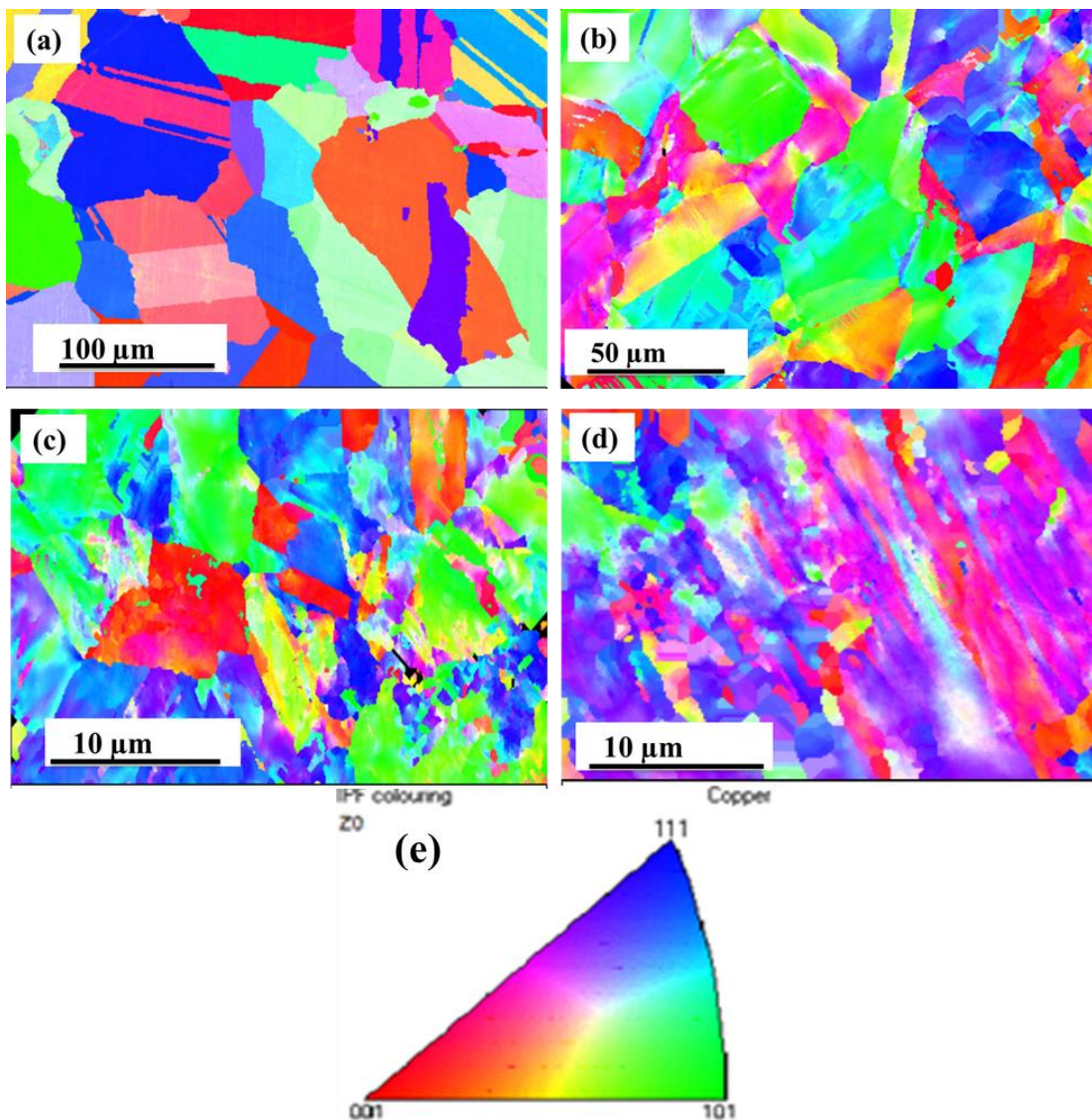
Figure 6.4 IPF maps: (a) As-received, (b) MAF 1 cycle, (c) MAF 2 cycles, (d) MAF 3 cycles, and (e) standard stereographic triangle for inverse pole figure
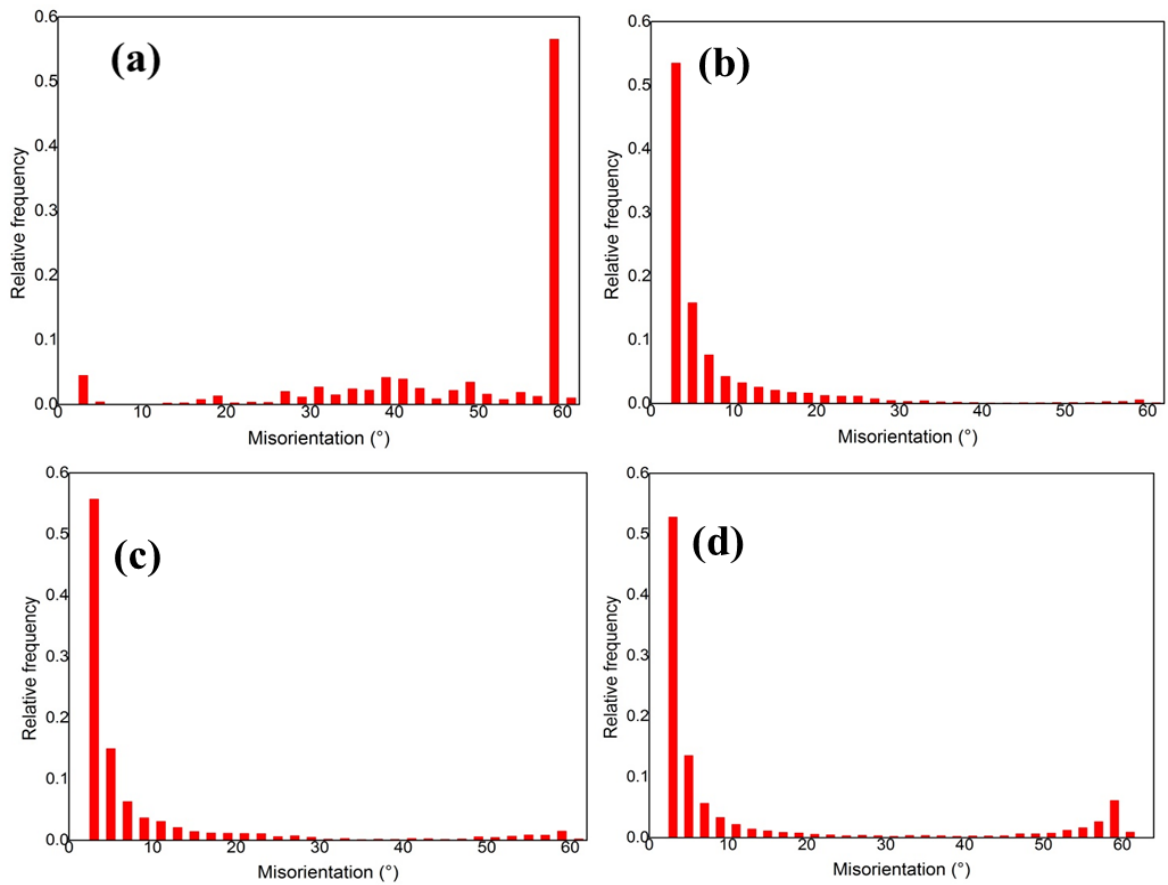
Figure 6.5 Misorientation angle distribution of samples processed by different MAF cycles: (a) As-received, (b) 1 cycle, (c) 2 cycles, and (d) 3 cycles

After 1 cycle, low angle (2-15°) misorientation are high, and play major role in dislocation strengthening. Strong peaks were observed at high angle (60°) and in low angle (2°), which may be due to grain refinement mechanism. At higher cycles of MAF, strain accumulated in sample increases and HAGBs gets converted to LAGB (Sahu et al. 2017), leading to more stable microstructure. Grains elongated and oriented in one direction were found in samples processed by MAF for 3 cycles. Initial texture ranged from (100) to (111), as visible from IPF map (Figure 6.4) having coarser grains. After one cycle of MAF, coarse grains were refined and converted from HAGBs to LAGBs, as shown in Figure 6.5 (b).

6.2 XRD Analysis

XRD peaks are shown in Figure 6.6. Change in intensity and broadening of peaks of planes (111), (220), (200) and (311) are observed in samples processed by MAF up to 2 and 3 cycles. Observed changes are because of grain refinement and strain hardening during MAF processing and induced lattice strain (Krishna et al. 2017). Change in texture was observed when the material was processed by MAF and is evident from figure 6.6. Further, it is shown that strong variations in intensities of peaks and also peaks are shifted by one degree after 3 cycles of MAF, because of high density of dislocation in the deformed sample.
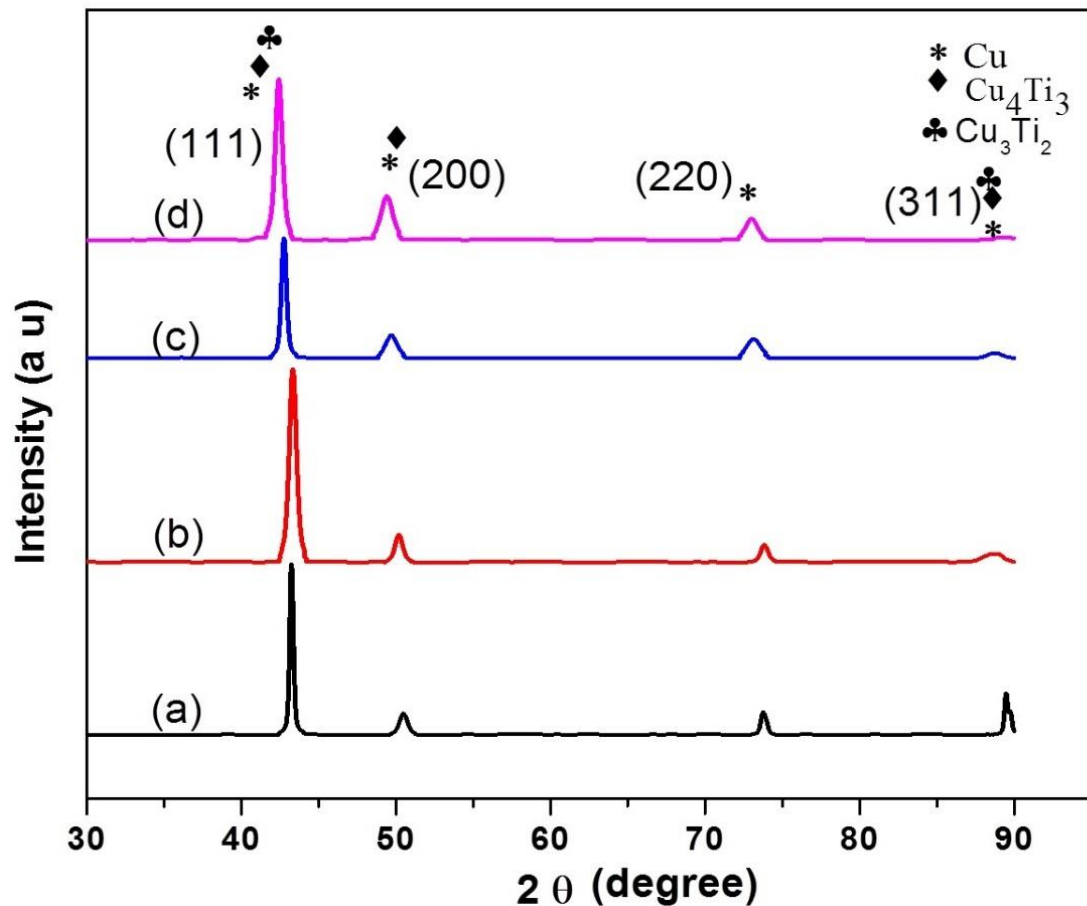
Figure 6.6 X-Ray Diffraction of sample processed by different MAF cycle (a) As-received (b) 1 cycle (c) 2 cycles (d) 3 cycles

6.3 Mechanical Properties

(i) Tensile properties

Engineering stress-Engineering strain curve is shown in Figure 6.8 (a) and corresponding mechanical properties are depicted in Figure 6.8 (b) and table 10. respectively. From Figure 6.8 (b), it can be observed that YS and UTS increased, as the number of MAF cycles is increased. UTS, YS and elongation for as-received samples were measured and reported as 641 MPa, 445 MPa and 16%, respectively.
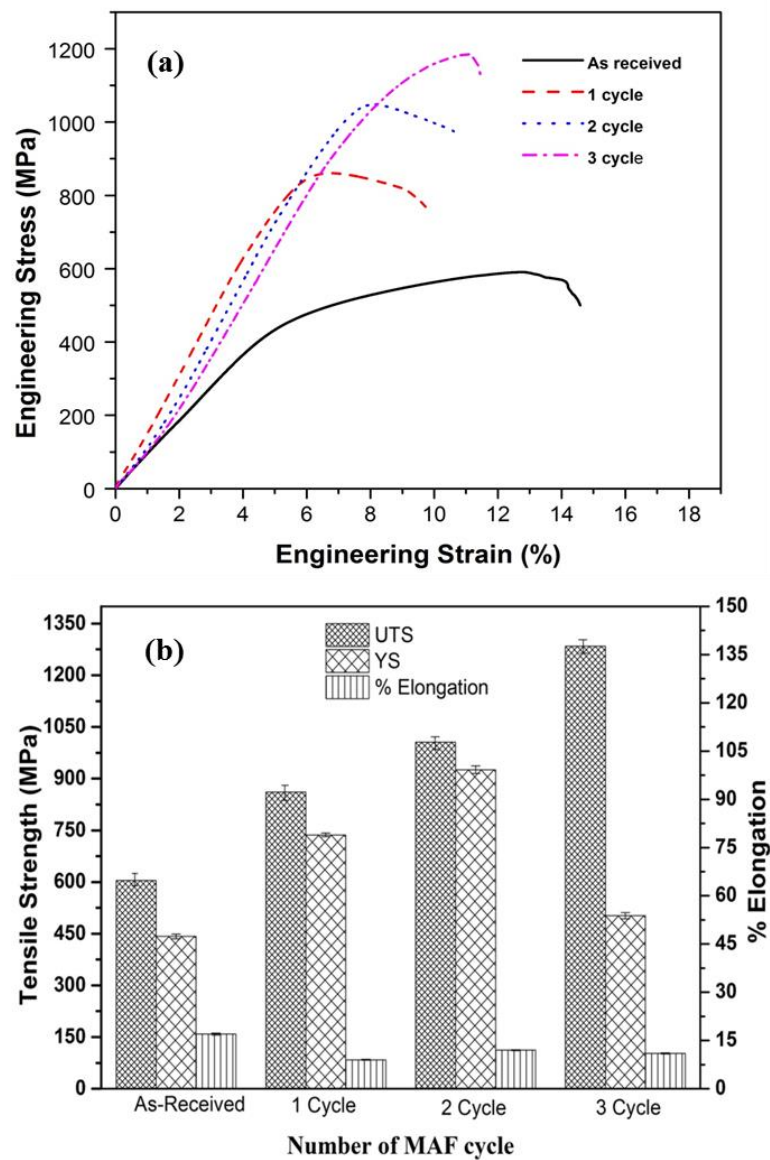
Figure 6.7 a)Engineering Stress- strain graph b) Bar chart of mechanical properties of MAF processed sample

After 1 MAF cycle (ε = 0.54) at cryogenic temperature, UTS and YS increased respectively to 861 MPa and 759 MPa, but elongation reduced to 9%. After 2 cycles of MAF, UTS increased to 1016 MPa, YS improved to 926 MPa and elongation raised to 10%, due to decrease in twin space width and decrease in shear band width (Dao et al. 2006, Gupta et al. 2016). Maximum tensile strength was obtained for 3 cycles (1284 MPa) and percentage elongation increased to 11%. Increase in strength is due to grain refinement, strengthening of sub-grain boundaries and dislocation strengthening. In addition, decrease in twin width plays a major role in improvement of strength and ductility, during MAF (Dao et al.2006). Relationship between strength (YS and UTS), hardness and average grain size is represented in figure 6.10, which clearly shows the improvement in strength and hardness with decrease in grain size. This relationship can easily be understood from the well-known Hall-Petch equation (Nieh et al.1991). Similar kind of behavior between strength and grain size was also obtained by Luo (Luo et al.2016, 2012, 2018).

(ii) Vickers Microhardness

Omni-Tech hardness machine was used to estimate Vickers Microhardness (HV) of undeformed and deformed samples. Hardness of as-received material was 252 HV. After first cycle of MAF, hardness increased to 358 HV. Hardness increased to 392 HV and 428 HV, respectively, in samples processed up to 2 and 3 cycles of MAF and is shown in Figure 6.8. Mechanical properties of both unprocessed and processed samples are tabulated in table 10. Grain refinement and strain hardening are the reasons for increase in hardness of the sample. Relationship between hardness, YS and UTS with average grain size is shown in Figure 6.9.

Table 10 Mechanical properties of as-received and MAF processed sample

Sample No.	UTS (MPa)	YS (MPa)	Elongation (%)	Hardness (HV)	Average grain size (µm)
As-received	605±6	442±7	17±0.5	252±12	70±8
1 cycle	861±8	737±9	9±0.2	358±8	5±2
2 cycle	1006±12	926±7	12±0.3	392±10	0.8
3 cycle	1284±9	1007±8	11±0.25	428±10	0.2
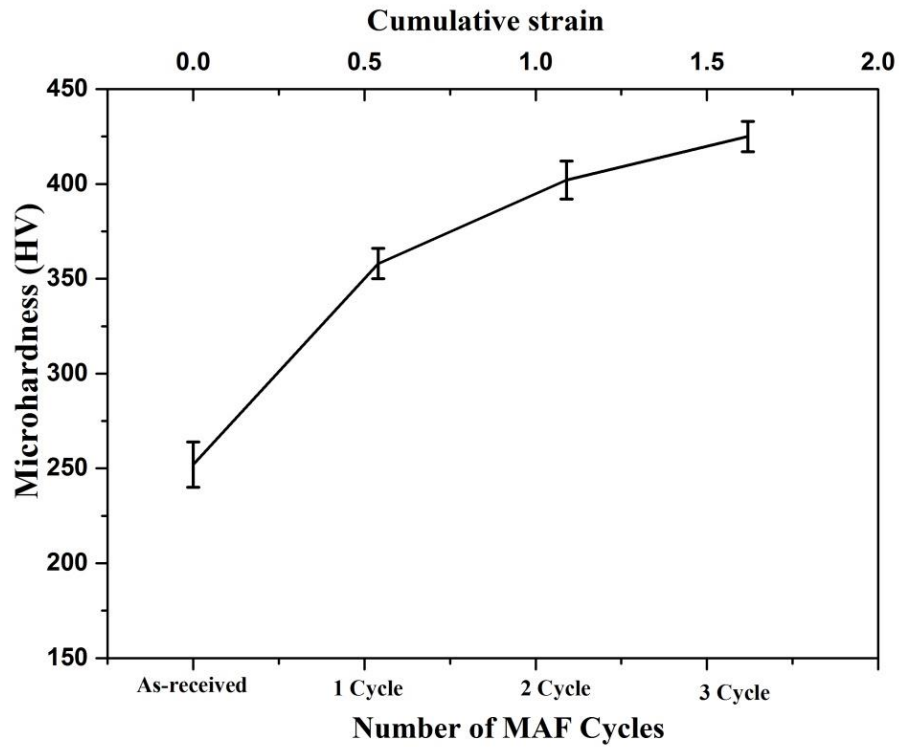
Figure 6.8 Vickers microhardness of sample processed by different MAF cycle
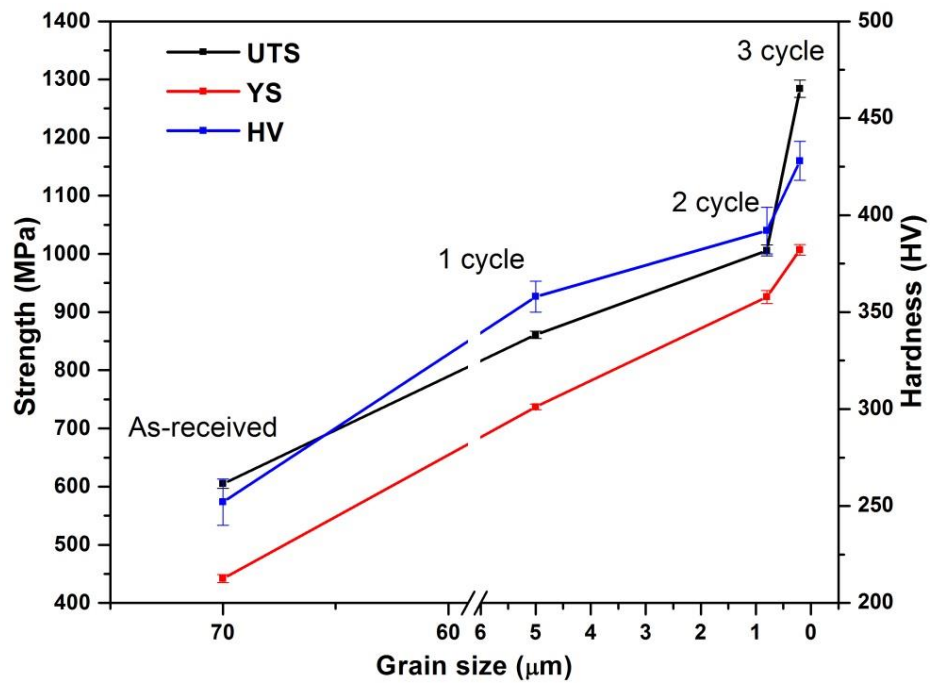
Figure 6.9 Variation of mechanical properties (UTS, YS, and hardness) with average grain size

(iii) Fractography

Fractured surfaces were analyzed using SEM. Figure 6.10(a) shows fractured surface of as-received sample, and it contains large dimples of ~25µm over the entire surface, and it is a ductile type of fracture.
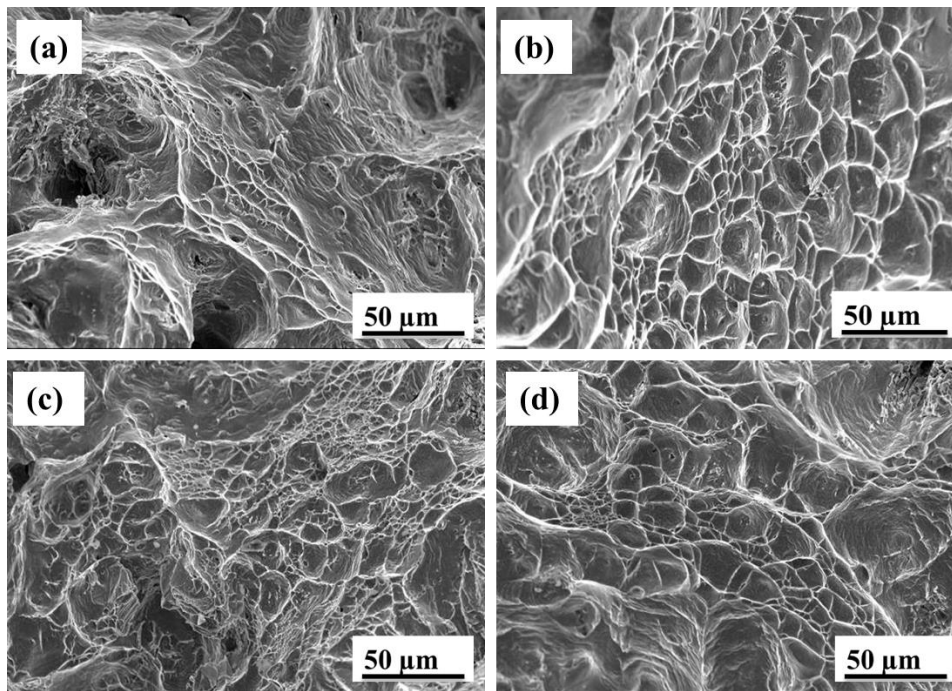
Figure 6.10 SEM micrography of tensile fractured surface of sample processed by different MAF cycle (a) As- received (b) 1 cycle (c) 2 cycles (d) 3 cycles

Figure 6.10(b) shows fractured surface of 1 cycle MAF processed sample where the dimple size is decreased to 6 µm. From Figure 6.10(c and d), it is observed that the dimple size increases to 8 µm and 14 µm, respectively, after 2 and 3 cycle of MAF. Increase in dimple size, after 2 cycles, is because of increase in ductility of the material. This shows that dimple size is directly related to ductility of material. Reduction in dimple size in MAF processed samples is due to work hardening and grain refinement (Dasharath et al.2016).

6.4 Wear behaviour of Cu-4.5%Ti alloy

(i) COF during wear test

 Two loads and two sliding distances were selected as varying parameters to conduct wear test using DUCOM pin-on-disc wear testing machine. Loads of 10N and 20N and sliding distances of (500 m, 1000 m, 1500 m, 2000 m, 2500 m and 3000 m) were selected. For each condition, 3 trials were conducted and the average COF values are obtained for different conditions and are plotted in Figure 6.11. As the number of MAF cycles increased, COF reduced indicating wear resistance in MAF processed samples. Table 11 shows the variation of COF with MAF cycles for different loads and velocities.
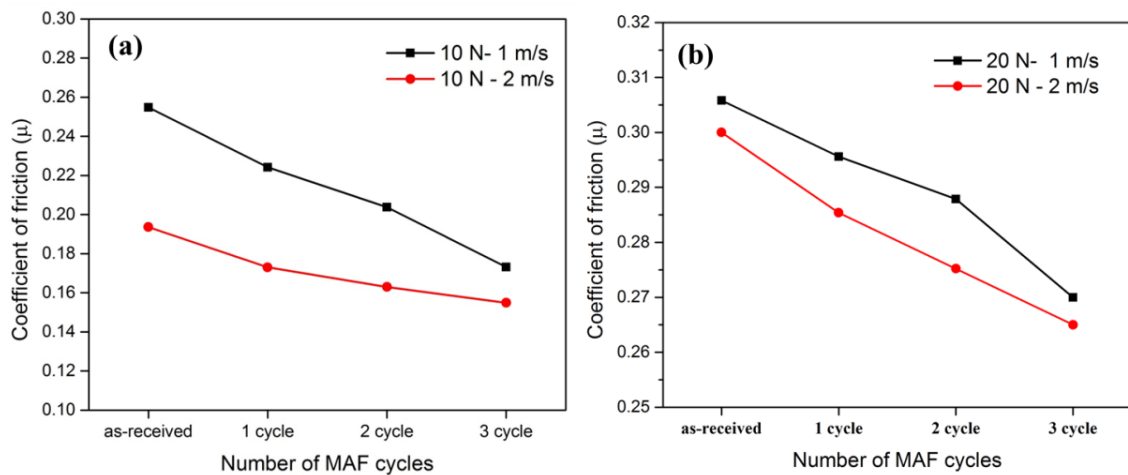
Figure 6.11 COF curves for samples under 10 N and 20 N load with (a) 10N with 1 m/s and 2 m/s (b) 20 N with 1 m/s and 2 m/s.

Table 11 COF values at different loads and different velocities

Material/Condition	10 N-1 m/s	10 N-2 m/s	20 N-1 m/s	20 N-2 m/s
As-received	0.25	0.19	0.35	0.30
1 cycle	0.22	0.17	0.28	0.29
2 cycle	0.20	0.16	0.27	0.28
3 cycle	0.17	0.15	0.26	0.27

(ii) Volume mass loss

Figure 6.12 shows the variation of wear volume loss with different sliding distances for as-received and MAF processed samples. Figure 6.12 (a) and (b) shows the variation of wear volume loss with different sliding distances, tested at 1 m/s with two different loads. Similarly, Figure 6.12 (c) and (d) shows the variation of wear volume loss with different sliding distances, tested at 2 m/s with 10 N and 20 N. It is observed that cumulative volume loss is linearly varied with sliding distances for both as-received and MAF processed samples. In all material conditions, volume loss increases with increase in load and sliding velocity. As the number of MAF cycles increased, volume mass loss decreased, because of improvement of hardness.
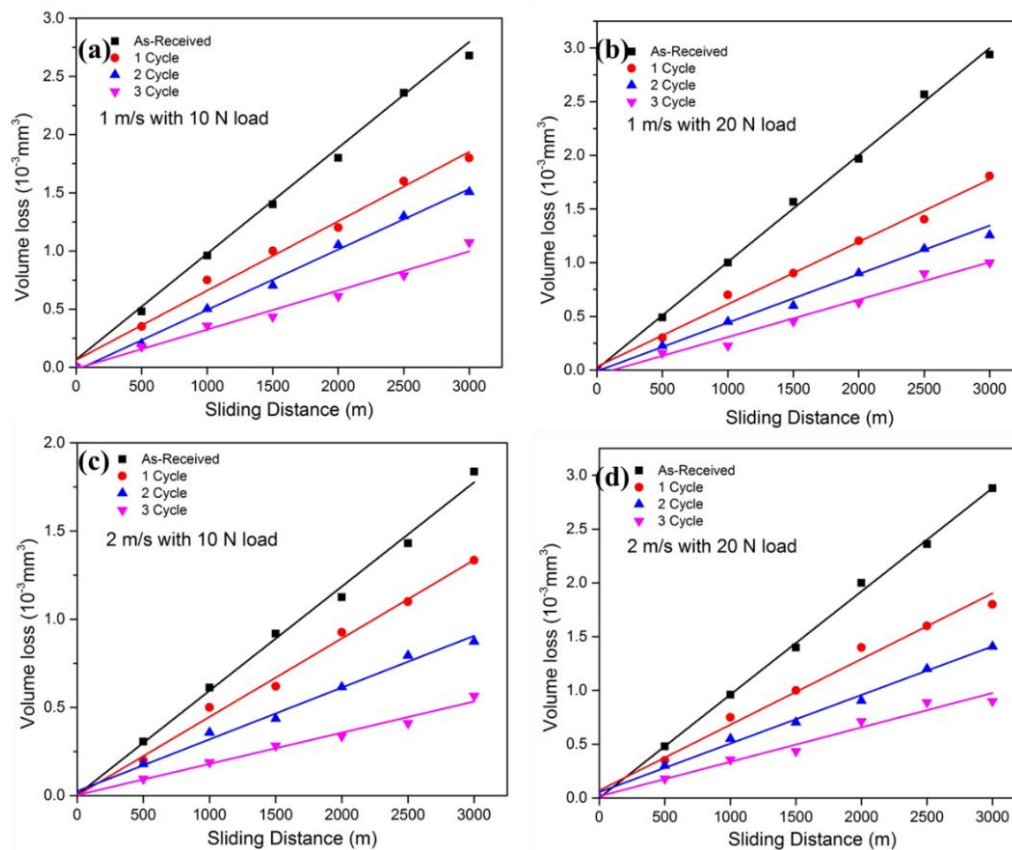
Figure 6.12 Volume mass loss (mm^3) v/s Different sliding distances (a) 1 m/s with 10 N (b) 1 m/s with 20 N (c) 2 m/s with 10 N (d) 2 m/s with 20 N.

(iii) Wear rate and wear morphology

Wear mass loss of the material, subjected to different loads and sliding distances, followed the same trend as that of COF. Samples processed by MAF up to 3 cycles, showed reduced wear rate loss, because of increased microhardness distribution, which avoids loss of material due to sliding motion of the sample, where the rotating disc prevents formation of delamination and wear debris. Wear mass loss for different conditions is shown in Figure 6.13.
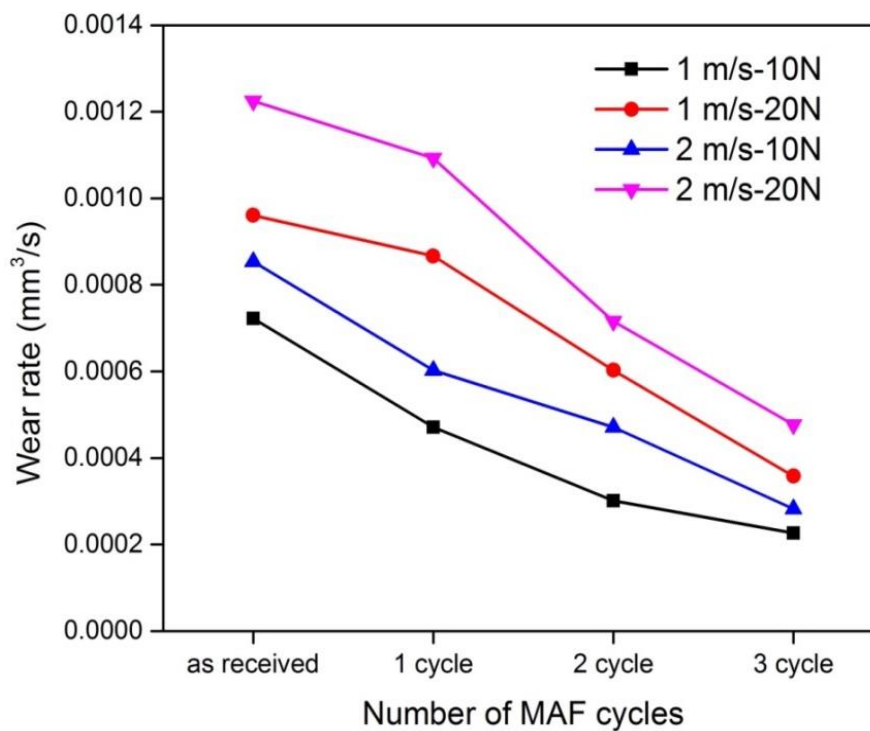
Figure 6.13 Wear rate versus MAF cycle

Table 12 shows wear rate at different velocities and different loads. Samples of 3 MAF cycles showed high wear resistance property, because of higher hardness value due to grain refinement. Figures 6.15 and 6.16 show worn surfaces of as-received and MAF processed samples at load of 10 N with sliding velocity 1 m/s and sliding distance 3000 m. Similarly, figures 6.17 and 6.18 show worn surfaces of unprocessed and processed samples for 20 N load with sliding velocity 2 m/s.

Table 12 Wear rate at different velocities and different loads

Material/Condition	10 N-1 m/s	10 N-2 m/s	20 N-1 m/s	20 N-2 m/s
As-received	7.2244×10^{-4}	8.536×10^{-4}	9.6084×10^{-4}	12.2×10^{-4}
1 cycle	4.71×10^{-4}	6.0288×10^{-4}	8.6664×10^{-4}	10.9×10^{-4}
2 cycle	3.0144×10^{-4}	4.71×10^{-4}	6.0288×10^{-4}	7.1592×10^{-4}
3 cycle	2.2608×10^{-4}	2.826×10^{-4}	3.5796×10^{-4}	4.768×10^{-4}

Worn surfaces showed grooves, micro cracks, delamination, ploughing and wear debris along the sliding direction, which are caused due to initiation and propagation of subsurface cracks, resulting in removal of material in the form of flakes or wear debris as shown in figures. 6.15 to 6.18. Worn surfaces appear to be smooth in deformed samples, due to improved microhardness distribution which helps in avoiding the formation of wear debris and delamination. EDS analysis revealed the presence of oxygen along with copper. Since, copper combines with oxygen, to form oxide, Cu is more prone to oxidation and can be considered as one of the reasons for wear. Copper and oxygen are found on the wear surface in the areas of delamination, ploughing and wear debris and are shown in figures 6.19 and 6.20. Based on the above discussion we can conform the possibility of oxidation wear.
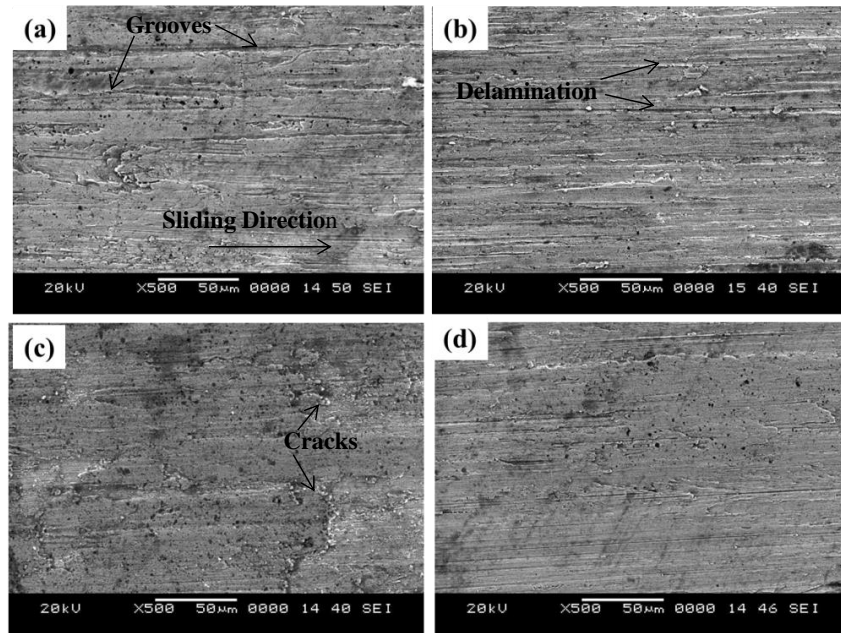
Figure 6.14 SEM images of worn surfaces of (a) As-received and MAF processed (b) 1 cycle, (c) 2 cycle, and (d) 3 cycle samples under 10 N load, 1 m/s with sliding distance 3000 m
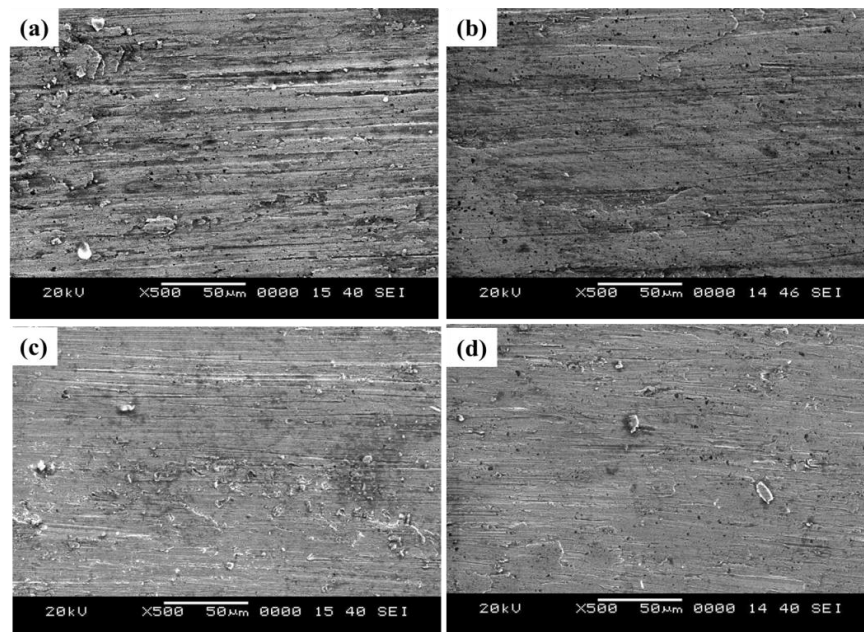
Figure 6.15 SEM images of worn surfaces of (a) As-received and MAF processed (b) 1 cycle, (c) 2 cycle, and (d) 3 cycle samples under 20 N load, 1 m/s with sliding distance 3000 m
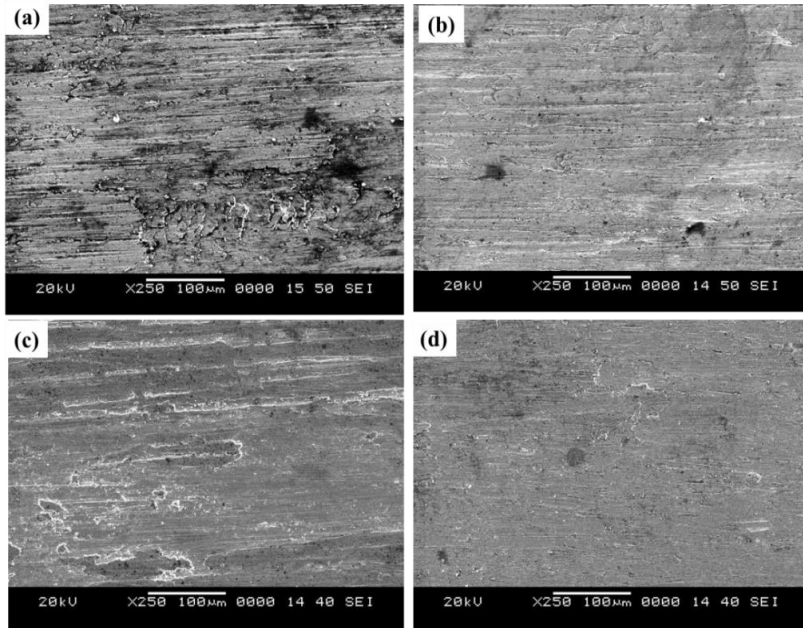
Figure 6.16 SEM images of worn surfaces of (a) As-received and MAF processed (b) 1 cycle, (c) 2 cycle, and (d) 3 cycle samples under 10 N load, 2 m/s with sliding distance 3000 m
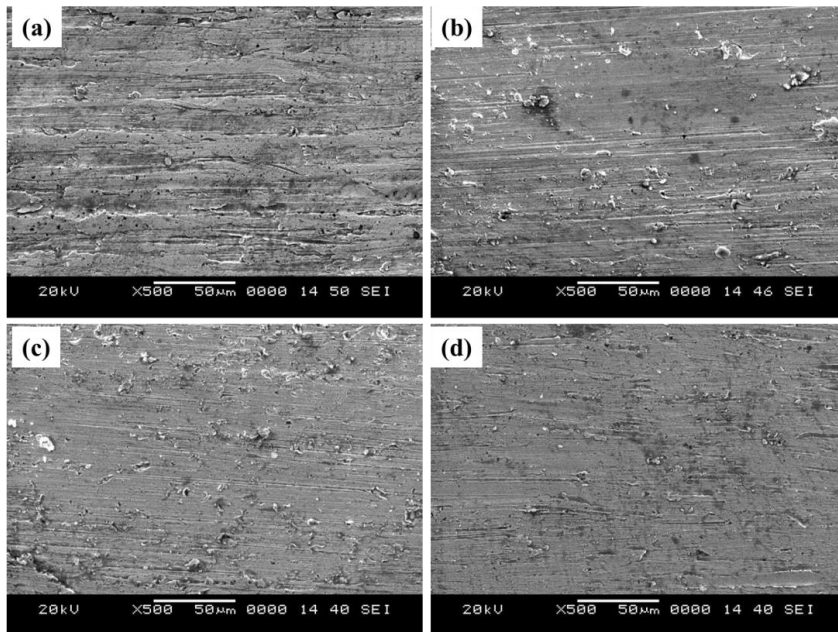
Figure 6.17 SEM images of worn surfaces of (a) As-received and MAF processed (b) 1 cycle, (c) 2 cycle, and (d) 3 cycle samples under 20 N load, 2 m/s with sliding distance 3000 m
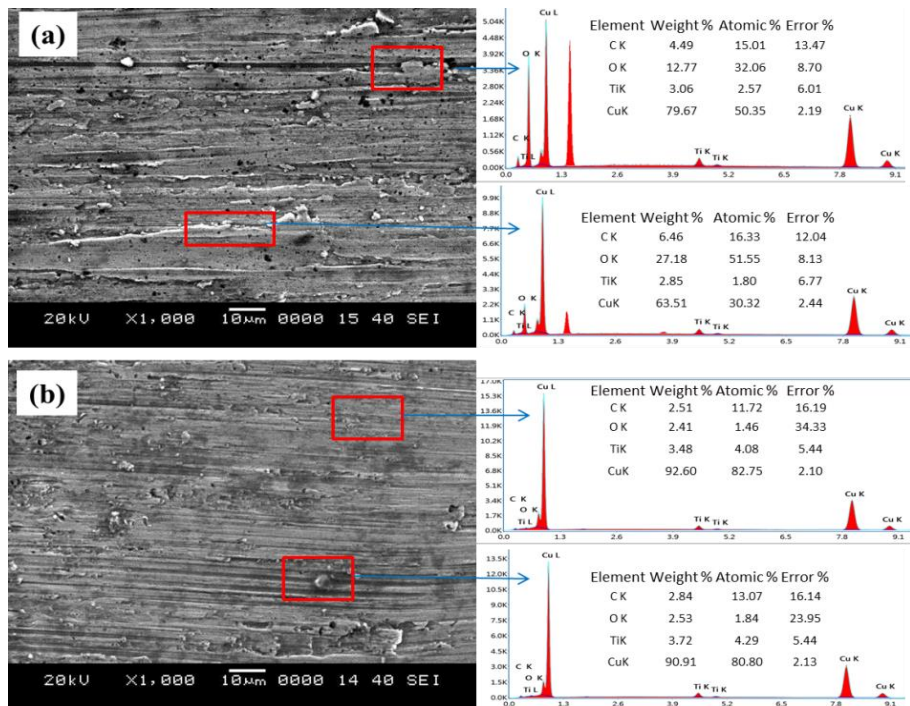
Figure 6.18 EDS analysis of Cu-4.5%Ti (a) As-received and (b) 3 cyle MAF processed sample 2 m/s at 10 N
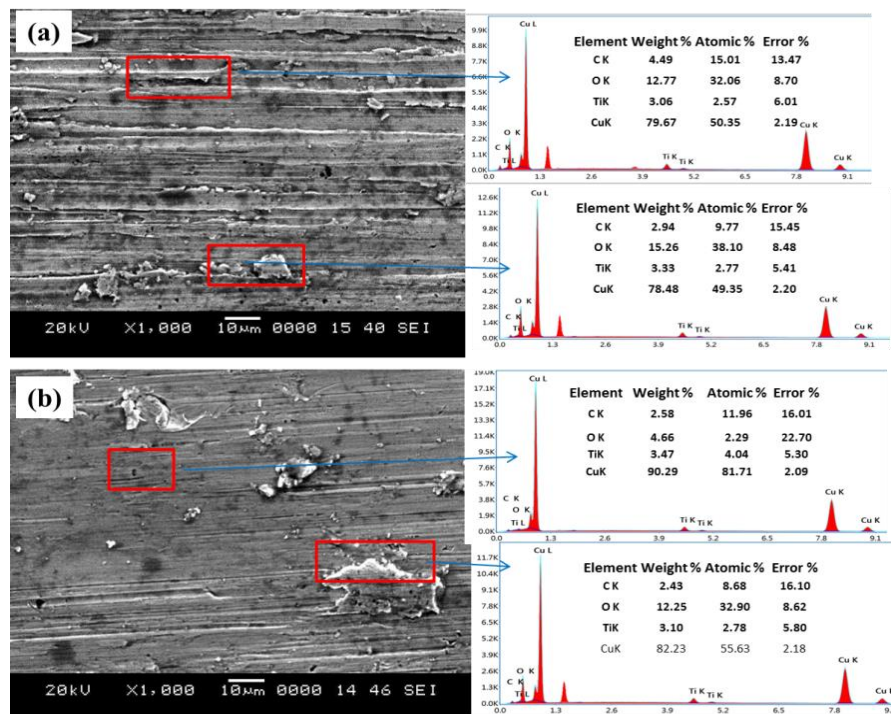
Figure 6.19 EDS analysis of Cu-4.5%Ti (a) As-received and (b) 3 cyle MAF processed sample at 2 m/s at 20 N

6.5 Corrosion behaviour

MAF processed Cu-4.5%Ti alloy was subjected to corrosion test to know the corrosion behavior by conducting electrochemical measurement test.

(i) Potentiodynamic Polarization

Potentiodynamic polarization test was conducted on both as received and MAF processed samples to study the corrosion behavior. Corrosion rate, corrosion potentials (E_{corr}) and Corrosion current density (I_{corr}) were extracted from polarization curves (figure 6.21) and values are clearly tabulated in table 13.
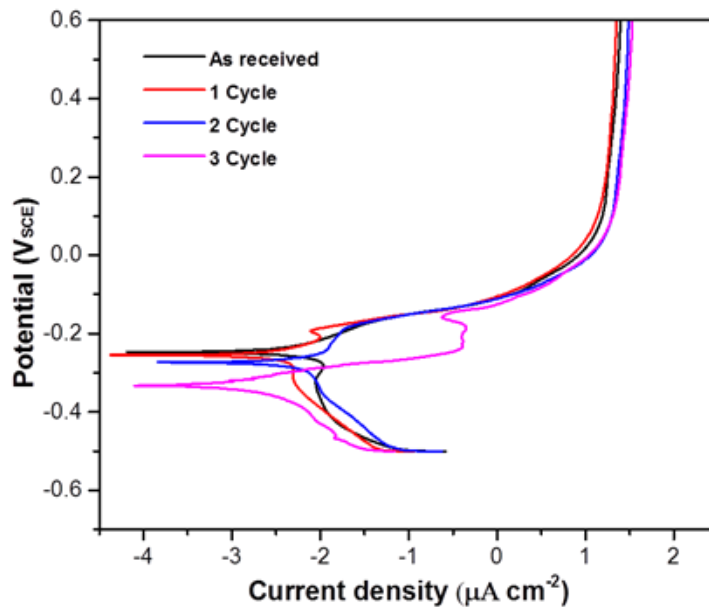
Figure 6.20 Electrochemical potentiodynamic polarization plots of unprocessed and MAF processed sample

X axis represents corrosion current and Y axis represents corrosion potential. MAF processed samples showed reduced I_{corr} value, which indicates higher corrosion resistance. Corrosion current density (I_{corr}) can be measured using Tofel extrapolation method with the help of EC-lab Ver. 10.37 software. With increase in MAF passes, corrosion potential (E_{corr}) shift towards a more negative value and current density (I_{corr}) value was found to decrease. Finally, potentiodynamic polarization results shows that increase in MAF passes gradually enhances corrosion resistance, which is because of grain refinement.

Table 13 Electrochemical kinetic parameters like corrosion potential, corrosion current density, and corrosion rate (mm/y).

Materials Cu-4.5%Ti	E_{corr} (V_{SCE})	i_{corr} ($\mu A/cm^2$)	Corrosion rate (mm/y)
As-received	-251.39	5.38	0.125
1 Cycle	-234.0	4.24	0.098
2 Cycle	-246.88	3.52	0.072
3 Cycle	-251.88	2.82	0.055

(ii) Electrochemical impedance spectroscopy (EIS)
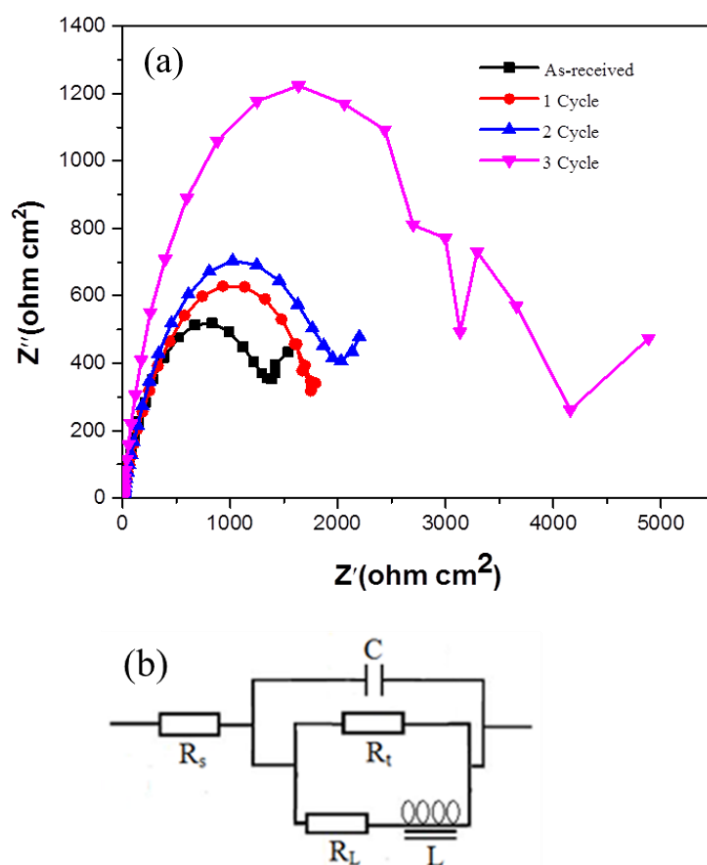
Figure 6.21 Nyquist plots of as-received and MAF processed samples

Corrosion behavior was also studied using EIS test with frequency ranging from 100 kHz to 10 mHz and the amplitude of sinusoidal potential signal maintained

at 5 mV. EIS plots obtained for different conditions are shown in figure 6.22, which represents the Nyquist plots. The first arc is the capacitance arc which represents the protective film formation and the second arc or tail region represents the degradation or damage to protective layer formed on the surface. The diameter of the arc is proportional to the variation of corrosion rate. The diameters of capacitive arcs of the MAF processed samples increase with increase in MAF cycles, which implies increased corrosion resistance.

SEM images of corroded MAF processed Cu-4.5%Ti samples are shown in figure 6.23. Intergranullar and pitting corrosions were observed, because of susceptibility of copper to intergranular corrosion in chlorine solution. Pitting corrosion occurred, because of micro-galvanic coupling between Cu and Ti. Figure 6.23 shows EDS mapping on the corroded surface. As-received sample produced oxide layer of 36.29 wt%. With increase in number of MAF cycles, oxide formation on sample surface reduced, because of increased grain boundaries which acts as corrosion barrier and increased the corrosion resistance. Figure 6.24 shows XRD pattern of corroded sample processed by MAF for 3 cycles. CuCl and Cu_2O are the corrosion products observed from XRD analysis and act as protective passivation layer, which reduces corrosion attack on the sample.
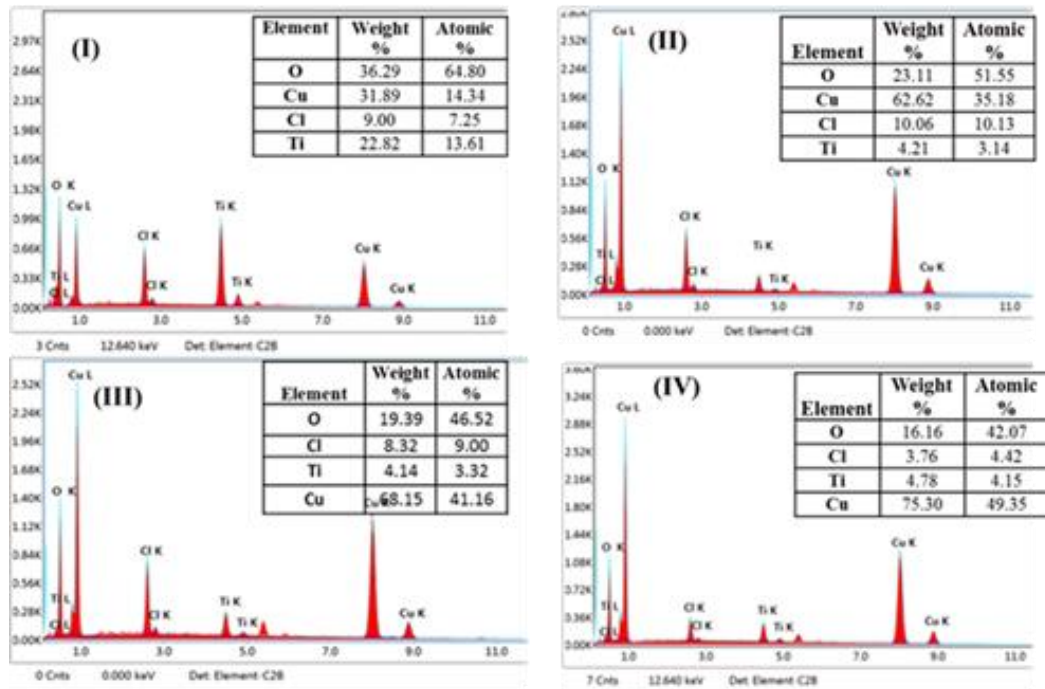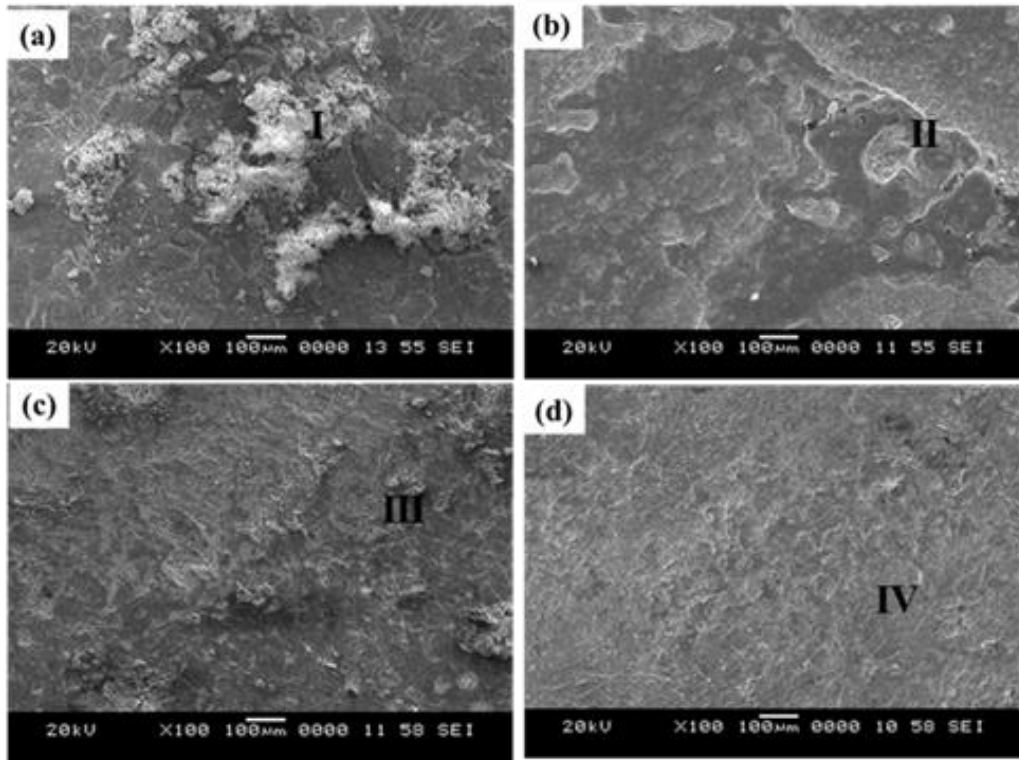
Figure 6.22 SEM images of corrosion samples for different MAF cyles.
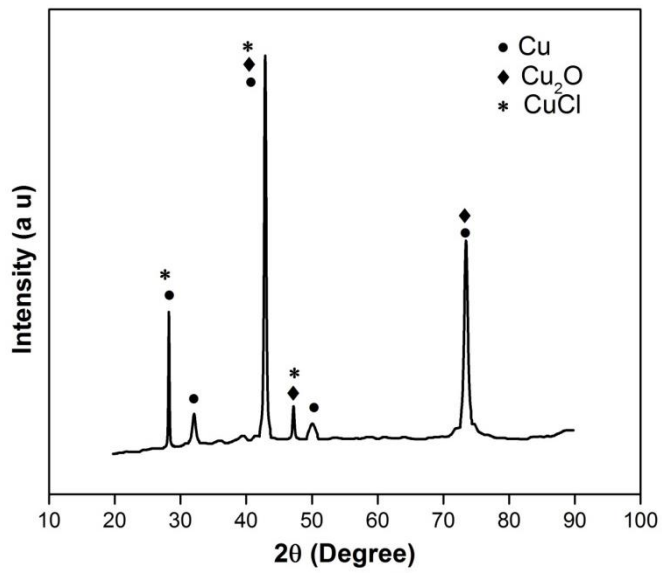
Figure 6.23 X-Ray Diffraction pattern of Corroded surface of 3 cycle MAF processed sample

6.6 Summary

MAF was used successfully to process Cu-4.5%Ti alloy upto 3 cycles, for a cumulative strain of 1.56, at cryogenic temperature. Microstructure, mechanical and corrosion properties were investigated and the results are summarized below.

- After 3 cycle of MAF, grain size reduced from 70 μm to ~200 nm (as observed from TEM). Grain refinement is because of the formation of micro shear bands. EBSD results shows transformation of HAGB to LAGB.

- YS, UTS and % elongation to failure was increased with increase in MAF cycles. Maximum UTS of 1284 MPa, YS 1007 MPa with 11% elongation was achieved after 3 cycles of MAF process at cryogenic condition. Grain boundary strengthening is the mechanism behind increase in strength.

- Microhardness increased from 225 HV to 428 HV for 3 cycle MAF processed sample. Driving mechanisms for increase in hardness are strain hardening and grain refinement.

- Fractured surface revealed that dimple size decreases in one cycle sample due to decrease in ductility. After 2 cycle of MAF, slight increase in dimples size was observed, because of increase in ductility. After 3 cycles surface looks to be of ductile-brittle kind of fracture.

- Dry sliding wear tests were performed on as received and MAF processed samples, to know the COF behaviour for different loading condition. COF decreased, as the number of MAF passes increased, due increased hardness of the sample. Wear mass loss reduced in MAF processed samples, when compared to that of as-received material. Wear mass loss directly depends on the hardness of the material.

- SEM micrograph of worn surface reveals surface deformation. Ploughing and scratches increased with increase in load and decreased with increase number of MAF passes.

- Potentiodynamic polarization results shows that corrosion resistance increased after MAF due to grain refinement. SEM and EDX morphology showed the formation of oxide layers and its compositions on the corroded surface.

CHAPTER 7

7. COMPARISON OF MAF PROCESSED Cu-1.5%Ti, Cu-3%Ti AND Cu-4.5%Ti ALLOYS

7.1 Microstructure and Mechanical properties

Tensile properties of MAF processed Cu-1.5%Ti, Cu-3%Ti and Cu-4.5%Ti up to 3 cycles are shown in figure 7.1. Increase in Ti content increases the strength of Cu-Ti alloys. From figure 7.1 it is observed that, average grain size of as-received samples for Cu-1. 5%Ti, Cu-3%Ti and Cu-4.5%Ti is 600 μm, 80 μm and 70 μm respectively. As %Ti increases, grain size decreases, because of increase in dissolution of Cu matrix (Nagarjuna et al.1996, 1994). Among MAF processed samples, grain size is maximum in samples processed for 1 cycle. During 1st cycle of MAF, grain refinement rate is high in all 3 alloys. High grain refinement is because of decrease in frequency of HAGB's and increase in LAGB's during the MAF process.
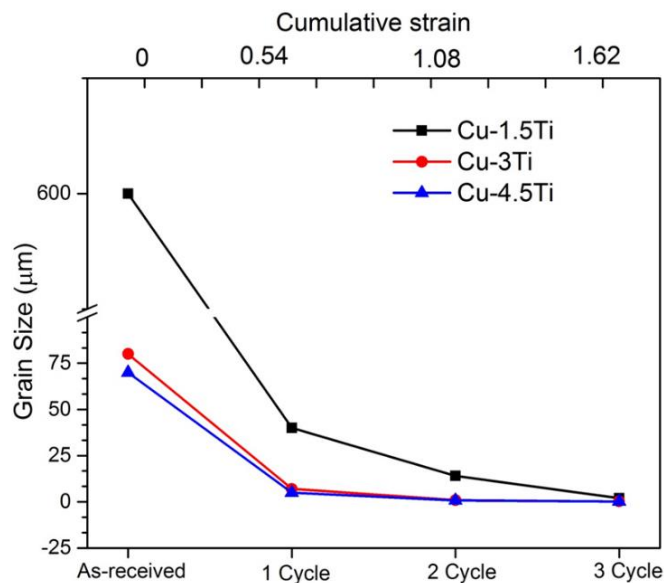
Figure 7.1 Comparision of Grain size v/s number of MAF cycles for different alloys

Alloys with higher Ti content increase the amount of inter-dendritic Cu_4Ti_3 and Cu_2Ti. Increase in volume fraction of Cu_4Ti_3 and Cu_2Ti phases results in decrease in ductility, which makes the alloy more of brittle in nature (Matthew S. Dargusch et al. 2010, Sobhani et al.2013).
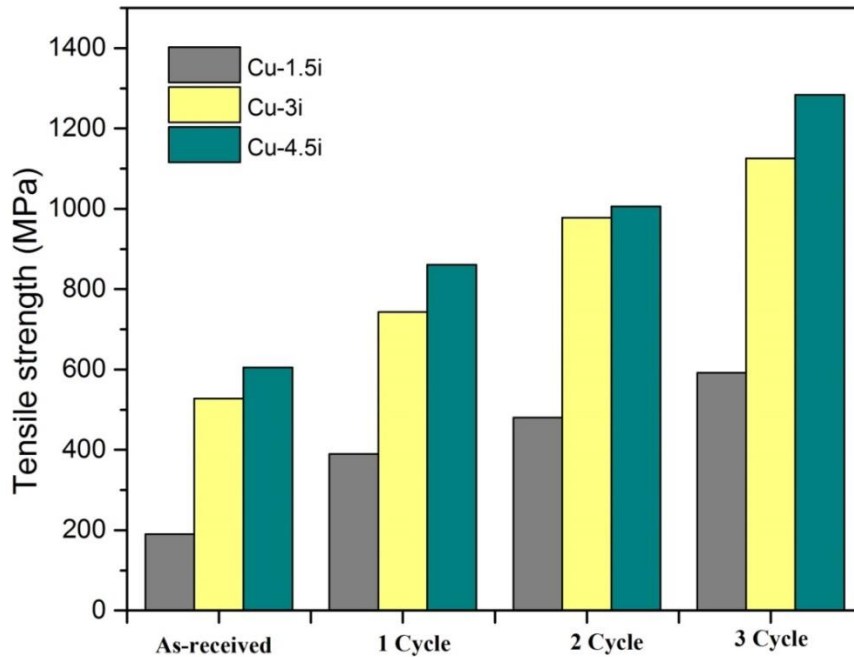
Figure 7.2 Comparision of Tensile Strength v/s number of MAF cycles for different alloys

Variation of tensile strength with different conditions of samples of Cu-1.5%Ti, Cu-3%Ti and Cu4.5%Ti are plotted on bar chat shown in figure 7.2. For each condition, 3 samples were tested for confirming the tensile properties of the samples. UTS of as-received alloys are 190 MPa, 528 MPa and 605 MPa, respectively. This shows clearly, when %Ti is increased, strength also increases. After 1 cycle of MAF (ε=0.54), UTS increased to 390 MPa, 743 MPa and 861 MPa, respectively. This increase in strength is due to grain boundary strengthening mechanism (Dieter, 1988). UTS increased further with increase in MAF cycles and reached to maximum of 592 MPa, 1126 MPa and 1284 MPa, respectively. Increase in strength is due to grain refinement, strengthening of sub-grain boundaries and dislocation strengthening (Hall, 1951, Gupta et al. 2016). Cu-4.5%Ti alloy possess maximum strength in samples processed by MAF for 3 cycles.
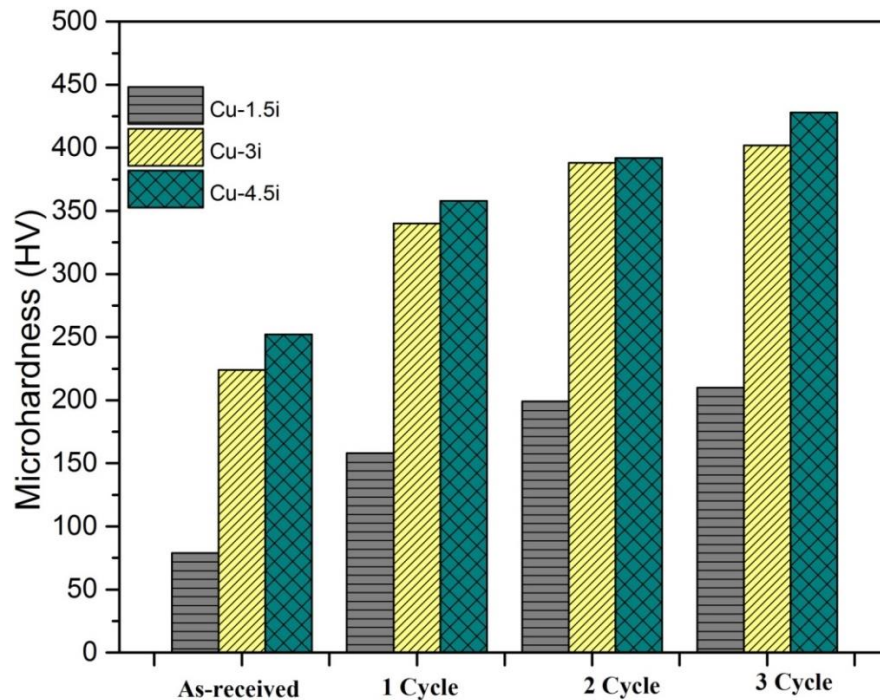
Figure 7.3 Comparision of Microhardness with number of MAF cycles for different alloys

Figure 7.3 shows the variation of Vickers Microhardness (HV) with various conditions of samples of Cu-1.5%Ti, Cu-3%Ti and Cu-4.5%Ti alloy. As Ti% increases, hardness increases for as received material (Markandeya et al.2006, Nagarjuna et al.1996, Semboshi et al.2019). In all 3 alloys, as-received sample shows minimum value of hardness. As the number of MAF cycles increases, hardness value increases, because of strain hardening effect and grain refinement. During 1st cycle, increment rate of hardness is high, because of high grain refinement rate. After 2nd and 3rd cycle of MAF, hardness increment rate reduces. Cu-4.5%Ti alloy shows highest hardness among all 3 alloys.

Figure 7.4 shows % elongation of Cu-1.5Ti, C-3%Ti and Cu-4.5%Ti alloys. As received samples shows high ductile (Nagarjuna et al.2001). After 1 cycle of MAF, ductility of the material reduces, but after 2 and 3 cycles of MAF, ductility increases slightly, due to decrease in shear band width and twin width/spacing. As received Cu-1.5%Ti has high ductility and Cu-4.5%Ti alloy had least ductility (Nagarjuna et al.1999).
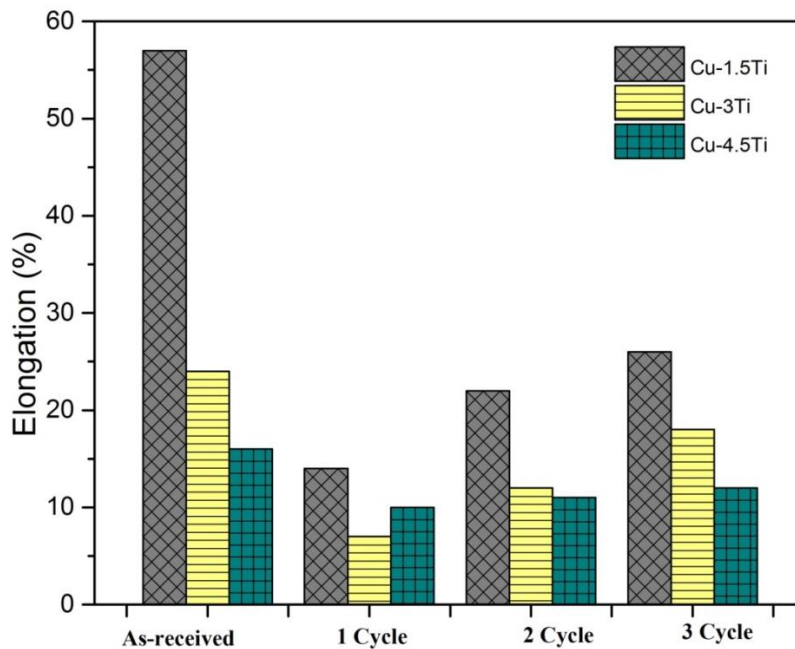
Figure 7.4 Comparision of % Elongation v/s number of MAF cyclesfor different alloys

7.2 Wear properties

Figure 7.5 shows the variation of wear rate with different conditions of samples of Cu-1.5%Ti, Cu-3%Ti and Cu-4.5%Ti alloy, with velocity of 2 m/s at a load of 20 N load. When number of MAF cycles increases (for different loading and sliding conditions) wear resistance increases, due to increased hardness. MAF processed samples show decreased wear rate. With increase in load and sliding distances, wear rate increases for all samples and is shown in figure 7.5. As MAF cycles increase, wear rate reduces, due to increases in hardness of the sample. Wear rate is related to hardness, by Archard equation. MAF process gives better microhardness properties because of grain refinement in the material, wear rate of MAF processed samples is reduced.

Cu-1.5%Ti samples have high wear rate, as compared to Cu-3%Ti and Cu-4.5%Ti, because of high ductility. Cu-4.5%Ti have higher wear resistance, due to low ductility. 3 cycle MAF processed sample has lowest wear rate as shown in figure 7.5.
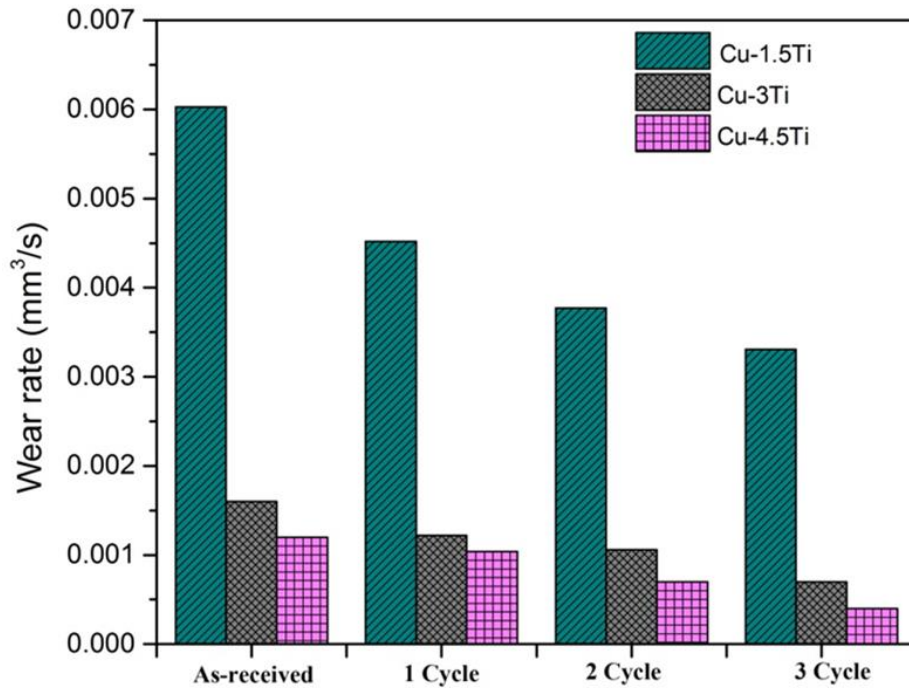
Figure 7.5 Comparision of Wear rate v/s number of MAF cycles for different alloys

7.3 Corrosion properties

Cu-1.5%Ti has higher corrosion resistance, as compared to, Cu-3%Ti and Cu-4.5%Ti alloy, as observed from figure 7.6. This clearly shows that, as %Ti increases, corrosion rate increases, thereby reducing corrosion resistance. It is also observed that corrosion rate decreases with increase in MAF cycles, thus indicating improvement in corrosion resistance and current density. Main reason for enhancement in corrosion resistance of UFG materials is attributed to improvement in passive film formation and adhesion due to increased grain boundary density. 3 cycle MAF processed sample shows highest corrosion resistive property and also Cu-1.5%Ti has lowest corrosion rate, due to less %Ti in the Cu matrix (Huan et al. 2018).
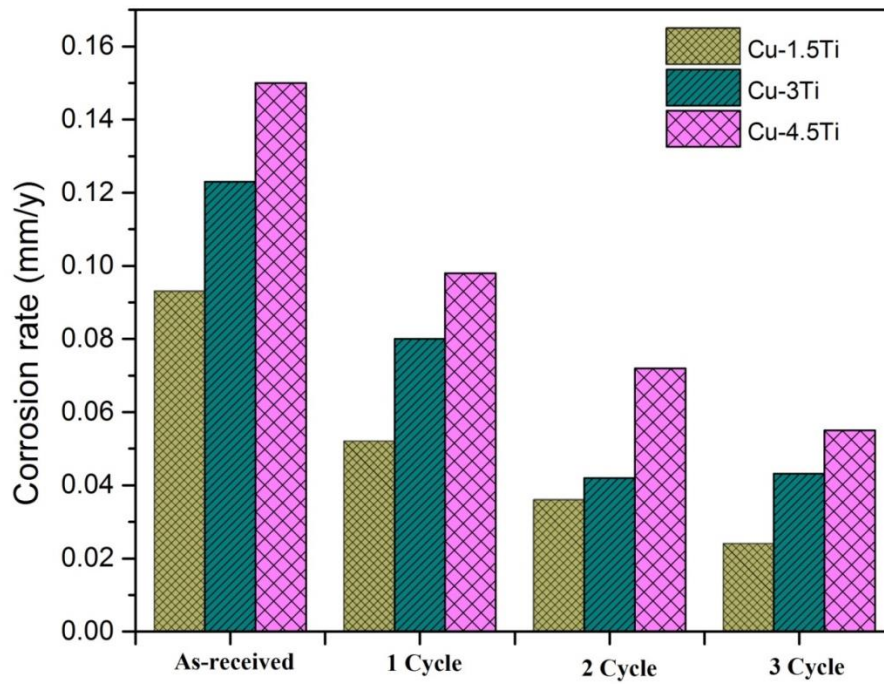
Figure 7.6 Comparision of Corosion rate v/s number of MAF cycles for different alloys

CHAPTER 8

8. CONCLUSIONS

Multi axial forging was performed on Cu-1.5%Ti, Cu-3%Ti and Cu-4.5%Ti at a cryogenic temperature. Effect of MAF process on microstructure, mechanical properties, wear and corrosion studies were investigated. Microstructural studies were conducted using OM, SEM, TEM, EBSD and XRD, to study the grain structure, grain size, grain misorientation angles and presence of intermetallic in the microstructure. Tensile and hardness tests were performed to know the strength and hardness of MAF processed samples. Wear test was carried out to know the wear characteristics of both as-received and MAF processed samples. Electrochemical measurements were conducted to measure the corrosion resistance of as-received and MAF processed samples and the conclusions are summarized up based on the achieved outcome.

Microstructural studies of as-received and MAF processed Cu-Ti alloys

- Average grain size reduced to 2 μm for Cu-1.5%Ti, 250 nm for Cu-3%Ti and 200 nm for Cu-4.5%Ti after 3 cycles of MAF.

- As the number of MAF cycle increased, density of shear bands increased and width of shear bands decreased. After 3 cycle of MAF, Grain refinement was maximum, because of formation high density shear bands.

- EBSD was carried out to know the misorientation angles of as-received and MAF processed sample. It was observed that, as strain increased during MAF process, occurrence of LAGBs increased and HAGBs were converted to LAGBs.

Mechanical properties of as-received and MAF processed Cu-Ti alloys

- Tensile strength improved with increase in MAF cycles, at cryogenic temperature. Maximum UTS (592 MPa,1126 MPa, 1284 MPa) was obtained for 3 cycle MAF processed samples in all three composition of Cu-1.5%Ti, Cu-3%Ti and Cu-4.5%Ti alloys respectively. Increase in strength is attributed to grain boundary strengthening mechanism and increase in dislocation density,

with increase in number of MAF passes. Decreasing shear band width/twin width is also the reason for improvement in strength and ductility of material.

- Hardness was observed to be maximum of 211 HV, 402 HV, 428 HV for 3 cycles MAF processed samples for Cu-1.5%Ti, Cu-3%Ti and Cu-4.5%Ti respectively. As the number of MAF cycles increases, hardness value increases, because of strain hardening, high dislocation density and also, due to formation of ultrafine grains.

- Fractured surface of MAF processed samples indicate the type of fracture behavior. During first MAF cycle, dimples are finer, because of grain refinement and strain hardening, indicating combination of brittle and ductile fracture. At higher cycles, dimple size increased, because of decrease in the shear band width and twin width and dimpled appearance indicating ductile fracture behavior, indicating ductile fracture behavior. Wear behavior of as-received and MAF processed Cu-Ti alloys.

- As-received and MAF processed samples were subjected to dry sliding wear test to estimate the COF for different loading condition. COF decreased with increase in MAF cycles, but increased, as load and sliding distance increased. Overall, COF value decreased in MAF processed samples. Higher wear resistance was observed in 3 cycles MAF processed samples, due to increase in hardness of Cu-Ti alloys as compared to as-received alloys.

- MAF processed samples showed lower wear rate as compared to as-received samples and wear resistance was increased with increase in MAF cycles due to increased hardness of samples. Wear mass loss was lower in case of MAF processed samples, when compared to that of as-received material. Wear mass loss directly depends on the hardness of the material.

- Microstructure of worn as-received and MAF processed samples shows surface plastic deformation, ploughing and scratches. These irregularities increased with increase in load and decreased, with increase in number of MAF passes. EDS analysis showed presence of oxygen peaks along with copper peak on the wear surface, indicating abrasion and oxidation wear mechanisms.

Corrosion behavior of as-received and MAF processed Cu-Ti alloys

- Potentiodynamic polarization test showed reduced corrosion current density (I_{corr}) which indicates higher corrosion resistance for the MAF processed samples, due to the presence of equiaxed fine grained microstructure and homogeneously distributed secondary particles.

- Electrochemical impedance spectroscopy results indicate an increase in charge-transfer resistance (R_t) values for MAF processed samples compared to as-received condition. Increase in Rt values represents increased corrosion resistance of the sample.

SCOPE OF FUTURE WORK

- The present research work can further be extended to study the microstructural stability of the developed UFG Copper alloy by performing heat treatment at different elevated temparatures.

- To study the thermal behaviour of both as-received and MAF processed samples.

- Study the Electrical conductivity test for both as-received and MAF processed samples.

- To study the Fatiuge behaviour of both as-received and MAF processed samples.

- Study the MAF process at different strain rate conditions and study the microstructural and strength variations.

REFERENCES

Akbaripanah, F., Salavati, M., and Mahmudi, R. (2017). "The influences of extrusion and Multi-Directional Forging (MDF) Processes on microstructure, shear strength and microhardness of AM60 Magnesium Alloy." *M. Mech. Eng.*, *16*(11), 409-416.

Anne, G., Ramesh, M. R., Nayaka, H. S., Arya, S. B. and Sahu, S. (2017). "Development and characteristics of accumulative roll bonded Mg-Zn/Ce/Al hybrid composite." J. Alloys Compd., 724, 146-154.

Anne, G., Ramesh, M. R., Nayaka, H. S., Arya, S. B. and Sahu, S. (2017). Development and properties evaluation of Mg–6% Zn/Al multilayered composites processed by accumulative roll bonding." *J. Mater. Res.,* 32(12), 2249-2257.

Anne, G., Ramesh, M. R., Nayaka, H. S., Arya, S. B. and Sahu, S. (2017). "Microstructure evolution and mechanical and corrosion behavior of accumulative roll bonded Mg-2% Zn/Al-7075 multilayered composite." *J. Mater. Eng. Perform.*, *26*(4), 1726-1734.

Archard, J. (1953). "Contact and rubbing of flat surfaces". *J. Appl. Phys.,* 24(8), 981-988.

Armstrong, P. E., Hockett, J. E. and Sherby, O. D. (1982). "Large Multidirectional Compression Strain of 1100 Al [J]". *J Mech Phys Solids.*, *30*, 37.

Bay, B., Hansen, N., Hughes, D. A and Kuhlmann-Wilsdor, D., (1992). "Evolution of FCC de-formation structures in polyslip." *Acta Metall. Mater.*, 40, 205-219.

Belyakov, H., Miura, H and Sakai,T. (2000). "Fine-grained structure formation in austenitic stainless steel under multiple deformations at 0.5T m." *Mater.Trans.JIM4.,* 476-484.

Belyakov, A., Sakai, T., Miura, H., and Tsuzaki, K. (2001). "Grain refinement in copper under large strain deformation." *Philos. Mag. A.*, 81(11), 2629-2643.

Cao, C. (1990). "On the impedance plane displays for irreversible electrode reactions based on the stability conditions of the steady-state-I. One state variable besides electrode potential." *Electrochem. Acta.*, 35, 831-836.

Chen, Q., Shu, D., Hu, C., Zhao, Z and Yuan, B. (2012). "Grain refinement in an as-cast AZ61 magnesium alloy processed by multi-axial forging under the multitemperature processing procedure." *Mater. Sci. Eng. A, 541*, 98-104.

Chegini, M., Fallahi, A and Shaeri, M. H. (2015). "Effect of equal channel angular pressing (ECAP) on wear behavior of Al-7075 alloy. *Proc. Mater. Sci.*, *11*, 95-100.

Cheng, S., Zhao, Y. H., Zhu, Y. T and Ma, E. (2007). "Optimizing the strength and ductility of fine structured 2024 Al alloy by nano-precipitation." *Acta Mater.*, 55(17), 5822-5832.

Dasharath, S. M and Mula, S. (2016). "Mechanical properties and fracture mechanisms of ultrafine grained Cu-9.6% Zn alloy processed by multiaxial cryoforging." *Mater. Sci. Eng. A., 675*, 403-414.

Dasharath, S. M and Mula, S. (2017). "Improvement of mechanical properties and fracture toughness of low SFE Cu-Al alloy through microstructural modification by multiaxial cryoforging." *Mater. Sci. Eng. A.,* 690, 393-404.

Dao, M., Lu, L., Shen, Y. F and Suresh, S. (2006). "Strength, strain-rate sensitivity and ductility of copper with nanoscale twins." *Acta Mater.*, 54(20), 5421-5432.

Dehghan, Nayeri F., Esfandyarpour, B., Ashkan Behnam, Soleymani E. Asl, Zadeh Sh Mohajer, and Mohammad Hadi Maleki (2007). "Ohmic contact of Cu/Mo and Cu/Ti thin layers on multi-crystalline silicon substrates." *Iran. J. Chem. Chem. Eng.*, 55-59.

Dieter G E, Mechanical Metallurgy, 3rd edition., Mc Graw-Hill Book Co., New York, 1988

Flausino, P. C. A., Nassif, M. E. L., de Castro Bubani, F., Pereira, P. H. R., Aguilar, M. T. P and Cetlin, P. R. (2019). "Microstructural evolution and mechanical behavior of copper processed by low strain amplitude multi-directional forging." *Mater. Sci. Eng. A*, 756, 474-483.

Gao, L. L and Cheng, X. H. (2008). "Microstructure and dry sliding wear behavior of Cu–10% Al–4% Fe alloy produced by equal channel angular extrusion." *Wear.*, 265(7-8), 986-991.

Gopi, K. R., Nayaka, H. S and Sahu, S. (2016). "Investigation of microstructure and mechanical properties of ECAP-processed AM series magnesium alloy." *J. Mater. Eng. Perform.*, 25(9), 3737-3745.

Gopi, K. R., Nayaka, H. S and Sahu, S. (2017). "Microstructural Evolution and Strengthening of AM90 Magnesium Alloy Processed by ECAP." *Arb. J. Sci. Eng.*, 42(11), 4635-4647.

Gupta, R., Srivastava, S., Kumar, N. K and Panthi, S. K. (2016). "High leaded tin bronze processing during multi-directional forging: Effect on microstructure and mechanical properties." *Mater. Sci. Eng. A*, 654, 282-291.

Hall, E O., (1951), " The deformation and ageing of mild steel." *Proc. Phy. Scoc.,* (London), Vol. 64 B, pp. 747-753.

Horita, Z and Langdon, T. G. (2005). "Microstructures and microhardness of an aluminum alloy and pure copper after processing by high-pressure torsion." *Mater. Sci. Eng. A.*, *410*, 422-425.

Hu, H. J., Fan, J. Z., Wang, H., Zhai, Z. Y., Li, Y. Y and Ou, Z. (2015). Dry sliding wear behavior of ES-processed AZ31B magnesium alloy." *Russ. J. Non- Ferrous Mater*, *56*(4), 392-398.

Huang, J. Y., Zhu, Y. T., Jiang, H and Lowe, T. C. (2001). "Microstructures and dislocation configurations in nanostructured Cu processed by repetitive corrugation and straightening." *Acta Mater.*, *49*(9), 1497-1505.

Huang, J., Zhu, Y. T., Alexander, D. J., Liao, X., Lowe, T. C and Asaro, R. J. (2004). "Development of repetitive corrugation and straightening." *Mater Sci Eng. A*, *371*(1-2), 35-39

Huan, W. E. I., Hou, L. F., Cui, Y. C and Wei, Y. H. (2018). "Effect of Ti content on corrosion behavior of Cu-Ti alloys in 3.5% NaCl solution." *Trans. Non-Ferrous Mater. Soc. China.*, 28(4), 669-675.

Ivanisenko, Y., Kulagin, R., Fedorov, V., Mazilkin, A., Scherer, T., Baretzky, B and Hahn, H. (2016). "High pressure torsion extrusion as a new severe plastic deformation process." *Mater. Sci. Eng. A.*, *664*, 247-256.

Jamali, A and Mahmudi, R. (2019). "Evolution of microstructure, texture, and mechanical properties in a multi-directionally forged ZK60 Mg alloy." *Mater. Sci. Eng. A., 752*, 55-62.

Jia, D., Wang, Y. M., Ramesh, K. T., Ma, E., Zhu, Y. T and Valiev, R. Z. (2001). "Deformation behavior and plastic instabilities of ultrafine-grained titanium." *Appl. Phys. Lett., 79*(5), 611-613.

Joshi, A., Kumar, N., Yogesha, K. K., Jayaganthan, R and Nath, S. K. (2016). "Mechanical properties and microstructural evolution in Al 2014 alloy processed through multidirectional cryoforging." *J. Mater. Eng. Perform.*, 25(7), 3031-3045.

Kikuchi, M., Takada, Y., Kiyosue, S., Yoda, M., Woldu, M., Cai, Z and Okabe, T. (2003). Mechanical properties and microstructures of cast Ti–Cu alloys." *Dental. Mater*, *19*(3), 174-181.

Kim, J. K., Kim, H K., Park, J. W., and Kim, W. J. (2005) "Micro-extrusion of ECAP processed magnesium alloy for production of high strength magnesium micro-gears." *Scr. Mater*., 53, 1207–1211.

Kim, J. K., Jeong, H. G., Hong, S. I., Kim, Y. S and Kim, W. J. (2001). "Effect of aging treatment on heavily deformed microstructure of a 6061 aluminum alloy after equal channel angular pressing." *Scr.Mater.*, 45(8), 901-907.

Kim, W. J., Chung, C. S., Ma, D. S., Hong, S. I and Kim, H. K. (2003). "Optimization of strength and ductility of 2024 Al by equal channel angular pressing (ECAP) and post-ECAP aging." *Scr Mater.*, 49(4), 333-338.

Kobayashi, C., Sakai, T., Belyakov, A and Miura, H. (2007). Ultrafine grain development in copper during multidirectional forging at 195 K." *Philos. Mag. Lett*., 87(10), 751-766

Kral, R., Minarik, P., Lesna, I. K., Skublova, L., Harcuba, P., Hadzima, B and Janecek, M. (2011). "Effect of Grain Refinement on Electrochemical Characteristics in AE42 Magnesium Alloy." WDS'11 *Proceedings of Contributed Papers, Part III,* 136-140.

Krishna, K. S. V. B. R., Ashfaq, M., Varun, V., Sivaprasad, K., Venkateswarlu, K and

Akella, S. S. (2017). "On Plastic Deformation Behavior of Cryorolled AA8090 Alloy." *Trans. Indian Inst. Met.*, 70(6), 1463-1475.

Kumar, N., Owolabi, G. M and Jayaganthan, R. (2019). "Al 6082 alloy strengthening through low strain multi-axial forging." *Mater. Charact*., *155*, 109761.

Kumar, S. S and Raghu, T. (2015). "Bulk processing of fine grained OFHC copper by cyclic channel die compression." *Int. J. Mater. Res.,* 106, 1230-1239.

Lee, C. S., Kim, M. G., Kim, G. H., Kim, K. T., Hwang, D and Kim, H. S. (2019). "Corrosion Properties of Ultra-Fine-Grained Cu-3 wt% Ti Alloy Fabricated by Combination of Hot Rolling and Aging Treatment." *J. Nanosci. Nanotechnol.*, *19*(10), 6487-6492.

Luo, P., Hu, Q and Wu, X. (2016). "Quantitatively analyzing strength contribution vs grain boundary scale relation in pure titanium subjected to severe plastic deformation." *Metall. Mater. Trans. A.,* 47(5), 1922-1928.

Luo, P. (2018). "Analysis of Microstructure and Its Effect on Yield Strength of Pure Alpha-Titanium Consolidated by Equal Channel Angular Pressing." *Mater. Trans*. 59(7), 1161-1165.

Luo, P. E. N. G., McDonald, D. T., Xu, W., Palanisamy, S., Dargusch, M. S and Xia, K. E. N. O. N. G. (2012). "A modified Hall–Petch relationship in ultrafine-grained titanium recycled from chips by equal channel angular pressing." *Scr Mater.,* 66(10), 785-788.

Manjunath, G. K., Bhat, K. U., Kumar, G. P and Ramesh, M. R. (2018). "Microstructure and Wear Performance of ECAP Processed Cast Al–Zn–Mg Alloys". *Trans. Ind. Inst. Metals,* 71(8), 1919-1931.

Mao, J., Kang, S. B and Park, J. O. (2005). "Grain refinement, thermal stability and tensile properties of 2024 aluminum alloy after equal-channel angular pressing." *J. Mater. Process. Technol*., 159(3), 314-320.

Markandeya, R., Nagarjuna, S., Satyanarayana, D. V. V and Sarma, D. S. (2006). "Correlation of structure and flow behaviour of Cu–Ti–Cd alloys." *Mater. Sci. Eng. A.*, 428(1-2), 233-243.

Nagarjuna, S., Srinivas, M., Balasubramanian, K and Sarmat, D. S. (1997). "Effect of alloying content on high cycle fatigue behaviour of Cu-Ti alloys." *Int. J. Fatigue*, *19*(1), 51-57.

Nagarjuna, S., Srinivas, M., Balasubramanian, K and Sarma, D. S. (1999). "On the variation of mechanical properties with solute content in Cu–Ti alloys." *Mater. Sci. Eng. A.*,*259*(1), 34-42.

Nagarjuna, S. (2004). "Thermal conductivity of Cu-4.5 Ti alloy." *Bull. Mater. Sci.*, *27*(1), 69-71.

Nagarjuna, S., Srinivas, M., Balasubramanian, K and Sarma, D. S. (1996). "The alloy content and grain size dependence of flow stress in Cu-Ti alloys." *Acta Mater,. 44*(6), 2285-2293.

Nagarjuna, S., Srinivas, M., Balasubramanian, K and Sarma, D. S. (1994). "Influence of polycrystalline grain size on yield and flow stress in Cu-1.5 wt% Ti alloy." *Scr. Metall. Mater.*, *30*(12), 1593-1597.

Nagarjuna, S., Sharma, K. K., Sudhakar, I and Sarma, D. S. (2001). "Age hardening studies in a Cu–4.5 Ti–0.5 Co alloy." *Mater. Sci. Eng. A.*, 313(1-2), 251-260.

Nieh, T. G and Wadsworth, J. (1991). "Hall-Petch relation in nanocrystalline solids." *Scr. Metall. Mater.*, 25(4), 955-958.

Ning, J. L and Wang, D. (2012). "Concurrent high strength and high ductility in isotropic bulk Cu–Al alloy with three-dimensional nano-twinned structure." *J. Alloys Compd.*, *514*, 214-219.

Orlov, D., Ralston, K. D., Birbilis, N and Estrin, Y. (2011). "Enhanced corrosion resistance of Mg alloy ZK60 after processing by integrated extrusion and equal channel angular pressing." *Acta Mater.,* 59(15), 6176-6186.

Padap, A. K., Chaudhari, G. P., Nath, S. K and Pancholi, V. (2009). "Ultrafine-grained steel fabricated using warm multiaxial forging: Microstructure and mechanical properties." *Mater. Sci. Eng. A.*, *527*(1-2), 110-117.

Pardo, A., Merino, M.C., Coy, A.E., Viejo, F., Arrabal, R and Feliu Jr., S. (2008).

"Influence of microstructure and composition on the corrosion behaviour of Mg/Al alloys in chloride media." *Electrochem. Acta*, 53, 7890-7902.

Petch, N J., (1953), " The clevage strength of polycrystals", *J. Iron Steel Inst.*, Vol. 174, pp. 25.

Purcek, G., Yanar, H., Saray, O., Karaman, I and Maier, H. J. (2014). "Effect of precipitation on mechanical and wear properties of ultrafine-grained Cu–Cr–Zr alloy." *Wear*, *311*(1-2), 149-158.

Raab, G. J., Valiev, R. Z., Lowe, T. C and Zhu, Y. T. (2004). "Continuous processing of ultrafine grained Al by ECAP–Conform." *Mater. Sci. Eng. A.*, *382*(1-2), 30-34.

Ralston, K. D and Birbilis, N. (2010). "Effect of grain size on corrosion: a review." *Corrosion.*, 66(7), 075005-075005

Rao, P. N., Singh, D and Jayaganthan, R. (2014). "Mechanical properties and microstructural evolution of Al 6061 alloy processed by multidirectional forging at liquid nitrogen temperature." *Mater. Des.*, 56, 97-104.

Richert, M., Stüwe, H. P., Richert, J., Pippan, R and Motz, C. (2001). "Characteristic features of microstructure of ALMg5 deformed to large plastic strains." *Mater. Sci. Eng. A,* 301(2), 237-243.

Sahu, S., Yadav, P. C and Shekhar, S. (2018). "Use of hot rolling for generating low deviation twins and a disconnected random boundary network in inconel 600 alloy." *Metall. Mater. Trans. A*, 49(2), 628-643.

Sarma, V. S., Sivaprasad, K., Sturm, D and Heilmaier, M. (2008). "Microstructure and mechanical properties of ultra fine grained Cu–Zn and Cu–Al alloys produced by cryorolling and annealing." *Mater. Sci. Eng. A.*, *489*(1-2), 253-258.

Semboshi, S and Takasugi, T. (2013). "Fabrication of high-strength and high-conductivity Cu–Ti alloy wire by aging in a hydrogen atmosphere." *J. Alloys Compd.*, *580*, S397-S400.

Semboshi, S., Hinamoto, E and Iwase, A. (2014). "Age-hardening behavior of a single-

crystal Cu–ti alloy." *Mater. Lett.*, *131*, 90-93.

Semboshi, S., Kaneno, Y., Takasugi, T., Han, S. Z and Masahashi, N. (2019). "Effect of Composition on the Strength and Electrical Conductivity of Cu-Ti Binary Alloy Wires Fabricated by Aging and Intense Drawing." *Metall. Mater. Trans. A.*, 50(3), 1389-1396.

Shin, D. H., Park, J. J., Kim, Y. S and Park, K. T. (2002). "Constrained groove pressing and its application to grain refinement of aluminum." *Mater. Sci. Eng. A., 328*(1-2), 98-103

Sobhani, M., Arabi, H., Mirhabibi, A and Brydson, R. M. D. (2013). "Microstructural evolution of copper–titanium alloy during in-situ formation of TiB2 particles." *Trans. Non-ferrous. Met. Soc. China*, 23(10), 2994-3001.

Song, D., Ma, A., Jiang, J., Lin, P., Yang, D and Fan, J. (2010). "Corrosion behavior of equal-channel-angular-pressed pure magnesium in NaCl aqueous solution." *Corros. Sci.*, 52(2), 481-490

Song, D., Ma, A. B., Jiang, J. H., Lin, P. H., Yang, D. H and Fan, J. F. (2011). "Corrosion behaviour of bulk ultra-fine grained AZ91D magnesium alloy fabricated by equal- channel angular pressing." *Corros. Sci.*, 53(1), 362-373.

Stolyarov, V. V., Zhu, Y. T., Alexandrov, I. V., Lowe, T. C and Valiev, R. Z. (2001). "Influence of ECAP routes on the microstructure and properties of pure Ti." *Mater. Sci. Eng. A.*, *299*(1-2), 59-67.

Sunil, B. R. (2015). "Repetitive corrugation and straightening of sheet metals." *Mater. Manuf. Processes*, *30*(10), 1262-1271.

Swaminathan, S., Shankar, M. R., Rao, B. C., Compton, W. D., Chandrasekar, S., King, A. H and Trumble, K. P. (2007). "Severe plastic deformation (SPD) and nanostructured materials by machining." *J. Mater. Sci. 42*(5), 1529-1541

Szkliniarz, A., Blacha, L., Szkliniarz, W and Łabaj, J. (2014). "Characteristics of Plasticity of Hot Deformed Cu-Ti Alloys." *Arch. Metall. Mater.*, *59*(4), 1307-1312.

Toroghinejad, M. R., Jamaati, R., Nooryan, A and Edris, H. (2014). "Hybrid composites produced by anodizing and accumulative roll bonding (ARB)

processes". *Ceramics International*, *40*(7), 10027-10035.

Tsuji, N., Saito, Y., Utsunomiya, H and Tanigawa, S. (1999). "Ultra-fine grained bulk steel produced by accumulative roll-bonding (ARB) process". *Acta mater*. 40(7), 795-800.

Valiev, R. (2004). "Nanostructuring of metals by severe plastic deformation for advanced properties." *Nat. Mater.,3*(8), 511.

Valiev, R. Z., Estrin, Y., Horita, Z., Langdon, T. G., Zechetbauer, M. J and Zhu, Y. T. (2006). "Producing bulk ultrafine-grained materials by severe plastic deformation."*JOM*, *58*(4), 33-39.

Valiev, R. Z., Islamgaliev, R. K and Alexandrov, I. V. (2000). "Bulk nanostructured materials from severe plastic deformation." *Prog. Mater. Science*, *45*(2), 103-189.

Valiev, R. Z., Korznikov, A. V and Mulyukov, R. R. (1993). "Structure and properties of ultrafine-grained materials produced by severe plastic deformation." *Mater. Sci. Eng. A*, *168*(2), 141-148.

Wang, Chuan Ting, Nong Gao, Mark G. Gee, Robert JK Wood, and Terence G. Langdon. "Effect of grain size on the micro-tribological behavior of pure titanium processed by high-pressure torsion." *Wear* 280 (2012): 28-35.

Wang, C. T., Gao, N., Wood, R. J and Langdon, T. G. (2011). "Wear behavior of an aluminum alloy processed by equal-channel angular pressing." *J. Mater. Sci., 46*(1), 123-130

Xia, X., Chen, Q., Zhao, Z., Ma, M., Li, X and Zhang, K. (2015). "Microstructure, texture and mechanical properties of coarse-grained Mg–Gd–Y–Nd–Zr alloy processed by multidirectional forging." *J. Alloys Compd*, *623*, 62-68

Xu, J., Wang, X., Zhu, X., Shirooyeh, M., Wongsa-Ngam, J., Shan, D., Guo, B and Langdon, T. G. (2013). "Dry sliding wear of an AZ31 magnesium alloy processed by equal-channel angular pressing." *J. Mater. Sci*., 48(11), 4117-4127.

Yadav, P. C., Sinhal, A., Sahu, S., Roy, A and Shekhar, S. (2016). "Microstructural inhomogeneity in constrained groove pressed Cu-Zn alloy sheet." *J. Mater. Eng Perfor.*, *25*(7), 2604-2614.

Yadav, P. C., Sahu, S., Subramaniam, A and Shekhar, S. (2018). "Effect of heat-treatment on microstructural evolution and mechanical behaviour of severely deformed Inconel 718." *Mater. Sci. Eng. A*., *715*, 295-306.

Zhao, Y. H., Bingert, J. F., Liao, X. Z., Cui, B. Z., Han, K., Sergueeva, A. V. and Zhu, Y. T. (2006). "Simultaneously increasing the ductility and strength of ultra-fine-grained pure copper." *Adv. Mater.*, *18*(22), 2949-2953

Zhilyaev, A. P., Lee, S., Nurislamova, G. V., Valiev, R. Z and Langdon, T. G. (2001). "Microhardness and microstructural evolution in pure nickel during high-pressure torsion." *Scr. Mater.*, *44*(12), 2753-2758.

Zhilyaev, A. P and Langdon, T. G. (2008). "Using high-pressure torsion for metal processing: Fundamentals and applications." *Prog. Mater. Sci.*, *53*(6), 893-979.

Zhu, Y. T and Lowe, T. C. (2000). "Observations and issues on mechanisms of grain refinement during ECAP process." *Mater. Sci. Eng. A*, *291*(1-2), 46-53.

Zhu, Y. T and Liao, X. (2004). "Nanostructured metals: retaining ductility." *Nat. Mater., 3*(6), 351.

LIST OF PUBLICATIONS AND CONFERENCE

Sl. No.	Title of the Paper	Authors (In the same order as in the paper, underline the Research Scholar's name)	Name of the Journal / Conference / Symposium, Vol., No., Pages	Month & Year of Publication	Category *
1	Investigation of Microstructure and Mechanical Properties of Cu-3%Ti Alloy processed by Multiaxial Cryo-forging"	**Ramesh S**, H. Shivananda Nayaka, Gopi K. R.,Sandeep Sahu, Udaya Bhat K	Journal of Materials Research , volume 33, issue 22, pages 3700-3710	2018	1
2	Influence of Multiaxial cryoforging on mechanical and microstructural properties of Cu-Ti Alloy	**Ramesh S.,** H. Shivananda Nayaka, Gopi K. R.,Sandeep Sahu.	Material Research Express, volume 2, issue 2, pages, 026556	2019	1
3	Influence o Multiaxial Cryoforging on Microstructure, Mechanical and Corrosion Properties of Copper-Titanium Alloy	**Ramesh S**.H. Shivananda Nayaka, Sandeep Sahu, Gopi K. R, Shivaram M J, Shashibushan Arya	Journal of Materials Engineering and Performance, 28(12), 7629-7641.	2019	1
4	Effect of combined multiaxial forging and rolling process on microstructure, mechanical properties and corrosion behavior of a Cu-Ti alloys	**Ramesh S**, Gajanan Anne H Shivananda Nayaka Sandeep Sahu Shashibhushan Arya	Material Research Express, volume 6, issue 5, pages, 056559	2019	1
5	Investigation of Tribological and Corrosion Behavior of Cu-Ti Alloy Processed by Multiaxial Cryoforging	**Ramesh S,** H. Shivananda Nayaka	Journal of Materials Engineering and Performance	2020	1
6	Influence of Multiaxial cryoforging on wear properties of Copper-Titanium alloy	**Ramesh S**, H. Shivananda Nayaka,	Material Science Forum (Vol. 969, pp. 392-397)	2019	1

*Category:

7	Effect of Multi axail cryo-forging on wear resistance of Copper-Titanium alloys	**Ramesh S**, H. Shivananda Nayaka,	Journal of Wear and Friction	Under Review	1
8	Influence of Multi Axial Forging (MAF) on Microstructure and Mechanical Properties of Cu-Ti Alloy	**Ramesh S**, H. Shivananda Nayaka, Gopi K. R.,	Materials Today: Proceedings, 5(11), 25534-25540.	2018	2
9	Mechanical properties and Microstructure studies of Cu-Ti alloy Processed by Multi Directional Cryo-Forging"	**Ramesh S**, H. Shivananda Nayaka,	NMD-ATM 2017, BITS Pilani, Goa, Nov-2017	Nov 2017	4
10	Influence of Multiaxial cryoforging on wear properties of Copper-Titanium alloy	**Ramesh S**, H. Shivananda Nayaka,	IES-2019 Kumamoto university, Japan	March, 2019	3
11	Wear and Corrosion properties of Cu-3%Ti alloy processed by multi axil cryoforging	Ramesh S, H. Shivananda Nayaka,	NMD ATM-2019, Trivendrum	Nov 2019	4

1: Journal paper, full paper reviewed.

2: Journal paper, Abstract reviews.S

3: Conference/Symposium paper, full paper reviewed.

4: Conference/Symposium paper, abstract reviewed.

5: others (including papers in Workshops, NITK Research Bulletins, Short notes etc.)

Ramesh S   **Dr. H Shivananda Nayaka**

Research Scholar   Research Guide

Name & Signature, with Date   Name & Signature, with Date

BIO-DATA

Name : Ramesh S

Father's Name : Sampath T

Date of Birth : 10-02-1990

Nationality : Indian

Marital Status : Single

Address:

Permanent Address   **Present Address**

Permanent Address	Present Address
Ramesh S S/o Sampath T. Agradahalli camp, Agaradahalli post, Bhadravathi , Shivamogga, Karnataka	Department of Mechanical Engineering National Institute of Technology Karnataka Surathkal-575025, Srinivasanagar, Dhakshina Kannada (Dist), Karnataka,

Mobile Number : +91-9742103996

E-mail id. : ramaghalli@gmail.com

Educational Qualification:

Qualification	College/school	University/Board	Year of Passing	Performance
Ph.D. in Mechanical Engineering	National Institute of Technology Karnataka	National Institute of Technology Karnataka	2020	8.64 (CGPA)
M. Tech in Machine Design	Adichunchanagiri Institute of Technology	Visvesvaraya Technological University (VTU)	2014	79 % (FCD)
B. E in Mechanical Engineering	Jawaharlal Nehru National college of Engineering	Visvesvaraya Technological University (VTU)	2011	69 % (FC)

Research Publications:

Number of papers published in International Journals	Number of papers published in International Conference/Symposium
10	5

Work Experience:

Name of the Organization	Duration	Position
BIT Mangalore	2014-2016	Assistant Professor

I declare that above information is true and correct to best of my knowledge.

(Ramesh S)